Cosmological angular correlations with γ-ray data

Università degli Studi di Torino

Scuola di Dottorato

Tesi di Dottorato di Ricerca in Scienza ed Alta Tecnologia

Indirizzo di Fisica ed Astrofisica

University of Chinese Academy of Sciences

Institute of High Energy Physics

Particle Physics and Nuclear Physics

Author: Xiu-hui Tan

Supervisors: Prof. Regis Marco
Prof. Fornengo Nicolao
Prof. Bi Xiao-jun

I would like to dedicate this thesis to my whole family, my husband, mother, father and brother, who have always believed in and supported me wholeheartedly; to my teachers and supervisors, who have led me into this splendid and marvelous physical field; and to my closed friends, who have spent joyous and wonderful time with me in youth.

Acknowledgements

The whole story began in September of 2017, when I first arrived in Turin, Italy. That was also my first time to go abroad, facing with a completely unfamiliar city and different culture, life was a little difficult and challenging for me surely. Fortunately, the people I met and acquainted with within Turin gradually made me feel at home. I am still a beginner to Italian, however, whenever I am back to Turin from another place, I can always feel the geniality and relaxation that the city brings to me.

First of all, I would like to make my greatest thanks to my thesis supervisors Marco Regis and Nicolao Fornengo for their huge help on countless problems that I could not solve only by myself during the calculation, derivation, and examination. Marco Regis is one of the most patient and kindest people I have ever seen and leads me to the right road finally with his hints and enlightenment. He is the second nominal supervisor of mine but actually is the first hand to instruct me. His profound comprehension of the theory, rigorousness to the scientific researches, and enthusiasm for the truth have benefited me a lot. Moreover, he also gives me large assistance for the life in Turin. At the same time, I give my sincere gratitude to my supervisor professor Nicolao Fornengo, who is knowledgeable, venerable, sagacious, and

affable, for all of the guidance and encouragement to me. Not only they inspired me directly but also offered me many extra opportunities to study in other ways. The international meetings, interesting colloquiums, and valuable summer schools were wonderful experiences for me and I have learned so many things and gotten acquainted with many peers.

Furthermore, great thanks to all of the professors, colleagues and friends in UniTO, they are including Stefano Camera, Paolo Gambino, Marco Taoso, Alessandro Cuoco, Manuel Colavincenzo, Simone Ammazzalorso, Kansitatinos Tanidis, Chiara Signorile, Michael Korsmeier, Valentina Cesare, Andrea Simonelli, Riccardo Conti, Silvia Manconi, Giovanni Pelliccioli, Riccardo Finotello, Francesco Galvagno, Elena Pinetti, Mario Motta, Gunnar Riemenschneider, …… Without your assistance, I can not achieve these easily. Although there is not enough sunshine in the underground office, their amicable and wise hearts shine like gold. I will always remember the joyful and beautiful time of the travels and parties with them, even the peaceful and ordinary daily life in the office.

Moreover, I want to thank the China Scholarship Council, professor Junqing Xia and Xiao-jun Bi for providing me such a wonderful opportunity to study in Turin. The process of signing the agreement between the University of Turin and the University of Chinese Academic of Sciences was complex, I can not manage to do those without the help from them. I appreciate the valuable comments and guidance from professor Enzo Branchini and professor David Parkinson, which are really helpful and meaningful to me.

Last but not the least, I am immensely grateful to my family, my mother, father, and brother. In particular, the unforgettable significance of Turin to me is not only I spend my Ph.D. life there, but also, that is the place where I met my husband, Yu-dong Wang.

I would search for the marvelous and mysterious truth continuously with the best people I have met, for the rest of my life.

Abstract

Over the past decades, an overwhelming amount of accurate scientific observational data, brought by ground-based detectors and space telescopes, have enhanced the possibilities to deepen our understanding about the process of formation of large-scale structures (LSS) in the Universe, and have given the opportunity to search for potential signals of dark matter particles.

Dark matter is one of the principal components of the Universe, but it is still in a bewildering condition for us. On top of the gravitational attraction, the dark matter can be subject to other (more intense) interactions, in particular, if it is in the form of a new particle beyond the standard model. Looking for signals of such interactions might bring the final proof about the dark matter existence. It is generally believed that the dark matter in halos can decay or annihilate, injecting a number of particles that can in turn induce γ-ray emissions. Fortunately, in the recent years, the γ-ray sky has been scanned in great details by the *Fermi*-LAT telescope, and the study of the unresolved γ-ray background (UGRB) (i.e., the residual emission after subtracting the galactic plane and resolved sources) has allowed us to put strong constraints on particle dark matter.

In this thesis, We measured the angular cross-correlation between the UGRB from *Fermi*-LAT data and four galaxy clusters catalogs, finding a positive signal. On one hand, we discussed this measurement in terms of compact γ-ray emission from active galactic nuclei and diffuse emission from the intra-cluster medium. On the other hand, we used it to put relevant bounds on weakly interacting massive particles (WIMP), which are one of the most competitive candidates for dark matter. The analyses were performed with a detailed estimation of the covariance matrix, which is built with mock realizations of maps of γ-rays and galaxy clusters.

Furthermore, we also calculated the cross-correlation power spectrum between the UGRB maps and the cosmic microwave background (CMB) temperature anisotropy distribution from the Planck satellite, to study the correlation with the integrated Sachs-Wolfe (ISW) effect. The ISW effect can theoretically feedback the consequence from the expansion of the Universe driven by dark energy, and it is expected to correlate with tracers of the LSS in the Universe, as, in this case, the sources of the UGRB. The signal we found, after a variety of robustness and null hypothesis tests, can be considered as an independent test of the ΛCDM model.

Contents

List of Figures

CHAPTER 1

Preface

The establishment of modern cosmology is usually considered to start with the foundation of the theory of gravitation in the form of *General Relativity* [1], which was discovered by Albert Einstein in the early 20th century. At that time, physicists were also deepening their understanding of the micro world, with several fundamental theories and mathematical models being proposed. After more than a century, we are now dealing with two theories which describe in an astonishingly good way (despite a few big open problems) the Universe and the microscopic world: the so-called *standard model of cosmology* and *standard model of particle physics*. However, the judgment of a theory can only come through observational data.

From the very beginning, people observed the starry sky and physical phenomena around them directly with naked eyes. During the last centuries, the continuous progress of science and rapid development of technology allowed us to start to explore the Universe with the help of various tools, and telescopes and detectors have become the more preeminent eyes to assist human beings. Astronomical observations extend now from the visible band down to the infrared and radio bands and up to the X and γ-ray bands, which are invisible to the naked eye. Furthermore, cosmic messengers other than photons, such as neutrinos and highly energetic cosmic-rays, have been detected and investigated. Nowadays astronomers commonly use large survey telescopes on the ground, underground and underwater detectors with capability of shielding the background noise, satellites orbiting the Earth and in the outer space, and even spacecrafts sailing outside the solar system. Detection methods of grand scales and breadths have offered an increasing large number of scientific data.

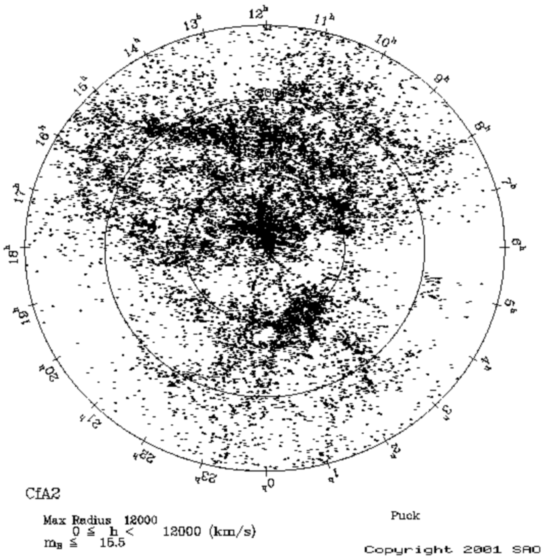

Figure 1.1: The figure shows the redshift distribution of all galaxies under the polar projection scanned by the CfA redshift survey at $12,000\,\mathrm{km\,s^{-1}}$ (the relationship between the cosmic distance and this velocity is abbreviated as $D_H = v/H_0$). The figure is taken from Ref. [2].

In the decades after the discovery of general relativity, physicists gradually accumulated observational evidences and experimental data through different kinds of telescopes and detectors, establishing the thermal *Big Bang Theory* (BBT) as the standard model for the evolution of the Universe [3].

The BBT model is now widely accepted and accurately supported by several cosmological observations. The key concept of this theory is that our Universe evolves from a primordial plasma with extremely high density and temperature. As the Universe cools down and expands, perturbations in the matter component grow, leading to the cosmological LSS visible to us today.

Back to 1920s, the American astronomer *Edwin Hubble* discovered that the receding speed of galaxies in the Universe was proportional to their distance from us, which became the first clue that the Universe is expanding. This was called *Hubble's law* later [4]. Moreover, BBT predicted a "residual radiation from the Big Bang" in the sky today, with a temperature of about 3 K. In 1965, American astronomers *Arno Penzias* ans *Robert Wilson* detected this blackbody emission from all directions of the sky [5], i.e., the CMB. With the data collected by the cosmic background explorer (COBE) satellite, which was launched in 1989, the cosmological researches stepped from more theoretically-oriented discussions into the era of precision cosmology. Our understanding of the Universe has since then undergoing a fundamental change and update.

Besides, the BBT was supported by other evidences, first among others the abundance of light elements. Predictions of the nucleosynthesis that can be produced in the early stages of the Universe history has been corroborated by different observational data [6–8].

The Universe we can observe is limited. Because of the finite speed of light, the size of propagation of light in the time scale of the finite age of the Universe forms a sphere-like space centered on the observer, which is the *Hubble Volume*. Theoretically, the radius of it is much farther than the oldest celestial body ever found, with a diameter of about 93 billion light-years [9, page 27].

How does such observable Universe appear to us?

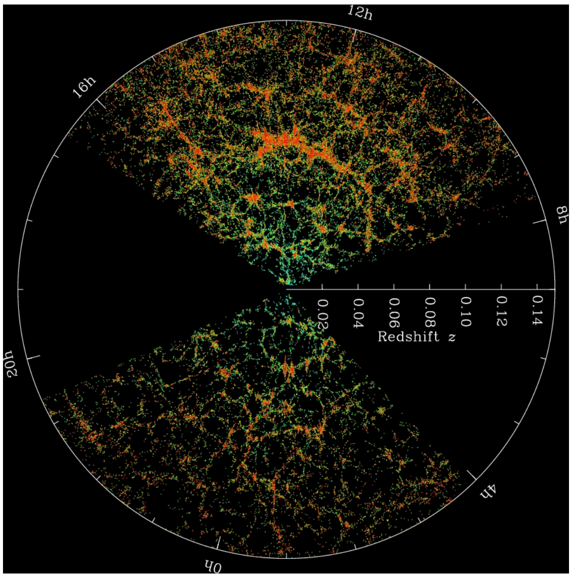

Figure 1.2: The cosmic scan image obtained by SDSS. Each point is a galaxy, with the color showing its g-r color. In the upper half of the figure, there is distinct giant wall-like structure, called Sloan Great Wall, at a redshift of about 0.06. The figure is taken from Ref. [10].

First evidence of the cosmological principle (i.e., homogeneity and isotropy on large scales) can still be traced back to Hubble. He measured the apparent magnitude and position of 400 extragalactic nebulae [11], and the results showed that their density in space was roughly uniform. Later, based on a richer catalog of galaxies called Shapley-Ames catalog, he found that the galaxy count exceeded the random Poisson distribution at an angle of about 10°, but agreed with the Gaussian distribution on larger scales [12]. This shows that the Universe may be clustered and clumpy on small scales, yet homogeneous on larger scale.

In 1982, the Center for Astrophysics Redshift Survey (CfA) completed data collection of about 2,400 galaxies observing all galaxies brighter than magnitude 14.5, in a total of 2.7 sr solid angle, at the north and south poles of the Milky way. The survey mission produced the first map with large area and medium depths, scanning three dimensional properties. From the data, one can recognize galaxy clusters and voids, the "Great Wall" and Filament structures. Fig. 1.1 shows one of the outcomes from CfA surveys. In the decade after 1985, CfA conducted a second survey of the sky, investigating the spectrum of 5,800 galaxies [13]. The shape of the "Great Wall" was better characterized and it revealed that the voids are common, with a density of about 20%. Thereafter, redshift surveys of multi-object spectrometers have been developed rapidly. They allow to observe hundreds of galaxies at the same time, while larger telescopes provide a profound understanding of low-luminosity or farther galaxies. The largest low redshift galaxy survey conducted so far is the Sloan Digital Sky Survey (SDSS) [14], which recorded data on nearly two million celestial bodies and scanned 8,000 square degrees of sky.

The Sloan Great Wall, discovered by SDSS in 2003, is the most giant gravitational bound system ever known, shaped like a wall, and has 1.38 billion light-years length. It is shown in the upper part of Fig. 1.2.

Surveys like SDSS have been offering an excellent mapping of the Universe and its LSS, revealing their unique features, and providing an enormous number of accurate observations for cosmologists to study the Universe formation and evolution.

Through the scanning observation of the large survey telescopes, leading to the production of numerous and large catalogs (for more survey data, see, e.g., galaxy redshift survey list[1]), it has been found that the observed (baryonic) matter such as galaxies and clusters, presents a bottom-up hierarchical structure. The first formed objects are small proto-galaxies and then in a hierarchical assembly one arrives after a few Gyr up to giant voids and super-clusters, vaster than $100\,\mathrm{Mpc}$.

Hubble expansion, CMB, Big Bang Nucleosynthesis (BBN) and the LSS characteristics observed by various surveys and multi-band electromagnetic radiation telescopes in recent years have become the four observational pillars of the BBT.

However, in spite of these achievements, there are still many open issues in the BBT. They include the problems of event horizon, flatness, baryon asymmetry, dark matter and dark energy. Among them, the last two share a great challenge in today's physics and astronomy. In another perspective, the widely accepted particle physics standard model, which constitutes the fundamental theory of nature, has to be extended, to introduce new particles or fields that can account for such phenomena. In its own, the model has different open questions, including in particular the gauge hierarchy problem, strong CP problem, neutrino masses.

Physicists hope that the solution of the microscopic and cosmological issues might be related. According to the latest cosmological results [15], the age of the Universe is 13.787 ± 0.020 billion years, dark energy accounts for $(68.47 \pm 0.73)\%$ of total energy content of the Universe, the rest of matter takes its $(31.53 \pm 0.73)\%$, where dark matter accounts for its $(26.45 \pm 0.27)\%$. Thus, most of the energy in the Universe has an origin

---

[1] https://www.astro.ljmu.ac.uk/ ikb/research/galaxy-redshift-surveys.html

which is mysterious to us.

In my thesis, I will describe how to collect and analyze the data from the *Fermi* Gamma-ray Space Telescope (*Fermi*), from CMB maps observed by the Planck spacecraft (Planck) and from galaxy of cluster catalogs obtained by large-scale surveys, in order to shed some light on the mystery of dark matter.

In chapter 2, I introduce the basic theoretical description of the formation of LSS on which this thesis is based, including the standard cosmological model, the thermal history of the Universe, statistics and evolution of density fluctuations. Chapter 3 is about some basic information and properties of dark matter. Chapter 4 describes the instruments and data acquisition for the observational data employed in this thesis. The next chapter 5 details the statistical methods which have been used and developed. They mainly involve Markov Chain Monte Carlo algorithms and the derivation of the two-point angular cross-correlation between two fields. In chapters 6 and 7, I will use the models, methodologies, and processed data discussed in the previous chapters, to constrain the γ-ray emission from galaxy clusters and WIMP dark matter, and the integrated Sachs-Wolfe effect. Chapter 8 summarizes the works, and describes how to proceed forward to the future researches with more accurate astronomical data, more effective analysis methods, and more refined theoretical models, to tackle the dark matter and dark energy problems. The last part of the thesis is occupied by the appendix, where some technical aspects are collected.

Chapter 2

The Formation of Large-Scale Structure

2.1 ΛCDM Model

The previous chapter 1 already mentioned that the modern cosmology is based on the theory of general relativity, proposed by Einstein in 1917. In general relativity, we use Einstein field equations to relate the geometry of the space-time of the Universe with the matter and energy content. They are generally expressed in terms of the stress-energy tensor $T_{\mu\nu}$, the Ricci tensor $R_{\mu\nu}$ (with R being the associated scalar), and the metric $g_{\mu\nu}$ as follows:

$$R_{\mu\nu} - \frac{1}{2} R\, g_{\mu\nu} = \frac{8\pi G}{c^4} T_{\mu\nu}, \tag{2.1}$$

where c is the speed of light and G is the Newton's constant.

The foundations of modern cosmology are given by the above equations and the cosmological principle, i.e.:

The Universe is isotropic (preserves SO(3) symmetry) and is homogeneous on the largest *scales.*

The isotropy refers to the rotational symmetry in any direction of the sky, and homogeneity is indicating the translational symmetry in space.

Based on the above two pillars, the Friedmann-Lemaître-Robertson-Walker (FLRW) metric defines the features of the Universe. It is given by

$$\begin{aligned} \mathrm{d}s^2 &= g_{\mu\nu}\mathrm{d}x^\mu x^\nu \\ &= c^2\mathrm{d}t^2 - a(t)^2\left[\frac{\mathrm{d}r^2}{1-\kappa r^2} + r^2(\mathrm{d}\theta^2 + \sin^2\theta\mathrm{d}\phi^2)\right], \end{aligned} \tag{2.2}$$

where t is time, $a(t)$ is the scale factor, representing the expansion of the Universe over time, and (r, θ, ϕ) are the comoving spherical coordinates.

Curvature κ can take on three possible values: $\kappa < 0$ defines a hyperbolic space, the Universe will be open; $\kappa = 0$ means Euclidean space, indicating a flat Universe; $\kappa > 0$ corresponds to an elliptical space and closed Universe.

Substituting the FLRW metric into the Einstein field equations, one can obtain the Friedmann equations [16], which describe the evolution of the Universe (c is set to be 1 here).

Time-time component gives

$$(\frac{\dot{a}}{a})^2 + \frac{k}{a^2} = \frac{8\pi G}{3}\rho + \frac{\Lambda}{3}; \tag{2.3}$$

and space-space component leads to

$$2\frac{\ddot{a}}{a} + (\frac{\dot{a}}{a})^2 + \frac{k}{a^2} = -8\pi G p + \frac{\Lambda}{3}, \tag{2.4}$$

where ρ and p are density and pressure of the matter-energy constant of the Universe, respectively. Λ is the cosmological constant.

The above two formulas can be combined to obtain:

$$\frac{\ddot{a}}{a} = -\frac{4\pi G}{3}(\rho + 3p). \tag{2.5}$$

To solve those evolution equations, we need information about the stress-energy tensor. Generally, we assume the Universe to be composed by perfect fluids which means:

$$p = \omega\rho. \tag{2.6}$$

The Friedmann equations and the equations of state for all the cosmological constituents provide a complete system of equations to describe cosmological dynamics.

The value of ω depends on the nature of the constituent. $\omega = 1/3$ corresponds to radiation, while $\omega = 0$ is the case of matter (both baryonic matter and DM).

The destiny of the Universe is determined by what it is made of, and the relative density of each component can be written as

$$\Omega_i = \frac{\rho_i}{\rho_c}, \tag{2.7}$$

ρ_i is the energy density of the component i, $\rho_c = 3H^2/8\pi G$ characterizes the critical density, which means the critical value between the expansion or contraction of the Universe.

If the Universe is flat, the sum of the relative densities of all substances is $\Omega_{\rm tot} = \sum_i \Omega_i = \Omega_\Lambda + \Omega_r + \Omega_m + \Omega_\kappa = 1$. $H(t)$ is the Hubble rate and it is defined through the scale factor:

$$H(t) \equiv \frac{\dot{a}(t)}{a(t)}. \tag{2.8}$$

Its value today is $H_0 = 100\ h\ \mathrm{km\ s^{-1}\ Mpc^{-1}}$ where h is a dimensionless constant.

The matter component consists of the sum of baryonic matter, cold DM, neutrinos, i.e., $\Omega_m = \Omega_b + \Omega_{\text{CDM}} + \Omega_\nu$. The density of the cosmological components are inferred from the Friedmann equation and are expressed through the critical density and Hubble rate displayed above:

$$\frac{H^2}{H_0^2} = \Omega_\Lambda + \Omega_\kappa(\frac{a_0}{a})^2 + \Omega_m(\frac{a_0}{a})^3 + \Omega_r(\frac{a_0}{a})^4, \tag{2.9}$$

$$\Omega_m = \frac{\rho_{m0}}{\rho_c}, \Omega_r = \frac{\rho_{r0}}{\rho_c}, \Omega_\Lambda = \frac{\Lambda}{3H^2}, \Omega_\kappa = -\frac{\kappa}{a^2H^2}. \tag{2.10}$$

Due to the expansion of the Universe, photons undergo a redshift in frequency as the distance from the observer increases over time,

$$1 + z = \frac{\lambda_{\text{obv}}}{\lambda_{\text{e}}} = \frac{a_{\text{obv}}}{a_{\text{e}}}, \tag{2.11}$$

where $a_{\text{obv}} = a_0 = a(t = 0)$, usually normalized to 1. λ_{obv} and λ_{e} are the photon wavelengths for the observation and emission, respectively.

From the redshift and Hubble constant definitions, we can integrate over time to get the age of our universe:

$$t_0 = \int \mathrm{d}t = \int_0^\infty \frac{\mathrm{d}z}{(1+z)H(z)}. \tag{2.12}$$

The physical distance between two points changes over time because of expansion. One can also define the so-called *comoving distance* as:

$$D_c = \int_0^r \frac{\mathrm{d}r}{\sqrt{1-\kappa r^2}} = \int_0^z \frac{\mathrm{d}z}{H(z)}. \tag{2.13}$$

2.2 A Brief History of the Universe

Our universe started from a extreme hot and dense plasma at Planck time $t \sim 10^{-43}$ seconds, with temperature of 10^{32} K, earlier phases of the Universe are not known, since we would need a theory combining together quantum and gravity descriptions.

When it comes to 10^{-36} seconds, and the temperature is around 10^{27} K to 10^{28} K, an inflationary phase occurred [17, 18]. *Inflation* increased the linear size of the Universe by more than 60 "e-folds", or its volume increased by a factor of at least 10^{78}[1].The proposal of inflation gives solution to many problems, such as horizon, flatness, homogeneity, isotropy and primordial monopole problem [19–25]. The latest result of Planck collaboration [15] points towards a flat Universe, with $\Omega_\kappa = 0.001 \pm 0.002$ today, where $\Omega_{\text{tot}} = 1 - \Omega_\kappa$. If the total energy density is close to 1, then, going back in time, it should have been even closer to 1, according to equation 2.10. This is a fine-tuning problem, and it seems very unnatural outside the context of inflation. This problem is solved by the exponential expansion, such that any curvature was diluted and the space became flatter.

The horizon problem arises from the observation of the homogeneity between sky regions that are not causally connected. In order to solve this observational phenomenon, there must had been a causal relationship in the past between those regions. The inflation mechanism stretches the spatial scale in a very short time through a huge expansion rate. Due to that, regions that were causally connected before inflation become disconnected.

---

[1] e-folds number $N(t)$ is defined by $a(t) \sim \exp(\int \mathrm{d}tH) = e^{-N(t)}$

After inflation, the Universe cooled down with the expansion in a less dramatic way, and particles formerly in the plasma gradually go out of equilibrium. The perfect symmetries of the beginning of the Universe started to break. e.g., the weak and electromagnetic interactions decoupled from each other when the temperature drops to 10^{15} K.

A relevant stage in the history of the Universe is the BBN. As the photon energy diminishes, it cannot break the nuclear bounds of the light nuclei any longer, and the first element, Deuterium ^{2}H, is created. Then it is followed by helium ^{3}He, ^{4}He, ^{7}Li and some unstable elements such as tritium ^{3}H, ^{7}Be. The calculation of helium abundance is one of the most important proof of the Big Bang theory [15]. The thermonuclear reaction ends when the kinetic energy of all the particles is insufficient to overcome the Coulomb barrier between the nuclei.

About a few tens of thousands of years after BBN, the Universe went from radiation-dominated to the matter-dominated era, and photons become less dense and energetic. The recombination period is when essentially all the free electrons and photons are combined into the neutral atoms. At a temperature of about $3,000$ K, the last scattering between free electrons and photons occurred, when about 380,000 years passed after the Big Bang. Once radiation decoupled from matter, photons could travel almost freely and survive to today to be eventually detected by us. The redshift of the last scattering sphere (which is actually not a surface but has a certain thickness since the decoupling is not instantaneous) is around $z \sim 1100$. The black-body CMB radiation has been detected very precisely with the today temperature being 2.726 K [26].

After CMB decoupling, there is a *Dark Age* at $10 < z < 1000$ where no luminous celestial body can be seen in the Universe, until the first stars lit up at about $z = 20 \sim$

30. Galaxies are created very early in the Universe by tiny density perturbations that cause primordial seeds to collapse as gravity condenses the mass of the surrounding matter. The subsequent growth of nonlinear structures arises from the first generation of gravitational bound bodies, allowing the Universe to shine full of galaxies, clusters, and inter galactic medium. We describe the evolution of perturbations in the following.

2.3 Linear Perturbation Theory

Although homogeneity is valid on large scales based on the cosmological principle, there are structures such as galaxies, clusters, and super-clusters on relative smaller scales. It is thought that very small quantum perturbations produced in the earliest stages of the Universe led to fluctuations in the density of primordial matter, which then grew due to the action of gravity. From linear evolution to the nonlinear phase, the Universe gradually formed structures on different scales.

The *Newton's linear perturbation theory* approach allows to describe the gravitational collapse in several relevant cosmological cases, in particular at large scales. At small scales, for large overdensities, perturbations enter the non-linear regime. Opposite limit is when the perturbation scale is larger than the horizon, and Newton's Perturbation theory is no longer applicable, requiring perturbation theory under general relativity.

A perturbation to the background FLRW metric (introduced in section 2.1) can be described by the metric:

$$g_{\mu\nu} = \bar{g}_{\mu\nu} + \delta g_{\mu\nu}, \tag{2.14}$$

where $\bar{g}_{\mu\nu}$ is the unperturbed FLRW metric, and $\delta g_{\mu\nu}$ represents the perturbation term.

The background metric depends only on time, while the disturbance can change both in time and space. Since it is symmetric under spatial rotation, the metric disturbance has 10 degrees of freedom. Four of them are scalars, another four are vectors and the last two are tensorial. This classification follows from the transformation properties in a three dimensional space. Scalar perturbations govern the process of LSS formation, vector terms attenuate with the expansion of the Universe, and tensors lead to gravitational waves. Although perturbations can be decomposed, their form is very complex (see Ref. [27, chapter 5] for more details). Their evolutions are generally solved by numerical methods or linearized gravity.

From the tiny perturbations to the conspicuous structures, there are two kinds of competing interactions acting: on the one hand, due to the gravitational effect, small fluctuations in the primary density can attract and enhance the amplitude; on the other hand, it is weakened by radiation or gas pressure, high speed free collisions of relativistic particles and the stretching of the expansion of the Universe. The CMB anisotropies are a sign that small inhomogeneities existed in the early universe and they can be the seeds for structure formation.

For LSS formation, i.e., on the scales of galaxies and clusters, studied in this thesis, the essence of the process can be nicely explained by using Newton's perturbation theory. To derive relevant equations, one can add disturbance (small) terms to the velocity, stress tensor, pressure, density, Newtonian gravitational potential field, entropy and other physical quantities. We define $\delta = \delta\rho/\rho_0$, and below we will expand at first order in δ since $\delta \ll 1$, so higher orders are negligible.

The beginning of this theory is based on an assumption of fluid who has density and velocity continuity equation:

$$\dot{\rho} + \nabla \cdot (\rho v) = 0, \tag{2.15}$$

and Euler equation in fluid dynamics

$$\dot{v} + (v \cdot \nabla)v + \frac{1}{\rho}\nabla\rho + \nabla\phi = 0. \tag{2.16}$$

Fluctuations in the gravitational potential ϕ satisfy the Poisson equation:

$$\nabla^2\phi = 4\pi G\rho. \tag{2.17}$$

The entropy conservation equation is

$$\dot{s} + (v \cdot \nabla)s = 0. \tag{2.18}$$

When plugging such disturbance terms into the above equations 2.15, 2.16, 2.17 and 2.18, at the first-order we have

$$\dot{\delta} + \frac{1}{a}\nabla \cdot [(1+\delta)v] = 0, \tag{2.19}$$

whereas the evolution of the density at zero-th order reflects the background evolution of matter $\rho_0 \approx a^{-3}$.

In the adiabatic case, also known as isentropic case, there is $\frac{\sigma}{\rho_0}\nabla\delta s = 0$, and the second-order derivative in time of the disturbance is given by

$$\ddot{\delta} = \frac{v_s^2}{a^2}\Delta\delta - 2H\dot{\delta} + 4\pi G\rho_0\delta. \tag{2.20}$$

The three terms on the right-hand side in equation 2.20 represent three different effects. They are, respectively, the propagation of vibrations in the form of sound waves created by the baryon pressure, the damping caused by the expansion of the Universe and the gravitational term. The sound velocity is given by $v_s^2 \equiv (\partial p/\partial \rho)_s$, and its effect can be physically "imaged" by observing the Baryon Acoustic Oscillations (BAO).

Performing a Fourier transformation, by introducing the wavenumber k and physical wavenumber $k' \equiv k/a$, and ignoring the expansion damping term in equation 2.20, we have

$$\ddot{\delta} + (v_s^2 k'^2 - 4\pi G\bar{\rho})\delta = 0. \tag{2.21}$$

The above equation has solution

$$\delta = \delta_k \exp\left[\sqrt{4\pi G\bar{\rho}(1 - \frac{\lambda_J^2}{\lambda^2})t}\right], \tag{2.22}$$

and it also satisfies the dispersion relation $\omega^2 = k^2 v_s^2 - 4\pi G\rho_0$.

In equation 2.22, the critical wavelength λ_J is called *Jeans wavelength*, and it is defined as

$$\lambda_J = v_s\sqrt{\pi/G\rho_0}. \tag{2.23}$$

For wavelength $\lambda > \lambda_J$, the density increases exponentially with time until the collapse. For small wavelength of $\lambda < \lambda_J$, the matter density oscillates due to sound wave propagation. On the contrary, the effect of sound waves slows down the growth of the disturbance. The above section is slightly changed when the damping factor $-2H\dot{\delta}$ (due to the expansion of the Universe), but the essence of the behavior is the one just outlined.

In the previous discussions, we have learned that in the very early universe, about $z > 10$, all perturbations can be considered on stages of linear evolution. To describe the evolution in shape of the disturbance spectrum, we can use the linear transfer function:

$$T(k) \equiv \frac{\delta(k,t)}{\delta(k,t_i)G(k,t_i)}, \tag{2.24}$$

$$\delta(k,t) = \delta_0 \frac{G(t)}{G(0)} = \delta_0 G, \tag{2.25}$$

where G is the linear *Growth factor* (normalized to one at $t = 0$), and the suffix i in t_i means the initial time. $T(k)$ gives the ratio of the late-time amplitude of a mode to its initial value. Fig. 2.1 shows the linear transfer functions for different cosmological scenarios where the Universe is matter dominated, since it is the situation from last scattering to recent times. The isocurvature perturbation are divided into the cold DM (iso CDM) and baryonic (iso baryons) terms. In the adiabatic case, from left to right are baryons, hot DM (HDM), mixed DM (MDM, 30% hot+70% cold) and cold DM (CDM), respectively, all starting at $T(k) = 1$. They all decrease at large k, which is indicating that the disturbance decays rapidly at small scales. The oscillations in the baryonic case reflect the acoustic wave oscillation. The cutoff scale is related to the minimum mass of the first generation of structures, with the smallest being for the CDM case and the largest for the baryonic case. Therefore, for a CDM universe, structures start to cluster at small scales, then the effect of gravity makes matter gradually to merge into larger objects, leading to a hierarchical clustering model.

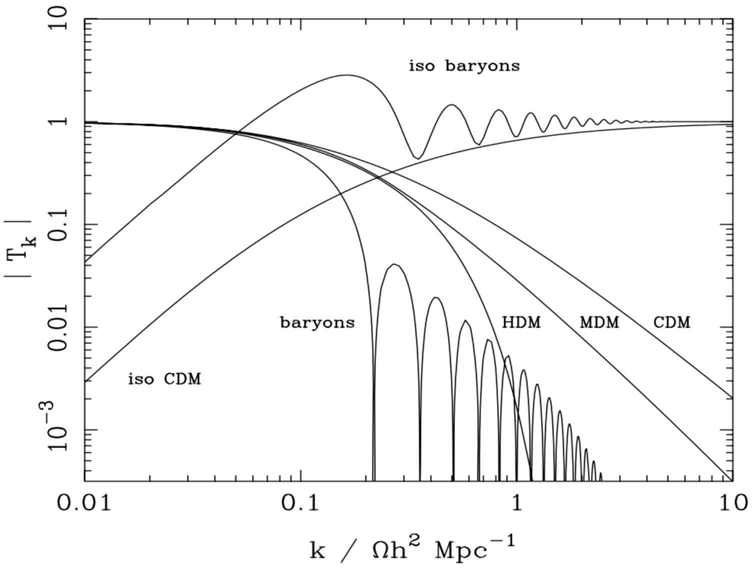

Figure 2.1: Linear transfer functions of various types, the adiabatic disturbance, from left to right are baryons, hot DM (HDM), mixed DM (MDM, 30% hot+70% cold) and cold DM (CDM), respectively. The figure is taken from Ref. [28].

If we describe the initial disturbance as random noise, then the phases of the different Fourier modes δ_k are uncorrelated and random. According to the Central Limit Theorem, the sum of a large number of independent random variables can be described by a Gaussian Probability Distribution Function (PDF) and the PDF of density fluctuations is given by

$$f(\delta) = \frac{1}{\sqrt{2\pi}} G(z)\sigma_M \exp\,[-\frac{\delta^2}{2G^2(z)\sigma_M^2}]. \tag{2.26}$$

To have a quantitative estimate of the magnitude of density fluctuations, one can compute the variance of the initial density fluctuation field in a sphere of radius R, randomly selected in the whole space.

Let us first introduce the so-called *Power Spectrum* $P(k) = \langle|\delta_k|^2\rangle$ which is the

Fourier transform of the two-point correlation function. The variance of the mass fluctuations σ_M can be obtained with

$$\sigma_M^2(R) = \frac{V}{2\pi^2} \int_0^\infty P(k) W^2(kR) k^3 \mathrm{d} \log k, \tag{2.27}$$

where $V = 4\pi R^3/3$ and $W(kR)$ denotes the Fourier transform of the filtering window function on the mass scale of a sphere with radius R. Here, we adopt a top-hat filter (in physical space) which in Fourier space reads:

$$W(kR) = \frac{3}{(kR)^3}[\sin kR - kR\cos(kR)]. \tag{2.28}$$

The relationship between power spectrum at the end of the linear evolution stage and the initial power spectrum is

$$P(k, t_f) = T^2(k)\, P(k, t_i) G^2(t_i, t_f), \tag{2.29}$$

where the t_f indicates the final time in calculation.

The road towards understanding the formation of LSS in the linear regime narrows down to the determination of the form of power spectrum for primordial disturbances. It is generally believed that the original density disturbance is produced from the vacuum quantum fluctuations produced by inflation. This predicts the field to be a uniform isotropic Gaussian random field (as already assumed above), implying a (nearly) scale invariant power spectrum, which reads:

$$P(k) = A\, k^n, \tag{2.30}$$

where A is the amplitude of normalization spectrum, n is its index, and scale-invariance means $n \simeq 1$. This corresponds to adiabatic perturbations and $n = 1$ is the Harrison-Zel'dovich spectrum [29, 30].

2.4 Non-Linear Perturbation Evolution

The density perturbation at the last scattering is approximately $\delta = \delta\rho/\rho \sim 10^{-5}$ and in a matter dominated Universe grows as $\delta \approx t^{2/3}$. This is valid until $\delta \ll 1$. Let us now briefly describe the collapse in the non-linear regime, under the assumption of spherical accretion. The spherically symmetric model is clearly an ideal picture because most perturbations are actually asymmetric, but it is instructive.

The local scale factor of the collapse model is

$$(\frac{\dot{a}}{a(t)})^2 = H^2(t)\left[\Omega_p(t)\frac{a(t)}{a} + 1 - \Omega_p(t)\right], \tag{2.31}$$

where the relative density is $\Omega_p(t) = \rho(t)/\rho_c(t)(1+\delta(t))$ and the curvature is positive. $\rho_c(t)$ expresses the critical density changing over time.

For such a model with a spherically symmetric perturbation region in the background of an expanding universe and a zero cosmological constant, the standard solution of Friedmann equations can be obtained through the parametrization

$$a(\theta) = A(1-\cos(\theta)), \tag{2.32}$$

$$t(\theta) = B(\theta - \sin(\theta)), \tag{2.33}$$

where A and B are the constant that can be expressed as $A = a(t)\Omega_p(t)/[2(\Omega_p(t)-1)]$ and $B = \Omega_p(t)/[2H(t)(\Omega_p(t)-1)]$.

The physical meaning can be summarized as follows.

- Expansion: When $\theta < \pi$, the sphere expands due to the expansion of the small perturbation regime;

- Turnover: When $\theta = \pi$, the sphere reaches the maximum radius and start collapsing inward, i.e., in a direction opposite to the expansion of the Universe;
- Virialization: When $\theta = 3\pi/2$ then $\delta = 1$ and this is the linear to nonlinear turning point;
- Collapse: $\theta = 2\pi$ is a mathematical singularity (infinite density) while physically it corresponds to virialization (at a finite density). In other words, one can see that the kinetic energy and potential energy in the sphere reach the equilibrium condition, $|U| = 2K$. At virialization point, the overdensity of the object respect to the background density turns out to be $\Delta_{\mathrm{vir}} \simeq 178$ and the initial overdensity required to an object to collapse is $\delta_c = 1.686$. This is the critical value for virialization. When considering density field of $\delta(\vec{x}, t) = \delta_0(\vec{x})G(t)$, the structure must satisfy $\delta_0(\vec{x}) > \delta_c/G(t) \equiv \delta_c(t)$, in order to form a DM halo.

Introducing a smooth density disturbance field (to consider that what you can measure is a density perturbation smoothed over some volume, not a perturbation at a point)

$$\delta_s(\vec{x}; k) \equiv \int \delta_0(\vec{x}')W(\vec{x} + \vec{x}'; R)\mathrm{d}^3\vec{x}' \tag{2.34}$$

where $W(\vec{x}+\vec{x}'; R)$ is also the filtering window function, and assuming Gaussian density fields, then the probability of $\delta_s > \delta_c(t)$, i.e., for the perturbation to be part of a collapsed object of mass $> M$, is

$$\begin{aligned} P(\delta_s > \delta_c(t)) &= \frac{1}{\sqrt{2\pi}\sigma(M)} \int_{\delta_c(t)}^{\infty} \exp\left[-\frac{\delta_s^2}{2\sigma^2(M)}\right] \mathrm{d}\delta_s \\ &= \frac{1}{2}\left[1 - \mathrm{erf}(\frac{\delta_c(t)}{\sqrt{2}\sigma(M)})\right], \end{aligned} \tag{2.35}$$

where $\sigma(M)$ can be transfer from equation 2.27.

Now we want to derive how many halos are formed as a function of the mass. Let us choose a volume of V and a number density distribution $N(V)\mathrm{d}M$, so that the mass in a unit of volume is

$$N(M)M(M)|\frac{\partial F}{\partial M}|\mathrm{d}M = \bar{\rho}|\frac{\partial F}{\partial M}|\mathrm{d}M, \tag{2.36}$$

with F being the fraction of the Universe collapsed into objects with mass $> M$ that can be obtained from equation 2.35.

Considering equation 2.30 for the power spectrum of the density disturbance, the Press-Schechter (PS) mass function turns out to be:

$$N(M) = \frac{2\alpha\bar{\rho}}{\sqrt{\pi}M_*}(\frac{M}{M_*})^{(\alpha-2)}\exp\left[-(\frac{M}{M_*})^{2\alpha}\right]. \tag{2.37}$$

It is also often expressed in terms of the multiplicity function that, defining $\nu = \delta_c/\sigma_M$, is

$$\nu f(\nu) = 2(\frac{\nu^2}{2\pi})^{1/2}\exp{(-\frac{\nu^2}{2})}. \tag{2.38}$$

The Press-Schechter formalism is in qualitative agreement with galaxy and cluster surveys for the number of collapsed objects and their mass distribution and time evolution. This confirms the *hierarchical/bottom-up* structure formation.

The spherical model is a simple description, but not compatible with precision cosmology data. A more realistic picture is provided by the ellipsoidal collapse model [31], where the multiplicity function is given by

$$\nu f(\nu) = 2A\left[1+\frac{1}{(a\nu^2)^q}\right](\frac{a\nu^2}{2\pi})^{1/2}\exp{(-\frac{a\nu^2}{2})}. \tag{2.39}$$

Both models depend on the underlying cosmological model. For example, the α parameter in the Press-Schechter model comes from the power-law index of the disturbance mass spectrum and is a result of the linear evolution stage, including the shape of the original spectrum and the transfer function. Typically such parameters are derived from numerical simulation results, and the halo mass function is a sort of fit with analytical function to the numerical simulation results. In my works, we used the ellipsoidal model (Sheth-Tormen). Fig. 2.2 and Fig. 2.3 represent the above two mass functions and the simulation results from the collaboration SDSSDR14 (called Comparat2017 model, beacuse released in 2017) [32], respectively. In these two figures, the solid lines represent the Press-Schechter model; the dotted lines are from the Sheth-Tormen model; Comparat2017 model can be seen from dashed lines. Different colors represent different masses or redshifts as illustrated in the legend.

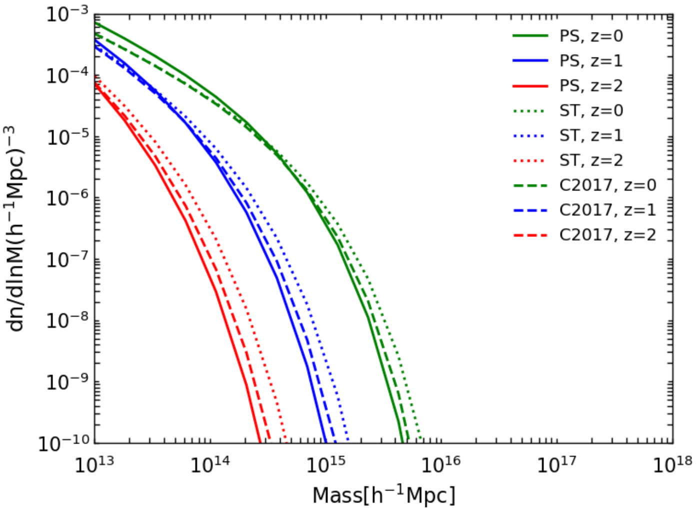

Figure 2.2: The dependence of the three mass functions on the halo mass for Press-Schechter (PS), Sheth-Tormen (ST) and Comparat2017 (C2017) models.

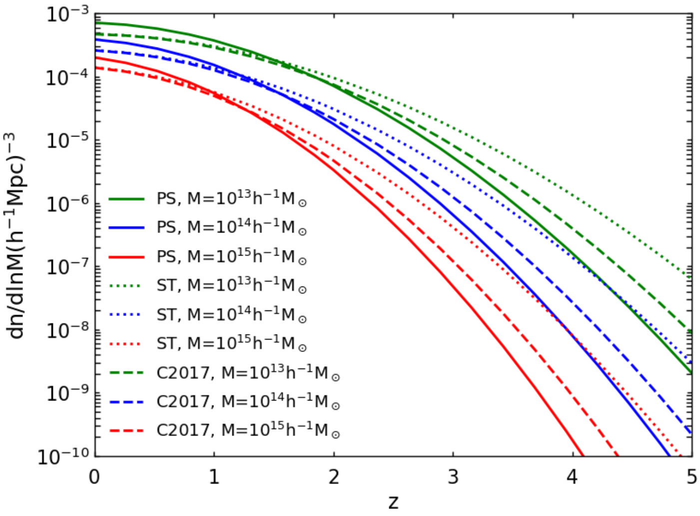

Figure 2.3: The dependence of the three mass functions on redshift for Press-Schechter (PS), Sheth-Tormen (ST) and Comparat2017 (C2017) models.

2.5 Dark Matter Halo Density Profile

The spatial profile of a single DM halo depends on the initial density distribution and can be derived from describing the collapse in spherically symmetry. The latter is a good approximation, even though numerical simulations tends to find slightly oblate or prolate profiles. The halo density profile that is most commonly adopted in the literature is the one from Ref. [33], that can be written as

$$\rho(r|m) = \frac{\rho_s}{(\frac{r}{r_s})^{\alpha}(1+\frac{r}{r_s})^{\beta}}. \tag{2.40}$$

The parameters r_s and ρ_s represent the scale radius and normalization of the density, respectively. This formula have been extensively applied to describe DM in galaxies. The values of α and β can be determined by simulation. When $\alpha = 1$ and $\beta = 2$, then it corresponds to the well-known Navarro-Frenk-White (NFW) profile.

At the time of writing, the precise description of the halo profile at small scales (e.g. the inner part of a galaxy) is still widely debated. Fig. 2.4 shows the three examples of common halo profiles: the green line is the NFW profile; blue is from Einasto model [34]; and red is taken from Diemer2014 model [35]. It can be seen that at intermediate scale, the three models are identical and overlap with each other. Only when the radius is extremely large or small, they show clear differences.

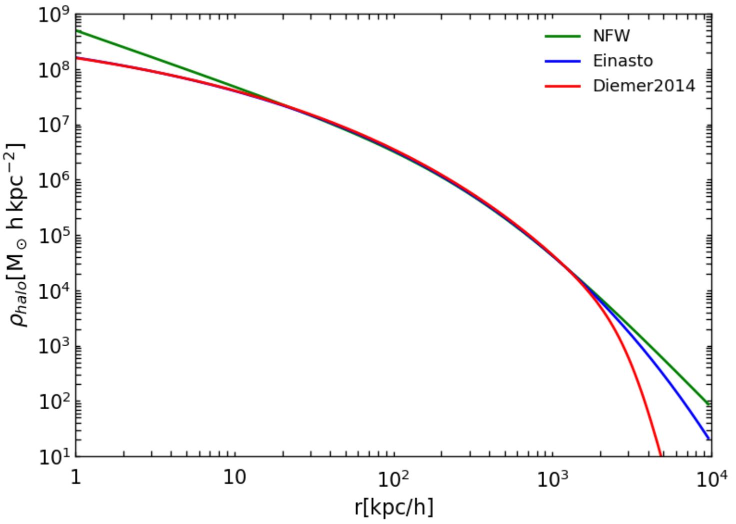

Figure 2.4: The dark halo density profile functions on radius r for NFW, Einasto and Diemer2014 models.

In simulations, the halo mass is often defined as the mass inside the radius of virialization

$$m \equiv \int_0^{r_{\rm vir}} \mathrm{d}r 4\pi r^2 \rho(r|m). \tag{2.41}$$

For the NFW model, there are

$$m = 4\pi\rho_s r_s^3 \left[\ln(1+c) - \frac{c}{1+c}\right], \tag{2.42}$$

where $c \equiv r_{\rm vir}/r_s$ is the concentration parameter.

In the following calculations, we will use the Fourier transform of the halo profile:

$$u(\mathbf{k}|m) = \frac{\int \mathrm{d}^3\mathbf{x}\rho(\mathbf{x}|m)e^{-i\mathbf{k}\cdot\mathbf{x}}}{\int \mathrm{d}^3\mathbf{x}\rho(\mathbf{x}|m)}. \tag{2.43}$$

Due to the spherical symmetry and considering the truncation at viralization radius, it reduces to:

$$u(k|m) = \int_0^{r_{\rm vir}} \mathrm{d}r 4\pi r^2 \frac{\sin kr}{kr}\frac{\rho(r|m)}{m}. \tag{2.44}$$

There is an analytic solution for the NFW profile [36]:

$$\begin{aligned} u(k|m) =& \frac{4\pi\rho_s r_s^3}{m}\{\sin(kr_s)\left[\mathrm{Si}([1+c]kr_s) - \mathrm{Si}(kr_s)\right] \\ &+ \cos(kr_s)\left[\mathrm{Ci}([1+c]kr_s) - \mathrm{Ci}(kr_s)\right] - \frac{\sin(ckr_s)}{(1+c)kr_s}\}, \end{aligned} \tag{2.45}$$

where

$$\mathrm{Ci}(x) = -\int_x^\infty \frac{\cos t}{t}\mathrm{d}t, \tag{2.46}$$

and

$$\mathrm{Si}(x) = -\int_x^\infty \frac{\sin t}{t}\mathrm{d}t. \tag{2.47}$$

The halo profile and its Fourier transform can be also written in terms of the dark halo concentration and mass, by using the above relations and a model for the concentration. In chapter 6, we will need the Fourier transform of the square of the NFW density profile, whose analytic form is in the appendix C. Fig. 2.5 shows the Fourier transform of NFW density profile, with the dark halo mass decreasing from left to right, and with the maximum value of $u(k|m)$ in the wavenumber space normalized to 1 (as clear from equation 2.43).

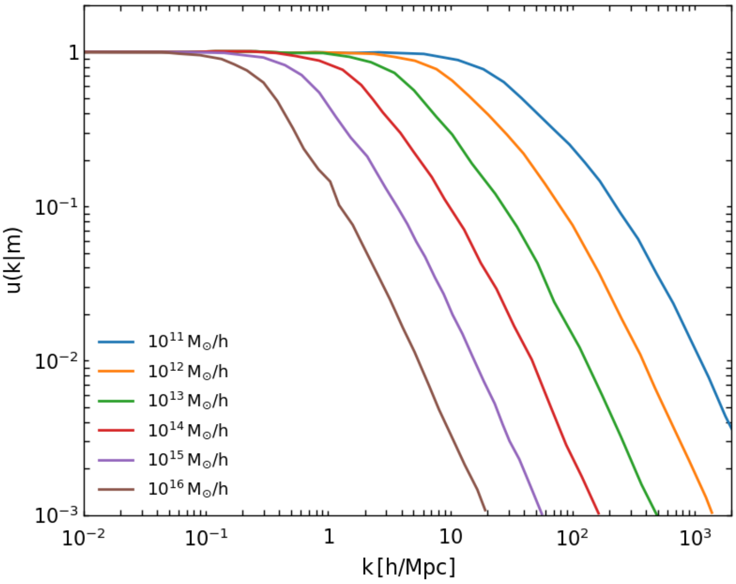

Figure 2.5: The Fourier transform function of the NFW density profile for different halo masses.

2.6 Dark Matter Halo Bias

Throughout the thesis we will adopt the halo model and compute signals from DM halos. If DM halos exactly follows fluctuations of the background density and are formed only under the action of the gravitational field, then their number density would be an unbiased tracer of the fluctuation of the DM density,

$$(\frac{\delta n}{n}) = (\frac{\delta \rho}{\rho}). \tag{2.48}$$

In the spherical collapse model, the probability of forming a halo is related to the initial density field [37]. The perturbation term can be divided into peak and background value, then according to the collapse of the basic threshold to determine whether add a bias factor or not. Therefore, the bias factor $b(M)$ of the halo can be expressed as:

$$\frac{\delta n_M}{n_M} = [1 + b(M)]\, \delta. \tag{2.49}$$

The bias factor depends on the mass function model. In the PS model, we have

$$b_h(M) = 1 + \frac{\nu^2 - 1}{\delta_c}, \tag{2.50}$$

while for the Sheth-Tormen mass function adopted in this thesis

$$b_h(M) = 1 + \frac{a\nu^2 - 1}{\delta_c} + \frac{2p}{\delta_c\,[1 + (a\nu^2)p]}, \tag{2.51}$$

where $a = 0.75$ and $p = 0.3$ are fitting parameters, derived from numerical simulations.

The Fig. 2.6 shows three models of halo bias factor: blue is from Ref. [38] (sheth01), orange line comes from Ref. [39] (thinker10) and green is taken from Ref. [32] (comparat17).

Equivalently, also galaxies and clusters also have deviations from density disturbances, know as galaxy/cluster bias $b_g = \delta_g/\delta$, in the linear, local cases. It leans on the size, luminosity, shape, color and redshift of the galaxy or cluster, and the form used will be specified later on when describing the analysis.

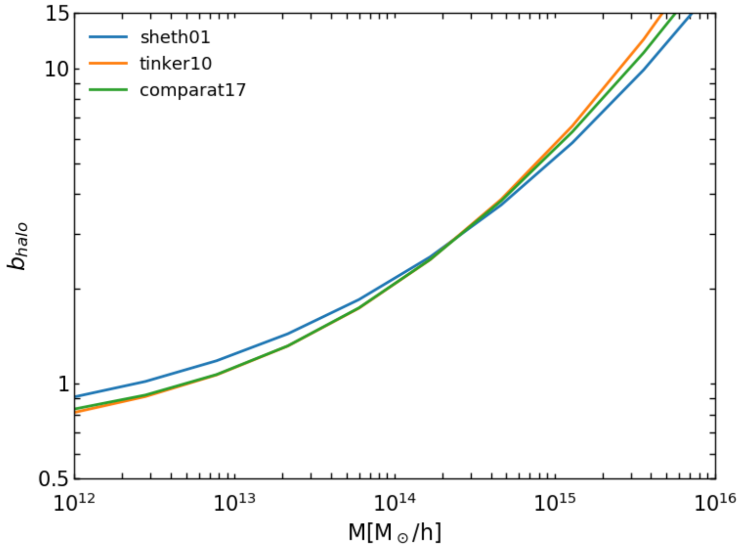

Figure 2.6: The dark matter halo bias factor function on mass for sheth01, thinker10 and comparat17 models.

2.7 Halo Occupation Distribution

The Halo Occupation Distribution (HOD) is a model relating the spatial distribution of galaxies to the distribution of DM halos, in order to understand how the former ones occupy the latter ones. HOD modeling can provide a deeper understanding of the relation between galaxy light and DM halo mass. The HOD is determined by the efficiency of galaxy formation and by the way galaxies fill the halos [40]. Thus the HOD depends on the process of galaxy formation, and it can change with the luminosity, shape and color of galaxies and clusters. These properties can be used as information to shape the HOD.

An HOD model is defined by three quantities:

1. The conditional probability $P(N|M)$ of a certain number N of galaxies in Halo viralized mass M;
2. The relative distribution of dark halos and galaxies in space;
3. The relative distribution of dark halos and galaxies in velocity.

Generally, the theoretical methods to sketch HOD are: semi-analytical model of galaxy formation, high resolution N-body simulation and hydrodynamical simulation. Here we introduce the first one.

This kind of model separates the central galaxy from the satellite region that contains multiple galaxies. Concerning the central galaxy, one parameterization consists to have a sharp transition between 0 and 1, when the halo mass is above a minimum threshold M_{min}. A smoother transition can be set with the function $\exp(-M_{\text{min}}/M)$ to test the sensitivity of the results to the sharpness of the central galaxy threshold. The HOD is parametrized as the contributions from two parts: central and satellite galaxies to the total number of galaxies in a halo: $N = N_{\text{cen}} + N_{\text{sat}}$. The central galaxies is

$$\langle N_{\text{cen}} \rangle_M = \frac{1}{2}\left[1 + \text{erf}\left(\frac{\log M - \log(M_{\text{cut}})}{\sigma_{\log M}}\right)\right], \tag{2.52}$$

where $\sigma_{\log M}$ is the width to set the transition from 0 to 1 for the central galaxy. The HOD of satellite galaxies in a halo mass M can be described by:

$$\langle N_{\text{sat}} \rangle_M = \begin{cases} \exp(-\frac{M_{\text{cut}}}{M - M_{\text{min}}})(\frac{M}{M_1}), & M \geq M_{\text{min}} \\ 0, & M < M_{\text{min}} \end{cases} \tag{2.53}$$

where M_{cut} in equation 2.52 and 2.53 is a mass cutoff of the power law relation of satellite galaxies, which governs the transition to the no-satellite galaxies case. The number of satellite galaxies is determined by a power-law with index α and normalization mass M_1.

For a given population of galaxies the HOD can be determined by fitting the above model to the correlation data from the sky survey [41], see Fig. 2.7.

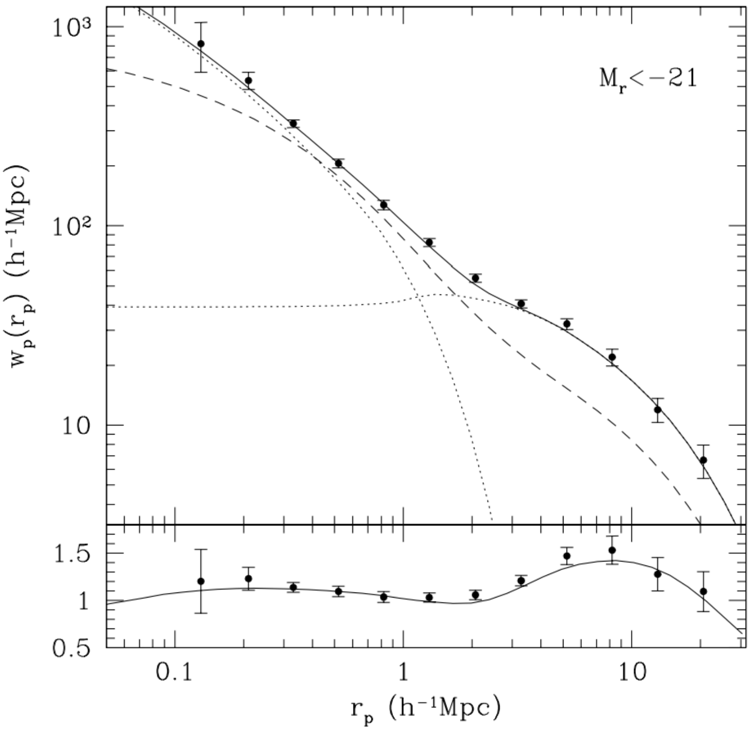

Figure 2.7: Projected correlation function for the absolute magnitude $M_r < -21$ samples, together with that for the best fitting HOD model for the SDSS survey. The dotted curves represent the contributions from 1 halo and 2 halo terms of the HOD model, and the dashed curve shows the projected correlation function for the matter computed from the nonlinear power spectrum of Ref. [42]. The deviation of the HOD model from data is shown in the bottom panel. The figure is taken from Ref. [41].

CHAPTER 3

Dark Matter Evidences and Candidates

The name "Dark Matter" was first proposed by the Swiss-American astronomer *Fritz Zwicky*, who in 1933 investigated the velocity of galaxies in the Coma cluster. Using the virial theorem he found a mass-to-light ratio around 400 times larger than that of ordinary spiral galaxies [43], suggesting the presence of an invisible mass component. Although the observations performed at that time resulted then to be inaccurate, and the mass that can be determined today is lower than such older estimates, the concept of DM introduced by Zwicky corresponds to the one that nowadays is thought to be one of the greatest mysteries in physics. Other more reliable evidences of the existence of DM have been accumulated over the past decades and are briefly outlined in the next section.

3.1 Evidences for Dark Matter

So far, no direct evidence of the existence of DM has been derived, but there is a large amount of indirect astronomical evidences. The first solid observational proofs for this conundrum occurred more than forty years ago. Hereafter I list a few major ones.

3.1.1 Galaxy Rotation Curve

As mentioned in the introduction, the motion of stars in galaxies is non-relativistic and can be described by Newtonian dynamics. Let us call R the radius of a sphere where visible matter is concentrated inside a galaxy. Inside such sphere along the disk of the galaxy, the velocity of matter rotating around the center increases linearly with the distance. When the distance becomes larger than R, the gravitational force should decrease with the distance from its center, according to Newton's law. The velocity of stars revolving around the center of a galaxy should therefore decrease as $r^{-1/2}$ when their distance r is larger than R. On the other hand, observationally it has been found to flatten instead of decreasing.

The American astronomer *Vera Rubin* discovered this phenomenon by measuring the rotation curve of Andromeda Galaxy M31 [44]. Although no light has been observed from the periphery of the galaxy, some additional mass providing the gravitational force needed to explain the rotational energy seemed to be necessary. This showed that the total amount of matter we have observed through light is not consistent with the actual mass responsible for gravitational attraction. Fig. 3.1 is a typical example, and it indicates that only after adding the contribution of a DM halo, one can match the observed

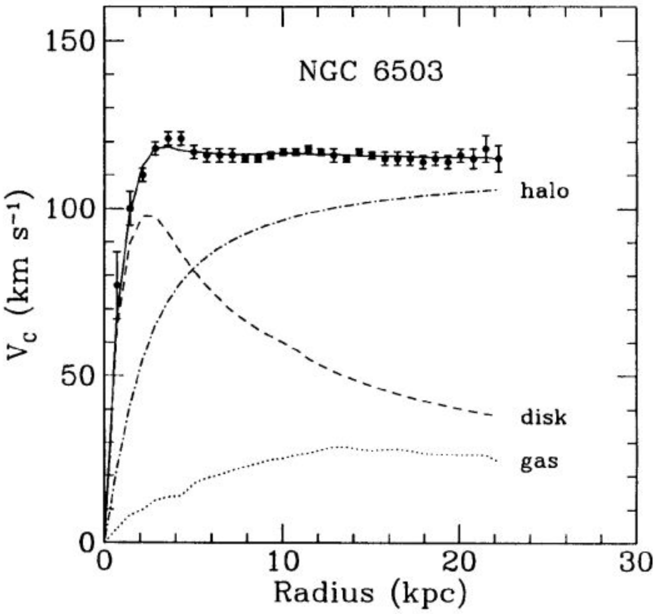

Figure 3.1: Rotation curve of NGC 6503 galaxy, the points with error bars are the observed data. The two curves of 'halo' and 'disk' are marked below is from the contributions of halo and galactic disk, respectively. Only by addition of the two terms can well fit the observed curves. The figure is taken from Ref. [45].

rotation curve [45]. A different point of view is to suggest that such observations may be the effect of the fact that Newtonian gravity is no longer applicable on such large scales. There are several models of modified gravity built to explain the rotation curve of galaxies, with the most popular being Modified Newtonian Dynamics (MOND) [46]. Such models typically face non-trivial issues on cosmological scales, and in general they struggle to explain the gravitational anomalies at different scales simultaneously. In this thesis, we will only consider the DM hypothesis.

Figure 3.2: This is the gravitational distortion of galaxy cluster CL 0024+17 observed by Hubble space telescope in November 2004. Although DM is invisible, its existence is inferred by drawing the distorted shape of background galaxies. The figure is taken from Ref. [47].

3.1.2 Gravitational Lensing

According to general relativity, when light encounters a massive object, the propagation path along the geodesic would show a 'bending', and this is known as gravitational lensing. Theoretically, any object with mass can bend light, but in order to produce a detectable effect a mass of the order of astrophysical structures is required. The mass determination through gravitational lensing occurs in a direct way from astronomical images and do not lean on specific assumptions in the description of the dynamics or of the visible component.

In Fig. 3.2, we show an example, the Hubble image of galaxy cluster CL 0024+17 [48]. Distortions of galaxy shapes are present, due to the lensing effect produced by the DM mass. This allows to reconstruct the DM distribution (blue pattern).

3.1.3 Bullet Cluster

Bullet cluster is a system made up of two galaxy clusters that collided and are now separating from each other after the collision. The matter component in form of galaxies of two clusters pass through each other without hindrance, but the gas medium is slowed down due to viscosity resistance. Since the intergalactic medium gas is the dominant mass component of the visible matter in a cluster, the gravitational lensing should follow from its distribution.

On the contrary, the mass distribution reconstructed by the lensing effect is very different from the one derived by X-ray observations of the gas [49]. Fig. 3.3 shows the observations of the Bullet cluster. It is clear that the lensing mass and baryonic matter are separated, which implies the presence of DM (that has to be collisionless). The mass distribution of the Bullet cluster (and other similar colliding clusters) is difficult to explain with modified gravity.

3.2 Properties and Candidates of Dark Matter

We list below the main typical properties that a DM candidate should satisfy:

1. **Zero electric and color charge:** This indicates that DM does not interact directly with photons and does not lead to exotic isotopes;
2. **Long life time:** It should be at least as long as the age of the Universe, in order

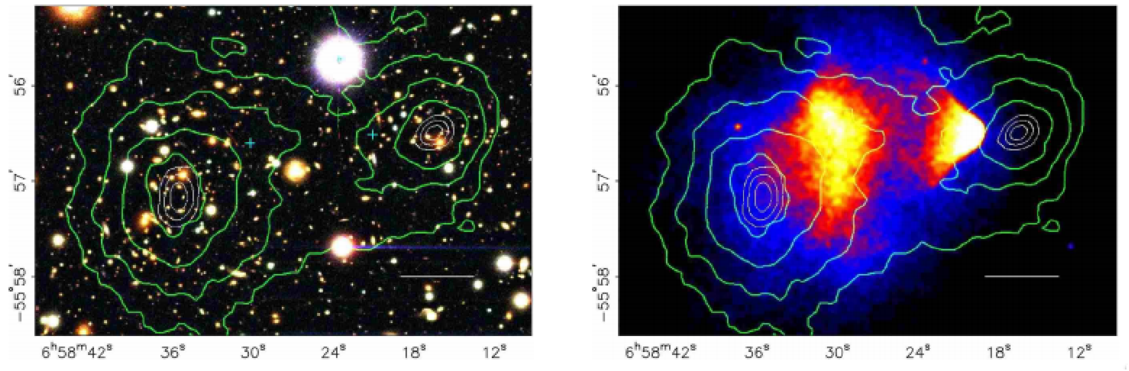

Figure 3.3: The image of the Bullet cluster. The green lines in the two images are contours of weak gravitational lensing, superimposed to observations in the optical band on the left and in X-rays on the right. The blue cross indicates the center of mass of the plasma gas, which significantly deviates from the center of mass determined through the weak gravitational lensing. The figure is taken from Ref. [49].

to be present today;

3. **Correct relic abundance:** It can be produced by thermal or non-thermal processes in the early universe, in all cases those processes need to determine the DM abundance observed today;

4. **Massive:** It constitutes the dominant mass component of the Universe.

5. **Cold or warm:** To be consistent with observations of LSS and N-body numerical simulation.

Because of above stringent characteristics, it is not possible to find a suitable DM candidate in the standard model of particle physics. Neutrinos looked to be good candidates, but they are not cold, i.e., they are relativistic at the beginning of structure formation. This implies a long free streaming path, that would lead to a structure growth inconsistent with observations described in section 2.3. N-body simulations has been crucial in understanding that hot DM candidates are not able to form the structures observed today [50].

Therefore, suitable DM candidates generally require new physics beyond the standard model [51, 52]. There are many possibilities proposed, including Weakly Interactive Massive Particle (WIMP), Axions, sterile neutrinos and others. We mainly focus on the WIMP model in this thesis. Here we sketch a few other types of candidates.

Sterile Neutrino: they are right-handed neutrinos added to the standard model to help explain the (small) mass of neutrinos. This component almost does not participate in electroweak interactions, and the mass is about keV providing warm DM. Sterile neutrinos may be generated by neutrino oscillations or by the decay of heavier particles [53]. It can decay due to mixing with ordinary neutrinos and releasing ordinary neutrinos plus photons through one-loop effects. The final state photons are monochromatic with energy corresponding to half mass of the sterile neutrinos [54]. The parameter space for mass and mixing angle can be constrained by searching for X-rays (i.e., keV photons) from galaxies and clusters [55–57].

Axion: The CP violation in strong interactions would lead to the existence of an electric dipole moment of neutrons, which is not found in high-precision measurement experiments. A way to solve the strong CP problem is to introduce a new dynamical particle, the axion. Two typical models are the DFSZ and KSVZ models [58].

They foresee an interaction between axion and two photons, and this makes the axion to possibly play an important role in star evolution and other astrophysical processes. The Primakov effect [59] can lead to a resonant production of photons from axion decay in regions with strong magnetic field. There are many experiments searching axions, including the CERN Axion Solar Telescope (CAST) [60], Cosmic Axion Research with Rydberg Atoms in resonant Cavities in Kyoto (CARRACK) [61], the Axion DM eXperiment (ADMX) [62], Polarisation of Vacuum with LAser (PVLAS) [63] and so on.

Besides the solution in terms of particles, there are some massive but compact astronomical objects, made of baryons, that can also be considered as candidates of DM.

MACHO: Massive Compact Halo Objects (MACHO) [64] is small size but massive baryonic matter, including very dark stars, or brown dwarfs. They do not emit electromagnetic waves, so they are hard to be detected, but can be searched for using gravitational lensing. However, limits from the BBN on the amount of baryons in the early Universe makes it unlikely that they can be a viable candidate for DM.

BH and PBH: Stellar black holes (BH) as candidates for DM have been already excluded from gravitational lensing data, and in general BH are constrained by the same BBN bounds mentioned for MACHOs. The way to avoid BBN constraints is to form BH before BBN. Such primordial black holes (PBH) would be a microscopic black hole formed by quantum fluctuations in the early universe and may be a candidate for DM [65, 66].

WIMP: Let us now focus on the candidate considered in this thesis, the WIMP. Among many candidates proposed in the literature, the WIMP is the most popular one [67]. Let us represent the DM and its antiparticle by χ and $\bar{\chi}$ (we will not discuss specific realizations of WIMP, like supersymmetric candidates, see more information in Refs. [68, page 709-764][69, 70]). If they are Majorana particles, the two of them are the same. The abundance of DM can be inferred from its thermal history during the evolution of the Universe. In the particle plasma of the early universe, DM particles and ordinary matter were in thermal equilibrium through efficient annihilation and production processes. According to Boltzmann equation, the evolution of the number density can be described by:

$$\dot{n}_\chi = -3\, H\, n_\chi - \langle \sigma_{\mathrm{ann}} v \rangle \left[n_\chi^2 - (n_\chi^{eq})^2 \right] . \tag{3.1}$$

where σ_{ann} is the annihilation cross section. It is clear that $\langle \sigma_{\mathrm{ann}} v \rangle$ becomes a major parameter in describing DM properties. For energies below the DM mass, the DM particles cannot be efficiently produced by the bath and the density decreases as $n_\chi^{eq} = g(\frac{m_\chi T}{2\pi})^{3/2} e^{-m_\chi/T}$, if DM is in thermal equilibrium.

To describe the decoupling we rewrite the Boltzmann equation in terms of

$$\frac{\mathrm{d}Y}{\mathrm{d}t} = -\langle \sigma_{\mathrm{ann}} v \rangle s (Y^2 - Y_{eq}^2), \tag{3.2}$$

where $Y \equiv n_\chi / s$ and s is the entropy density. Hot DM refers to the case where DM particles decouple from the bath when they are still relativistic. In this case, we have

$$n_\chi(T) = g_{\chi *} \frac{\zeta(3)}{\pi^2} T^3, \tag{3.3}$$

$$s(T) = g_{s*} \frac{2\pi^2}{45} T^3, \tag{3.4}$$

where $\zeta(3)$ shows the Riemann ζ function, $\zeta(3) = 1.20206$.

For Boson, there is $g_{\chi *} = g_\chi$ and Fermion $g_{\chi *} = 3 g_\chi / 4$. g_χ is spin degree of freedom of particle χ and g_s is the entropy degree of freedom when temperature is T. After decoupling, the comoving density is frozen, and today number density can be expressed as

$$n_{\chi 0} = s_0 Y_\infty = s_0 Y_{eq}(x_f) = s_0 \frac{45\zeta(3)}{2\pi^4} \frac{g_{\chi *}}{g_s * (T_f)}, \tag{3.5}$$

where index f is the time of freeze-out, here $x_f \equiv m_\chi / T$ and $x_f \lesssim 2$ [71].

Non-relativistic DM decoupling means that DM cools down before freezing out. The decoupling roughly occurs when the annihilation rate becomes comparable to the expansion of the Universe. The solution to the Boltzmann equation leads to the relic abundance:

$$\begin{aligned} \Omega_\chi h^2 = m_\chi n_{\chi 0} \frac{h^2}{\rho_c} &= \frac{m_\chi s_0 Y_\chi (x \to \infty)}{\rho_c} \\ \sqrt{\frac{4\pi^3}{45}} \frac{g_*^{1/2}}{M_P} &\frac{x_f}{\langle \sigma_{\text{ann}} v \rangle} \frac{T_0^3 h^2}{\rho_c} (\frac{a_1 T_1}{a_0 T_0})^3 \\ &= 0.847 (\frac{x_f}{10}) (\frac{g_*}{100})^{1/2} \frac{10^{-27} \text{cm}^3 \text{s}^{-1}}{\langle \sigma_{\text{ann}} v \rangle}. \end{aligned} \tag{3.6}$$

Considering CMB observations that implies $\Omega_\chi h^2 = 0.1200 \pm 0.0012$, one finds

$$\langle \sigma_{\text{ann}} v \rangle \simeq 3 \times 10^{-26} \text{cm}^3 \text{s}^{-1}. \tag{3.7}$$

The value of the cross section just derived coincides to expectations for particles annihilating through weak interactions. Since the solution of problems in the standard model of particle physics typically requires an extension at the electro-weak scale, WIMP candidates “naturally” arise. This coincidence is sometime called the “WIMP miracle”. Several realizations have been proposed in the literature, as, for example, neutralino and neutrino in Supersymmetric models [72] and Kaluza-Klein particles in Extra-Dimension theories [73].

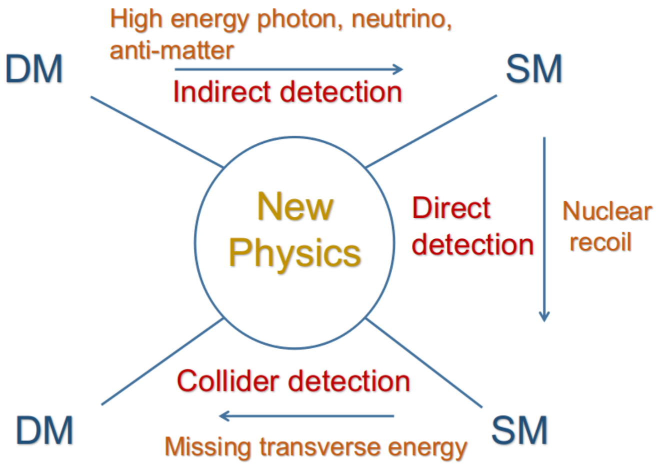

Figure 3.4: A schematic diagram of the three methods (Collider, Direct and indirect) and their relationship for DM detection.

3.3 Detection of DM

Particle DM detection can follow three routes: collider, direct and indirect detection. The three probes are complementary to each other. Fig. 3.4 is a schematic diagram of such three ways to detect DM: at colliders one looks for missing energy in the final state from the collision of standard model particles (since DM produced in those collisions would escape detectors); the direct detection aims at capturing the signal of DM bumping to targets of standard model particles; indirect detection look for standard model particles produced via DM annihilation or decay in astrophysical environments.

3.3.1 Collider Detection

If DM was produced in the high-temperature environment of the early universe, it should also be produced by particle collisions at the Large Hadron Collider (LHC), unless its mass is well above the TeV scale or it only interacts with leptons. The minimal condition to produce a pair of DM particles is that the energy of the colliding particles exceeds twice the DM mass. Signatures of such events are related to the standard model particles produced along with DM particles or in the missing energy associated to DM particles escaping the detector.

The DM detection is however not straightforward due to the presence of several background components. For example, also neutrinos carry energy out from the detector. No signal of WIMP has been found at LHC at the time of writing. For more details, see e.g., Ref. [74].

3.3.2 Direct Detection

Direct detection refers to the search for nuclear (or electron) recoil [75] due to DM scattering in experiments based on underground detectors. In simple words, the idea is to set up a detection target of ordinary particles, then if there are enough DM particles passing through the Earth, they will hit the targets, scattering with its particles, and possibly give a trigger signal. However, the interaction is so weak that one needs very massive targets and extremely good background shielding. Direct detection experiments are arranged as deep as possible under the ground to eliminate background pollution, and they use sophisticated techniques to filter out other backgrounds such as the signal caused by radioactive elements in underground rocks.

Nuclear recoils occur at a measurable energy (typically keV) if the WIMP is in the range of mass GeV to TeV. For more details, see e.g., Refs. [76–85]

3.3.3 Indirect Detection

If we assume that DM particles have the possibility to annihilate, as in the case of WIMP, or decay, then they can inject standard model particles. The detection of the latter ones in astrophysical structures might be used to indirectly infer the presence of DM. The relevant DM properties for this process to occur are the annihilation rate (or decay lifetime), DM mass and final states of annihilation (decay). Possible DM signatures are searched in fluxes of neutrinos, photons, electrons and positrons, antiprotons, and antideuterium.

In this thesis, we will focus on signatures coming from γ-rays. The production of γ-rays from WIMP can follow different mechanisms [86]. The so-called *prompt emission* is typically the result of the decay of π^0 (produced as a consequence of hadronization of particles injected by the annihilation) producing a continuum spectrum, direct production from second order processes giving rise to a spectral line (whose detection would provide a smoking-gun for WIMP), or final state radiation, typically resulting in a continuum spectrum but with specific spectral features. Radiative γ-ray emission comes from the *Bremsstrahlung* or the *Inverse Compton mechanism* (IC) of the electron and positrons produced by DM annihilation. IC occurs when an electron/positron scatters with a CMB or interstellar photon, transferring momentum to it which reaches γ-ray energies.

At present, many experiments are implementing indirect DM searches through γ rays. They include *Fermi*-LAT, High Energy Stereoscopic System (HESS) [87], Very Energetic Radiation Imaging Telescope Array System (VERITAS) [88], Major Atmospheric Gamma Imaging Cherenkov telescope (MAGIC) [89], ARGO-YBJ [90, 91], Large High Altitude Air Shower Observatory (LHAASO) [92], eta. For more details on indirect detection experiments, see Refs. [93, 94]

In the rest of the thesis we will focus on the *Fermi*-LAT telescope, which is extensively described in chapter 4.

CHAPTER 4

Acquisition and Processing of Astronomical Data

This chapter describes the data I used in the thesis. The first and second sections concern the *Fermi* large-area telescope (LAT). They introduce its design and main properties, the instrument response functions, the data processing, and the catalogs of resolved astrophysical sources derived by the *Fermi*-LAT collaboration. The following sections describe the acquisition and processing of astronomical observations from other telescopes.

4.1 Overview of the *Fermi*-LAT Telescope

Among the various bands of the electromagnetic spectrum, the radiation with the highest energy is provided by γ rays. This thesis will be based on observational results coming from such a band. The *Fermi* γ-ray space telescope represents the state-of-the-art in terms of collecting area, angular resolution and field of view, for what concerns γ-ray detectors below TeV energies. Launched on June 11, 2008, into low Earth orbit, *Fermi* Telescope began its full-sky γ-ray monitoring on August 4, 2008. The energy range of detected photons is between $8\,\mathrm{keV}$ to $1\,\mathrm{TeV}$, receiving an intensity thousands to hundreds billion times higher than the naked eye can accept. It takes 96 minutes to orbit the Earth, has a field of view of about 20% of the sky, taking only three hours to complete the image of the whole sky [95, 96]. It consists of two detection systems, one is the *Fermi* Large Area Telescope (*Fermi*-LAT); the other is the *Fermi* Gamma-ray Burst Monitor (*Fermi*-GBM) [97].

We do not focus on transient but rather on stationary γ-ray emission and consider only data from the *Fermi*-LAT detector. The instrument tracks electron pairs which are converted from γ-ray photons. The major parts of the instrument include 16 accurate trackers (TKR) and Calorimeters (CAL). They combine together with data acquisition modules to become 16 towers, assembled in a 4×4 mechanical support structure, with an anti-coincidence detector (ACD) which is wrapped in a micrometeoroid shield. Events trigger electronics channel readout under each tower and anticoincidence [98]. The latter is very important for efficient rejection of the charged particle background, which is thousands of times more intense than the celestial gamma-ray radiation. The *Fermi*-LAT has been calibrating all aspects of the data analysis on-orbit results [99].

Thanks to this technology, the *Fermi*-LAT can measure with good precision the direction and energy of photons, so that we can trace back the flux and location of γ ray sources.

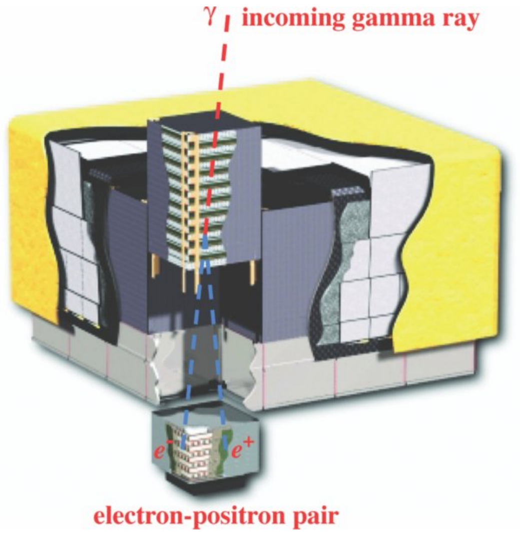

Figure 4.1: Fermi-LAT schematic diagram, the photons pass through instruments, the track detectors trace the direction of the propagation path, then the Calorimeters obtain energy, and the information is brought to the bottom structure. Telescope size is $1.8\ \mathrm{m} \times 1.8\ \mathrm{m} \times 0.72\ \mathrm{m}$, weights 2,789 kg. The figure is taken from Ref. [98].

The *Fermi*-LAT performance depends on the instrument hardware design, but also on the algorithm of event reconstruction, background rejection and the quality of event selection.

For the estimates of telescope capabilities, the LAT collaboration has been using Monte Carlo simulations of the interaction between γ-rays and the instruments. These simulations have been refined over the years thanks to observations and better calibrations. The level of reconstruction is indicated by a number after the name "Pass", and we will use Pass8[1] data in this thesis. There are a certain level of background contamination and a particular set of the *Instrument Response Functions* (IRFs) are corresponding to each data release. The IRFs are factored into efficiency of the effective area of detec-

---

[1] https://fermi.gsfc.nasa.gov/ssc/data/analysis/documentation/Pass8_usage.html

tor, resolution as given by the point-spread function (PSF), and energy dispersion. The analysis of Pass8 uses the most recent algorithm for event reconstruction, improving the performance of the instrument and reducing the stacking effect.

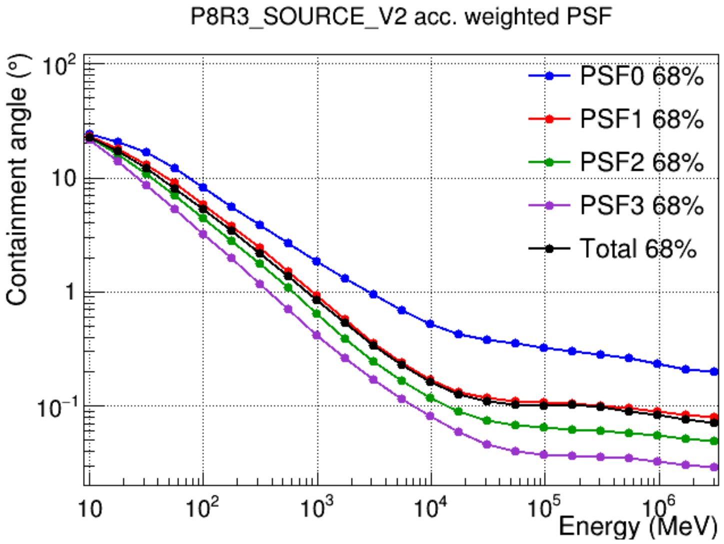

Figure 4.2: 68% containment angle of the *Fermi*-LAT as a function of energy. The black line is the average for all data. From PSF0 to PSF3 one can see how the quality goes from poor to high. The figure is taken from Ref. [100].

Events can be classified as TRANSIENT, SOURCE, CLEAN, ULTRACLEAN and ULTRACLEANVETO, depending on the level of background rejection. The first class is chosen for γ-ray burst analysis and has a poor “quality” since the rejection is performed using temporal features. The data quality of the latter four options is higher. SOURCE is the one with the largest effective area but still with non-negligible contamination; ULTRACLEANVETO loses a significant fraction of effective area in order to guarantee high quality of the reconstructed signal and to exclude pollution from cosmic rays; CLEAN and ULTRACLEAN are cases in between. The works described in this thesis adopt UL-

TRACLEANVETO Pass8.

In the process of analyzing γ-ray sources, we need also to carefully consider the angular resolution of the telescope. In this respect, events are divided into four categories [101], depending on the quality of the reconstruction of the direction. PSF3 is the selection with the highest angular resolution, while PSF0 is the one with the poorest.

In Fig. 4.2, we show the angular resolution, which improves as the energy increases. At $100\,\mathrm{MeV}$, the containment angle is equal to $5°$, while it is $0.2°$ at $10\,\mathrm{GeV}$.

The *Fermi*-LAT collaboration with the *Fermi* Science Support Center (FSSC) developed a set of scientific analyses tools (`ScienceTools`), in order to support the community in the astronomical analyses [102]. They will be employed in all the analysis shown later on.

Recently, the *Fermi*-LAT collaboration has released the Fourth *Fermi* Large Area Telescope catalog, (4FGL) [103], which is based on the first eight years of scientific data. It contains 5,064 sources, detected at 4σ confidence, in the $50\,\mathrm{MeV}$ to $1\,\mathrm{TeV}$ energy range. More than 3,130 of them are identified as Blazar-like AGN, 239 are Pulsars, see Fig. 4.3.

Furthermore, recently the *Fermi*-LAT collaboration has also released the Third Catalog of High-Energy *Fermi*-LAT Sources (3FHL) [104], which contains 1,556 astrophysical objects in the energy range $10\,\mathrm{GeV} \sim 2\,\mathrm{TeV}$. The vast majority of those sources are BL Lacs. The difference between this catalog and the 4GFL one is that the 3FHL focuses on the detection of sources in the high energy bins. Both the 4FGL and 3FHL improves over previous catalogs built by the *Fermi*-LAT collaboration with fewer years of data collection and less efficient data selection. In the analyses presented in this thesis, the sources of 4FGL and 3FHL catalogs are considered as foreground, and masked from the

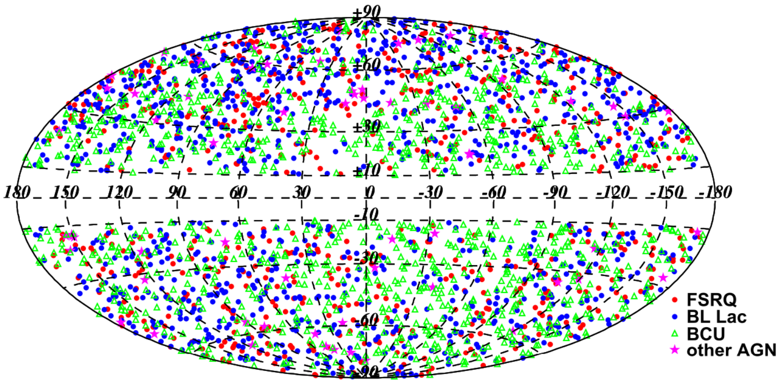

Figure 4.3: The astrophysical sources distribution of 4FGL in the galactic ordinate 4FGL. The figure is taken from Ref. [103].

γ-ray intensity maps.

4.2 Acquisition of *Fermi*-LAT maps

In the following, we report a brief description of how the γ ray counts and flux maps have been obtained from the released data.

Download Data: Download of weekly photon files provided by the *Fermi*-LAT collaboration at *Fermi* official website[2]. As mentioned before, since the researches in this thesis concern the correlation of γ-ray signals with LSS, namely, they deal with the unresolved/diffuse γ-ray emission, we choose ULTRACLEANVETO events. The description of the weekly photon file can be found in the Extended files and the spacecraft parameters in the Spacecraft files.

Combine Data: Once a complete set of weekly data and long mission spacecraft

---

[2] https://heasarc.gsfc.nasa.gov/FTP/fermi/data/lat/

files is collected, the next step is to integrate all the weekly files into one data file. This is done using the command `gtselect` which reads all the relevant parameters involved and ensures consistency.

Remove photons: Filtering the data to retain the appropriate photon events and to remove the Earth Limb contamination is necessary. The latter is addressed by limiting the zenith angle to less than 90°. In the rest of the thesis, we will use PSF1+2+3 above $1\,\mathrm{GeV}$, and PSF3 at lower energies, where the statistics are high but the PSF becomes poorer. The exposure has to be adjusted in agreement with the filtered events. The tool `gtmktime` is adopted to derive the Good Time Intervals (GTI).

Binning Data: Data are binned in energy, applying the tool `gtbin`. At this stage, we define very small bins. This is because, later on, to compute fluxes, we need to perform integrals in energy and they can be thus approximated as a simple sum given the small size of the bins.

Exposure map: The cumulative exposure (area$\times$time) of any given point in the sky is based on the *Fermi*-LAT IRFs[3], determined through Monte Carlo simulations by the *Fermi*-LAT collaboration, as mentioned above. The calculation of exposure sky map is performed through the command `gtcube`.

Flux map: Once count and exposure sky maps are obtained, the photon flux map is derived by dividing the count maps by the exposure maps and the pixel area $\Omega_{\rm pix} = 4\pi/N_{\rm pix}$.

Subtract contamination: Download the latest official foreground model provided by the *Fermi*-LAT collaboration in the `Healpix` format, and interpolate it to obtain the

---

[3] https://fermi.gsfc.nasa.gov/ssc/data/analysis/documentation/Cicerone/Cicerone_LAT_IRFs/index.html

corresponding maps in the same energy bins of the photon flux maps. Then subtract the foreground sky map from the photon flux map. We also further mask latitudes below 30° to avoid residuals from the Galactic plane.

The outlined procedure is conducted using the *Fermi*-LAT `ScienceTools`, with the current version being `v10r0p5`[4], and taking the events `P8R2_ULTRACLEANVETO_V6`.

We considered 108 months of data, from week 9 to week 476, a `Healpix` pixelation with the resolution parameter $N_{\text{side}} = 1024$ which corresponds to a total number of pixels $N_{\text{pix}} = 12,582,912$ and a mean spacing of $\sim 0.06^\circ$, similar to the best angular resolution of the γ-ray data. Fig. 4.4 illustrates the γ-ray flux sky map above $1\,\text{GeV}$.

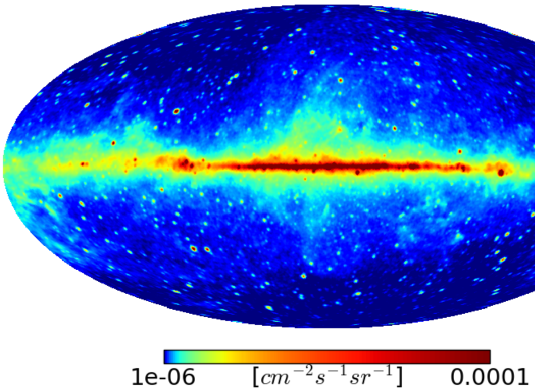

Figure 4.4: The *Fermi* γ-ray flux sky map for photon energies above $1\,\text{GeV}$ in Mollview projection. The figure is taken from Ref. [105].

We first determined the flux sky maps in 100 micro-bins of energy from $100\,\text{MeV}$ to $1\,\text{TeV}$, evenly spaced in logarithmic scale. Then we re-binned them into 9 larger energy bins, from $631\,\text{MeV}$ to $1\,\text{TeV}$, as reported in Tab. 4.1.

---

[4] https://fermi.gsfc.nasa.gov/ssc/data/analysis/software/

Table 4.1: The energy bins used in our works. For each bin we list upper and lower energy limits $E_{\rm min}$ and $E_{\rm max}$, the minimum $\ell_{\rm min}$ and and maximum $\ell_{\rm max}$ multipoles in calculation of power spectrum, see section 5, and, in the last column $\theta_{\rm cont}$, the size of the 68% containment angle.

Bin	$E_{\rm min}$ [GeV]	$E_{\rm max}$ [GeV]	$\ell_{\rm min}$	$\ell_{\rm max}$	$\theta_{\rm cont}$(deg)
1	0.631	1.202	40	251	0.50
2	1.202	2.290	40	316	0.58
3	2.290	4.786	40	501	0.36
4	4.786	9.120	40	794	0.22
5	9.120	17.38	40	1000	0.15
6	17.38	36.31	40	1000	0.12
7	36.31	69.18	40	1000	0.11
8	69.18	131.8	40	1000	0.10
9	131.8	1000	40	1000	0.10

The *Fermi*-LAT data used in our works involve the Unresolved γ-ray Background (UGRB), i.e., we mask bright astrophysical sources (listed in the *Fermi*-LAT catalogs): as mentioned before, we masked the $|b| < 30^\circ$ galactic plane (but in chapter 7 we also discuss the influence of different possibilities), we excluded resolved astrophysical sources in the 4FGL and 3HFL catalogs, and subtract the foreground maps. Note that in chapter 6, we adopted a preliminary version of the 4FGL, called FL8Y catalog[5], since 4FGL was not released at the time of that computation (we then tested that differences in the final results obtained masking with the FL8Y or 4FGL catalog are negligible).

The mask of each source is constructed according to the angular resolution of the specific energy bin and the brightness of the source. For point sources, the masking

---

[5] https://fermi.gsfc.nasa.gov/ssc/data/access/lat/fl8y/

radius around each source is defined as

$$F^{\gamma}_{\Delta E} \exp\left(-\frac{R^2}{2\theta^2_{\Delta E}}\right) > \frac{F^{\gamma}_{\Delta E,\text{faintest}}}{5}, \tag{4.1}$$

where $F^{\gamma}_{\Delta E}$ is the integral photon flux of the source in the energy bin ΔE, and $F^{\gamma}_{\Delta E,\text{faintest}}$ is the flux of the weakest source in the same energy bin. $\theta_{\Delta E}$ is the 68% containment angle, already mentioned.

The resulting energy-dependent masks aim at properly covering resolved sources and avoiding artefacts due to source flux leakage outside the mask, but at the same time maintaining a good sky coverage, accounting also for the energy dependence of the PSF.

Fig. 4.5 shows the sky maps of the γ-ray flux before and after subtracting the foreground mask. The foreground is removed using the model `gll_iem_v06.fits`[6].

4.3 Other Astronomical Data

This section describes the other astronomical datasets used in our works, and explain how to obtain the specific maps used for our computation.

4.3.1 Planck maps

The CMB map we adopted for the computations in chapter 7 comes from Planck 2018 full-mission data release ("PR3"), that is accessible on the website Planck Legacy Archive[7]. There are four algorithms to do the component separation in maps: COMAN-

---

[6] https://fermi.gsfc.nasa.gov/ssc/data/access/lat/BackgroundModels.html

[7] http://pla.esac.esa.int/pla

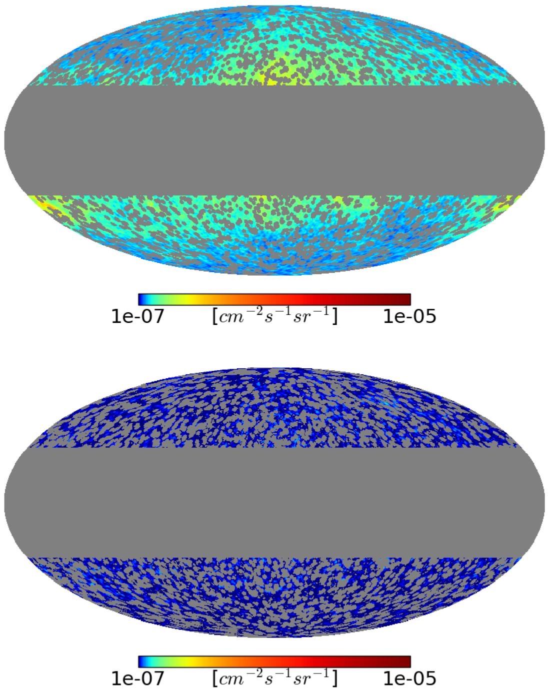

Figure 4.5: Masked γ-ray flux sky map with a latitude cut of 30° around the galactic plane and circles for resolved point sources mask, in the energy bin $1.202\,\text{GeV} \sim 2.290\,\text{GeV}$: the upper is before foreground subtraction, and the bottom is after subtraction, both of them are in Mollview projection.

DER, SEVEM, SMICA and NILC. We use SMICA synthesized CMB map, which stems from spectral matching technology [106]. We only need the `Healpix` maps with relatively low resolution, such as $N_{\text{side}} = 64$ or 128, since the main contribution of the ISW signal comes from large-scales. We eventually upgraded the CMB map to $N_{\text{side}} = 1024$ just to use the same resolution as in the *Fermi*-LAT maps and to avoid possible systematic errors. In Fig. 4.6, we have CMB isotropic sky map on the upper panel and underside we show the mask map of the Planck team defined to exclude foreground and astrophysical sources, and leaving coverage of 83.8% of the sky.

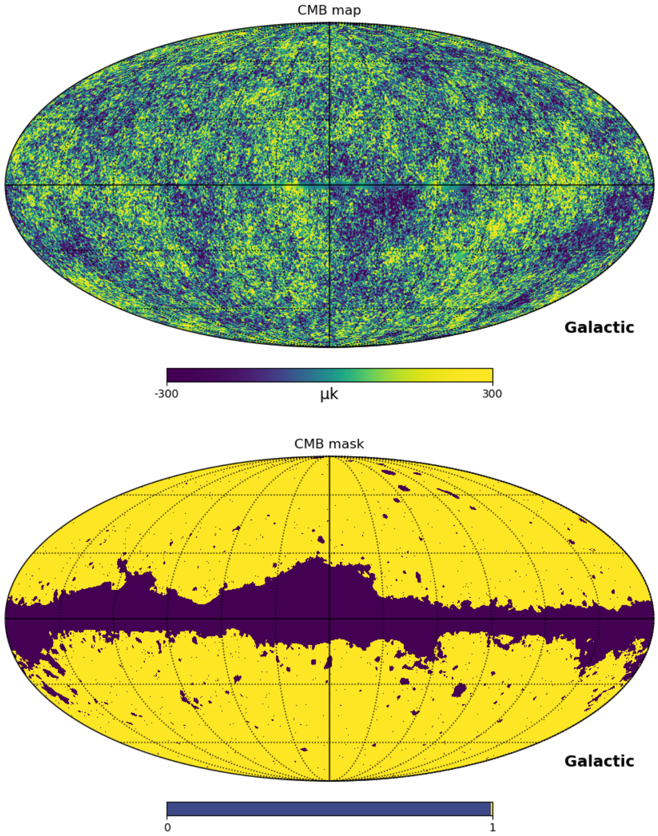

Figure 4.6: The Planck CMB temperature anisotropy map with unit μK and its mask map in Mollview projection.

4.3.2 Catalogs of galaxy Clusters

The analysis of chapter 6 is based on four galaxy cluster catalogs that were obtained in different frequency bands: one in the optical (SDSSDR9), one in the infrared (WHY18) and two in the X-ray band (MCXCsub and HIFLUGCS). The main feature is that they contain a large number of galaxy clusters with low redshifts and large masses, namely, suitable to produce a relevant cross-correlation signal according to theoretical expecta-

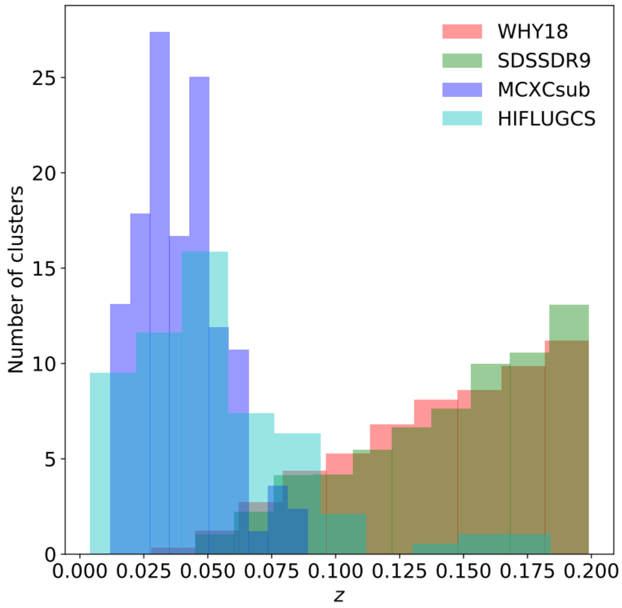

Figure 4.7: The redshift distribution to the number of four galaxy cluster catalogs: WHY18, SDSSDR9, MCXCsub AND HIFLUGCS in our works.

tions.

The properties of the galaxy cluster catalogs are listed below:

1. WHY18 is taken from the combination of photometric galaxies from 2MASS, the Wide-field Infrared Survey Explorer (WISE) [107] and the SuperCOSMOS Sky Survey [108]. The selection applied to the sources is such to include clusters with $M_{500} > 3 \times 10^{14} M_{\odot}$ and redshift between 0.025 and 0.3. The final number of selected clusters is 47,500 [109];

2. SDSSDR9 is part of the full SDSS catalog, acquired using an Adoptive Matched Filter (AMF) [110] technique, which is built using the cluster density radial profile, the galaxy luminosity function and the redshift. Applying this filter, there are

49,479 clusters with redshift between 0.046 and 0.691 [111] that are retained;

3. MCXC is an X-ray catalog [112], containing 1,743 clusters from two types of X-ray observations: contiguous area survey ROSAT [113] and deeper pointer X-ray observations. MCXCsub is built from MCXC selecting $M_{500} > 10^{13} M_{\odot}$, angular diameter larger than $0.2°$, latitude larger than $20°$ and positions in the sky such to avoid contamination from bright γ-ray point-sources [114];
4. There are 63 clusters in the HIFLUGCS catalog with latitude larger than $20°$. They have a flux between 0.1 to 2.4 keV larger than $2 \times 10^{-11} \mathrm{ergs\ s^{-1}\ cm^{-2}}$ [115].

Because the goal is to study the diffuse γ-ray emission of galaxy clusters, and therefore they have to be larger than *Fermi*-LAT PSF (in order to be distinguished from point-sources), we only considered clusters with $M_{500} > 10^{13} M_{\odot}$ mass and redshift less than 0.2. This will be better discussed in the following chapters. In addition, in order to make the identification of a galaxy cluster robust, we restricted the WHY18 catalog by keeping only clusters with the richness greater than 5. Tab. 4.2 lists the number of selected galaxy clusters in each catalog. Not all the catalogs provided the mass in terms of M_{500}, and we performed the appropriate conversions using the formalism reported in the Appendix of Ref. [116]. Fig. 4.7 shows the redshift distribution of the final catalogs we used.

The catalog sky maps were also masked in the correlations analysis, to prevent contamination from galactic plane or other sources, and systematic errors. For the WHY18 infrared catalog, we use the mask from Ref. [117]; it simply coincides with the area that was not covered by the SDSS survey for the optical catalog SDSSDR9; and we define the

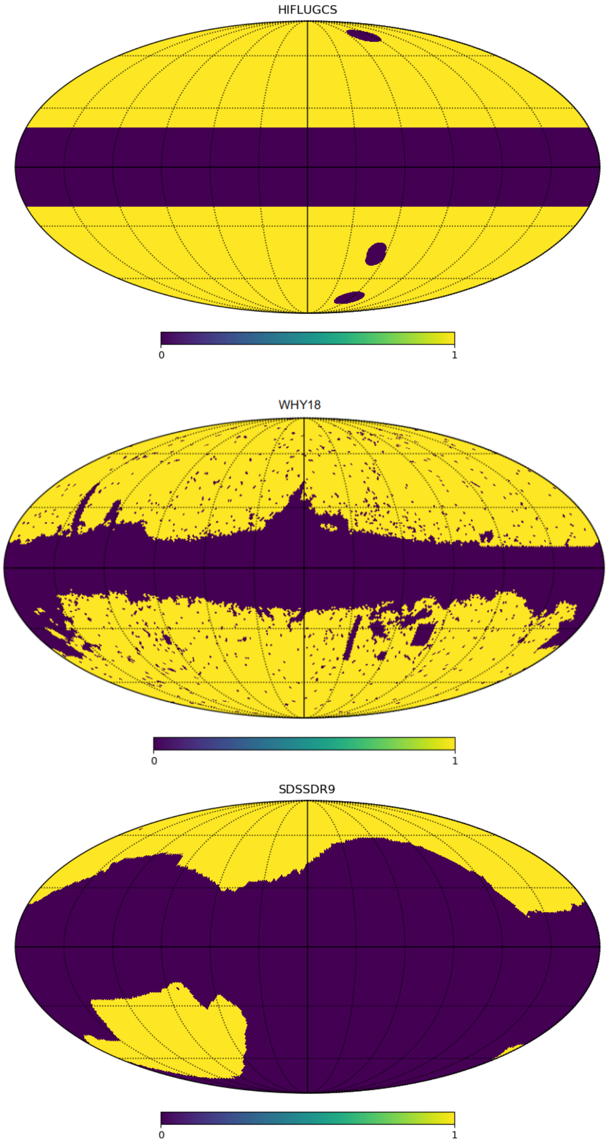

Figure 4.8: The mask maps of the four galaxy cluster catalogs used in our work. From top to bottom are HIFLUGCS (same with MCXCsub), WHY18 and SDSSDR9, respectively.

Table 4.2: The list of galaxy cluster catalogs used in this thesis. For each catalog, we give the total number obtained after the selection discussed in the text.

Catalogue	Type	Reference	Total number
WHY18	infrared	[109]	8,999
SDSSDR9	optical	[111]	2,582
MCXCsub	X-ray	[114]	109
HIFLUGCS	X-ray	[115]	105

same mask for X-ray catalog MCXCsub and HIFLUGCS by removing the galactic plane for $|b| > 20^\circ$ and the Virgo cluster [118].

For all catalogs, we assume uniform coverage, at least on the angular scales (that is, at relatively small angles) that are explored in our analysis of cross-correlation. Fig. 4.8 shows the mask maps of the cluster catalogs.

CHAPTER 5

Cosmological Statistical Analysis Methods

In order to dig out the information buried in the huge quantity and high quality of cosmological data, that we have at disposal in the era of precision cosmology, appropriate statistical tools are needed. Bayesian Analysis is one of the most extensively adopted statistical methods for cosmological studies. The following section describes the basics of Bayesian theory, the likelihood function, and Markov chain Monte Carlo methods used in our cross-correlation studies.

5.1 Bayesian Analysis

We make use of the parameter inference based on the Bayesian theory [119]. In this section I briefly review the basics of the theory, starting from the *Bayes theorem*.

First of all, the expression of the theorem can be derived from probabilistic axioms, not relying on Bayes interpretation. In particular, the theorem comes from the definition of the joint probability as the product of conditional and marginal probability, i.e.:

$$P(A \cap B) = P(A|B)P(B). \tag{5.1}$$

This means that the probability of events A and B to happen simultaneously is equal to the probability of event A under the condition of B already happened times the marginal probability of B. Following a similar logic, we can derive $P(B \cap A)$ and using obvious commutative law $P(A \cap B) = P(B \cap A)$ derive:

$$P(B \cap A) = P(B|A)P(A) = P(A|B)P(B) \ , \tag{5.2}$$

which means

$$P(A|B) = \frac{P(B|A)P(A)}{P(B)} \ , \tag{5.3}$$

that is called the Bayes theorem.

This equation encapsulates the technical core of many statistical analyses in cosmology. The Bayesian approach is often preferred to the frequentist one since we cannot repeat experiments, there is only one universe and we observe it from a single position.

In the context of parameter inference, the Bayesian theorem reads:

$$P(\vec{\theta}|\mathbb{D}) = \frac{P(\mathbb{D}|\vec{\theta})P(\vec{\theta})}{P(\mathbb{D})} \ , \tag{5.4}$$

where $\vec{\theta}$ is a series of parameters of a model, and the observed data points is represented by $\mathbb{D}$.

- $P(\vec{\theta}|\mathbb{D})$ is the *posterior* probability of the series of parameters of the model, and expresses our updated belief after performing observations. It can be used to derive expected values and credible intervals for the parameters.

- $P(\mathbb{D}|\vec{\theta})$ is known as the *likelihood function* (used for parameter inference in the frequentist approach) and expresses how likely are the parameters given the data.
- $P(\vec{\theta})$ is the prior probability of the parameters of the model. It refers to our first prediction or our original knowledge about the parameters, such as, e.g., some negative or positive bounds on some parameters. Prior distribution sometimes is considered to involve subjective assertions, but nevertheless, it is adjusted by the observational outcomes in the computation of the posterior. When a priori information is unknown, a uniform distribution is often adopted and typically would not affect the final results.
- $P(\mathbb{D})$ shows the Bayesian evidence, which is a normalization constant in parameter inference, whilst becomes crucial in case of model comparison.

The prior and posterior distributions are functions that are exclusive of the Bayesian analysis, in a process of using data to update and correct prior distribution information to get the posterior. Statistical inference concerns funding the cosmological parameters which are most consistent with the observed data. In order to do that, one has to define the likelihood function.

5.2 Likelihood Function in Cosmology

As mentioned above, the likelihood is the function that evaluates how likely are the model parameters once observational data are taken. It is generally expressed by

$$\mathcal{L}(\vec{\theta}) = P(\mathbb{D}|\vec{\theta}). \tag{5.5}$$

If a data set is following the Gaussian distribution, then the Likelihood is

$$\mathcal{L} = \frac{1}{(2\pi)^{n/2}|\det\Gamma|^{1/2}} \exp\left[-\frac{1}{2}\sum_{ij}(\mathbb{D}-\mathbb{T})_i \Gamma^{-1}_{ij}(\mathbb{D}-\mathbb{T})_j\right], \tag{5.6}$$

where Γ_{ij} is covariance matrix, and $\mathbb{T} = f(\vec{\theta})$ denotes the theory model. It is not difficult to see that the Gaussian likelihood function is intimately related to the statistical χ^2 through $\mathcal{L} \approx \exp\left[-\frac{1}{2}\chi^2\right]$, and the minimum of the χ^2 corresponds to the maximum of the likelihood.

There are several possibilities for the form of the likelihood: in most of the thesis we will consider a Gaussian likelihood (as suggested by LSS), with Poisson distribution in the cases involving photons counts.

In order to obtain a posterior distribution, which is the key function in Bayesian inference we need to multiply the likelihood by the prior. For the latter, in our works, we use flat or Gaussian priors. The posterior is computed using Markov Chain Monte Carlo (MCMC) algorithms.

5.3 Markov Chain Monte Carlo algorithm

To get the posterior distribution, we need to evaluate the likelihood by exploring the parameter space. This can be computationally intensive and the MCMC approach is the method that is widely used in Bayesian analyses to face this issue. It consists of sampling the posterior distribution such that the density of points becomes proportional to the distribution itself. Thanks to this algorithm, even very high-dimensional parameter spaces with non-trivial likelihoods can be analyzed.

A Markov chain is a sequence of random variables and describes a random process of transition from one state to another. The probability of a certain state only depends on its previous step, and, assuming to be in a stationary case, we have the so-called homogeneous chains identified by the transition probability $K(x, y)$ between two states x and y.

$$K(x, y) = P(X_{n+1} = y|X_n = x). \tag{5.7}$$

A probability distribution is said to be invariant with respect to the Markov chain if it fulfills the condition

$$\pi(y) = \int \mathrm{d}x \pi(x) K(x, y). \tag{5.8}$$

If a chain is reversible, i.e., satisfies the condition of detailed balance:

$$\pi(x)K(x, y) = \pi(y)K(y, x), \tag{5.9}$$

it has an invariant distribution.

Now we introduced a simple algorithm to build a Markov chain such to have the posterior as invariant distribution. The name “Monte Carlo” stays for the fact that one generates random sampling.

Let us choose a (in principle arbitrary) transition probability and define the acceptance probability as

$$\alpha(x, y) = \min \left\{ \frac{\pi(y)K(y, x)}{\pi(x)K(x, y)}, 1 \right\}. \tag{5.10}$$

In other words, when the chain is at point x, $K(x, y)$ is used to propose the point y, with a probability of accepting this transition given by $\alpha(x, y)$. One can show that the above acceptance makes the full transition probability to be $\alpha(x, y)K(x, y)$ and to satisfy the detailed balance. Thus the chain can be used to reconstruct π, than in the Bayesian context is the posterior distribution. This algorithm is famously known as Metropolis–Hastings algorithm [120].

In the literature, numerous different MCMC implementations have been proposed, on top of the Metropolis Hastings introduced above, including Gibbs sampling, independent sampling, random walk sampling and so on.

These methods have become crucial in astronomy and cosmology to confront theory with observations and to estimate cosmological parameters. Various sophisticated software packages or toolkits are available, like `CosmoMC` [121], `CosmoHammer` [122], `emcee` [123], `PMC` [124], `PyMC3` [125], `MontePython` [126], `CosmoSIS` [127].

In our works, I have used `CosmoMC`, `emcee` and `MontePython`. For a detailed introduction to these MCMC implementation see Refs. [121], [123] and [126].

5.4 Correlation Function Analysis

The n-points correlation functions are a widespread used tool for quantifying and ascertaining the relation among events or objects. In this section, first I derive the formalism of correlation functions, then introduce its application to LSS, in particular considering the Fourier power spectrum, which is the main object used in the following chapters.

5.4.1 General Description

Let us imagine an infinite grid in space, filled by particles, and consider one infinitely small cube with differential volume $\mathrm{d}V$. $\rho_0 \mathrm{d}V$ would represent the average number of particles, where ρ_0 is the average density. In this space, two objects (with the subscript of 1 and 2) with distance r_{12} gang together as a pair. The probability of finding a pair in which $\mathrm{d}V_1$ is occupied by an object 1 and $\mathrm{d}V_2$ by an object 2 is

$$\mathrm{d}P_{12} = \rho_1\, \rho_2 \mathrm{d}V_1 \mathrm{d}V_2 (1 + \xi(r_{12})), \tag{5.11}$$

where $\xi(r_{12})$ is the so-called *two-point cross correlation function* (2P CCF) between these two objects,

$$\xi(r_{12}) = \frac{\mathrm{d}P_{12}}{\rho_1\, \rho_2\, \mathrm{d}V_1 \mathrm{d}V_2} - 1 = \langle \delta_1(r_1) \delta_2(r_2) \rangle \ , \tag{5.12}$$

see Fig. 5.1 for an illustrative sketch.

If the objects are randomly distributed in space, then the joint probability is equal to the product of the two probabilities, thus the correlation is 0. However, if the distributions of two points cannot be regarded as independent distributions, then ξ is non-zero. The concept of 2P CCF is often used to judge whether two classes of objects have physical causal relationship. It is the most widely used tool to quantify the degree of clustering in a galaxy sample [128, 129]. Generally, it can be defined to determine the correlations between overdensities or underdensities, like already shown in equation 5.12. The overdensity δ is introduced in section 2.3 as $\delta(\boldsymbol{r}) = \rho(\boldsymbol{r})/\rho_0 - 1$ with ρ_0 is the background average density.

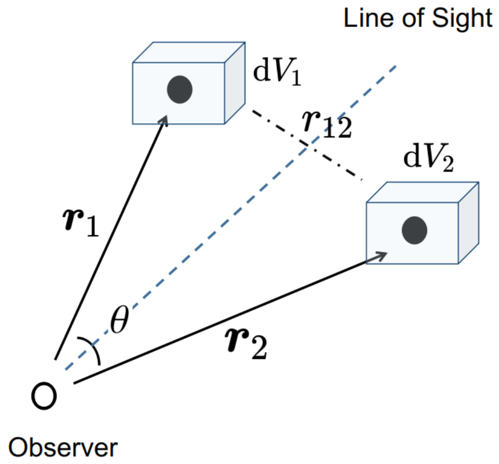

Figure 5.1: The cartoon diagram for description of two-point correlation function space.

Generalizing to the n-point correlation function:

$$\langle\delta(\boldsymbol{x}_1)...\delta(\boldsymbol{x}_n)\rangle \equiv \xi_n(\boldsymbol{x}_1, ..., \boldsymbol{x}_n). \tag{5.13}$$

Density field disturbance in real space is related to the one in Fourier space by

$$\delta(\boldsymbol{x}) = \int \frac{\mathrm{d}^3\boldsymbol{k}}{(2\pi)^3}\delta(\boldsymbol{k})\exp(i\boldsymbol{k}\cdot\boldsymbol{x}) \ . \tag{5.14}$$

The correlation functions in Fourier space can be written as

$$\begin{aligned}\langle\delta(\boldsymbol{k}_1)\delta(\boldsymbol{k}_2)\rangle &= (2\pi)^3\delta_D(\boldsymbol{k}_{12})P(\boldsymbol{k}_1,\boldsymbol{k}_2),\\ \langle\delta(\boldsymbol{k}_1)\delta(\boldsymbol{k}_2)\delta(\boldsymbol{k}_3)\rangle &= (2\pi)^3\delta_D(\boldsymbol{k}_{123})B(\boldsymbol{k}_1,\boldsymbol{k}_2,\boldsymbol{k}_3),\\ \langle\delta(\boldsymbol{k}_1)...\delta(\boldsymbol{k}_4)\rangle &= (2\pi)^3\delta_D(\boldsymbol{k}_{1234})T(\boldsymbol{k}_1,\boldsymbol{k}_2,\boldsymbol{k}_3,\boldsymbol{k}_4),\end{aligned} \tag{5.15}$$

where $\boldsymbol{k}_{i...j} = \boldsymbol{k}_i + ... + \boldsymbol{k}_j$. Above P, B, T express the Power Spectrum, Bispectrum and Trispectrum, respectively. In the following, we focus on the 2P CCF.

The correlation function at a distance of r (where we need only the modulus of the vector, because of statistical homogeneity and isotropy of the Universe) is expressed by

$$\xi(r) \equiv \langle \delta(\vec{x})(\delta(\vec{x} + \boldsymbol{r})) \rangle, \tag{5.16}$$

where brackets indicate volume average (that assuming ergodicity corresponds to ensemble average).

The power spectrum is the Fourier transform of the correlation function:

$$P(k) = \int \mathrm{d}^3 r \xi(r) e^{-ik \cdot r}. \tag{5.17}$$

5.4.2 Angular Correlation Function

In the analysis of large-scale correlations, it is often natural, to perform calculations based on the angular distance rather than on the physical distance. Here we introduce the *Angular correlation function* (ACF).

In the equation 5.11, the distance between two objects is $r_{12}(\theta)$, and, if measured from a third point, can be computed as

$$r_{12}(\theta) = |\boldsymbol{r}_1 - \boldsymbol{r}_2| = \left(r_1(z_1)^2 + r_2(z_2)^2 - 2r_1(z_1)r_2(z_2)\cos\theta\right)^{1/2}, \tag{5.18}$$

where the meaning of θ can be seen from Fig. 5.1.

Let us now derive the joint probability of finding numbers $\bar{N}$ of a pair in which the solid angle Ω_1 and Ω_2 are occupied by two galaxies with index 1 and 2:

$$\mathrm{d}P = \bar{N}_1 \bar{N}_2 \Omega_1 \Omega_2 (1 + \omega_{12}(\theta)) \tag{5.19}$$

Similar to the 3D case with spatial correlation function ξ_{12}, the ACF ω_{12} as a function of the separation angle θ can be derived from above equation.

The ACF is then obtained as a simple projection of

$$\begin{aligned} \omega(\theta) &\equiv \left\langle \delta_1(\hat{\boldsymbol{n}})\delta_2(\hat{\boldsymbol{n}}+\hat{\theta}) \right\rangle \\ &= \int \mathrm{d}z_1\phi(z_1) \int \mathrm{d}z_2\phi(z_2)\xi\left[r_1(z_1), r_2(z_2), \theta\right], \end{aligned} \tag{5.20}$$

where θ here (also in Fig. 5.1) is the angle between directions $\hat{\boldsymbol{n}}$ and $\hat{\boldsymbol{n}}+\hat{\theta}$. ϕ is the radial selection function and we assume that it can be modeled as a product of an angular mask and a radial selection here

$$\delta(\hat{\boldsymbol{n}}) = \int \mathrm{d}\phi(z)\delta(\hat{\boldsymbol{n}}, z), \tag{5.21}$$

and e.g., for galaxy count, $\phi(z)$ can be expressed as

$$\phi(z) = \frac{\mathrm{d}N}{\mathrm{d}z}W(z), \tag{5.22}$$

where $W(z)$ is *Window Function* for weighting the density field along the redshift but is direction-independent.

5.4.3 Spherical Harmonic Space

Since we project over the celestial sphere, it is useful to adopt a 2D expansion in Spherical Harmonics.

(θ, ϕ) expresses one direction on the unit spherical surface, and any square-integrable function $f(\theta, \phi)$ representing the intensity sky map can be expanded through the linear combination:

$$f(\theta, \phi) = \sum_{\ell=0}^{\infty} \sum_{m=-\ell}^{\ell} a_{\ell m} Y_{\ell m}(\theta, \phi), \tag{5.23}$$

where $a_{\ell m}$ are the coefficients of the expansion.

The spherical harmonic functions are given by

$$Y_{\ell m}(\theta,\phi)=\sqrt{\frac{(2\ell+1)}{4\pi}\frac{(\ell-m)!}{(\ell+m)!}}P_{\ell m}(\cos\theta)e^{im\phi}, \tag{5.24}$$

where $P_{\ell m}$ represents the Legendre polynomial and ℓ is called *multipole*.

Spherical harmonic functions constitute a complete set of orthogonal functions

$$\int_0^{\pi}\int_0^{2\pi} Y_{\ell m}(\theta,\phi)Y_{\ell' m'}(\theta,\phi)\sin(\theta)\mathrm{d}\phi\mathrm{d}\theta=\delta_{\ell\ell'}\delta_{mm'}, \tag{5.25}$$

where δ_{ij} is the Kronecker δ function.

The angular power spectrum of cross-correlation between two observed intensity sky maps can be defined as

$$C_\ell=\frac{1}{2\ell+1}\sum_{m=-\ell}^{\ell}a_{\ell m}^{(1)}a_{\ell m}^{(2)*}. \tag{5.26}$$

The CCF statistics provides a complementary information to Cross APS (hereafter is CAPS), they are connected by

$$\mathrm{CCF}(\theta)=\sum_{\ell}\frac{2\ell+1}{4\pi}C_\ell P_\ell\left[\cos(\theta)\right], \tag{5.27}$$

where P_ℓ are the Legendre polynomials.

These equations will be used in the sections 6 and 7, and the study of C_ℓ's provides the same information about clustering and anisotropy in LSS as the 2P CCF.

We now plug real physical quantities as the intensity $I_g(\hat{\boldsymbol{n}})$ of γ-ray astrophysical sources along a certain LOS direction $\hat{\boldsymbol{n}}$ into equation 5.23.

The disturbance is $\delta I_g(\hat{\boldsymbol{n}}) \equiv I_g(\hat{\boldsymbol{n}}) - \langle I_g \rangle$, and using the spherical harmonic expansion $\delta I_g(\hat{\boldsymbol{n}}) = \langle I_g \rangle \sum_{\ell m} a_{\ell m} Y_{\ell m}(\hat{\boldsymbol{n}})$, with coefficient $a_{\ell m}$ given by:

$$
\begin{aligned}
a_{\ell m} &= \frac{1}{\langle I_g \rangle} \int \mathrm{d}\hat{\boldsymbol{n}}\, \delta I_g(\hat{\boldsymbol{n}})\, Y^*_{\ell m}(\hat{\boldsymbol{n}}) \\
&= \frac{1}{\langle I_g \rangle} \int \mathrm{d}\hat{\boldsymbol{n}} \int \mathrm{d}D_c\, f_g(D_c, \boldsymbol{r}) W(D_c)\, Y^*_{\ell m}(\hat{\boldsymbol{n}}).
\end{aligned}
\tag{5.28}
$$

$f_g \equiv g(D_c, \hat{\boldsymbol{n}}) / \langle g(D_c, \hat{\boldsymbol{n}}) \rangle - 1$, $g(D_c, \hat{\boldsymbol{n}})$ indicates the density field of sources, D_c is the radial comoving distance, and here the window function $W(D_c)$ is related to the total intensity by,

$$
\langle I_g \rangle = \int dD_c\, W(D_c). \tag{5.29}
$$

The Rayleigh Expansion of plane wave, Spherical Bessel functions j_ℓ and the spatial Fourier transform of f_g can be used in equation 5.28 to obtain:

$$
\begin{aligned}
a_{\ell m} &= \frac{1}{\langle I_g \rangle} \int \mathrm{d}\hat{\boldsymbol{n}} \int \mathrm{d}D_c \frac{\mathrm{d}\boldsymbol{k}}{(2\pi)^3} \hat{f}_g(D_c, \boldsymbol{k}) e^{i\boldsymbol{k}\cdot\boldsymbol{r}} W(D_c) Y^*_{\ell m}(\hat{\boldsymbol{n}}) \\
&= \frac{1}{\langle I_g \rangle} \int \int \mathrm{d}\hat{\boldsymbol{n}}\, \mathrm{d}D_c \frac{\mathrm{d}\boldsymbol{k}}{2\pi^2} \hat{f}_g(D_c, \boldsymbol{k}) \\
&\times \left[\sum_{\ell' m'} i^{\ell'} j_{\ell'}(kD_c) Y^*_{\ell' m'}(\hat{\boldsymbol{k}}) Y_{\ell' m'}(\hat{\boldsymbol{n}}) \right] W(D_c) Y^*_{\ell m}(\hat{\boldsymbol{n}}) \\
&= \frac{i^\ell}{\langle I_g \rangle} \int \mathrm{d}D_c\, W(D_c) \int \frac{\mathrm{d}\boldsymbol{k}}{2\pi^2}\, \hat{f}_g(D_c, \boldsymbol{k}) j_\ell(kD_c) Y^*_{\ell m}(\hat{\boldsymbol{k}}) \,.
\end{aligned}
\tag{5.30}
$$

Combining equation 5.26 and 5.30, we get

$$
\begin{aligned}
C_\ell^{(ij)} &= \frac{1}{\langle I_i\rangle\langle I_j\rangle}\int \mathrm{d}D_c\, W_i(D_c)\int \mathrm{d}D'_c\, W_j(D'_c)\\
&\times \int \frac{\mathrm{d}\boldsymbol{k}}{2\pi^2}\int \frac{\mathrm{d}\boldsymbol{k}'}{2\pi^2}\,\langle \hat{f}_{g_i}(D_c,\boldsymbol{k})\hat{f}^*_{g_j}(D'_c,\boldsymbol{k}')\rangle j_\ell(kr)j_{\ell'}(k'r')Y_{\ell m}(\hat{\boldsymbol{k}})Y^*_{\ell' m'}(\hat{\boldsymbol{k}}')\\
&= \frac{2}{\pi\langle I_i\rangle\langle I_j\rangle}\int \mathrm{d}D_c\, W_i(D_c)\int \mathrm{d}D'_c\, W_j(D'_c)\\
&\times \int \mathrm{d}\boldsymbol{k}\; P_{ij}(k,D_c,D'_c)j_\ell(kr)j_{\ell'}(kr')Y_{\ell m}(\hat{\boldsymbol{k}})Y^*_{\ell' m'}(\hat{\boldsymbol{k}})\\
&= \frac{2}{\pi\langle I_i\rangle\langle I_j\rangle}\int \mathrm{d}D_c\, W_i(D_c)\int dD'_c\, \mathrm{d}k\, k^2\, W_j(D'_c)P_{ij}(k,D_c,D'_c)j_\ell(kr)j_\ell(kr')\\
&= \frac{1}{\langle I_i\rangle\langle I_j\rangle}\int \frac{\mathrm{d}D_c}{D_c^2}W_i(D_c)\,W_j(D_c)P_{ij}(k=\ell/D_c,D_c).
\end{aligned}
\tag{5.31}
$$

In the last step of the above equation we introduced the Limber approximation [130]. P_{ij} is the power spectrum defined in equation 5.15, related to the the density fields of this section by

$$
\langle \hat{f}_{g_i}(D_c,\boldsymbol{k})\hat{f}^*_{g_j}(D'_c,\boldsymbol{k}')\rangle = (2\pi)^3\delta^3(\boldsymbol{k}-\boldsymbol{k}')P_{ij}(k,D_c,D'_c). \tag{5.32}
$$

This is important for the transformation. The 2P CCF can be expressed as

$$
\begin{aligned}
\xi_{ij}(\boldsymbol{x},\boldsymbol{y}) &\equiv \langle f_{g_i}(\boldsymbol{x})f_{g_j}(\boldsymbol{y})\rangle\\
&= \int \mathrm{d}m_1\,\mathrm{d}m_2\,\mathrm{d}^3\boldsymbol{x}_1\,\mathrm{d}^3\boldsymbol{x}_2\\
&\times \langle \sum_a \delta^3_D(\boldsymbol{x}_1-\boldsymbol{x}_a)\delta_D(m_1-m_a)\sum_b \delta^3_D(\boldsymbol{x}_2-\boldsymbol{x}_b)\delta_D(m_2-m_b)\rangle\\
&\times f_1(m_1,\boldsymbol{x}-\boldsymbol{x}_1)\,f_2(m_2,\boldsymbol{y}-\boldsymbol{x}_2)\\
&= \int \mathrm{d}m\,\mathrm{d}^3\boldsymbol{x}_1\frac{\mathrm{d}n}{\mathrm{d}m}f_1(\boldsymbol{x}-\boldsymbol{x}_1,m)f_2(\boldsymbol{y}-\boldsymbol{x}_1,m)\\
&+ \int \mathrm{d}m_1\,\mathrm{d}m_2\,\mathrm{d}^3\boldsymbol{x}_1\,\mathrm{d}^3\boldsymbol{x}_2\frac{\mathrm{d}n}{\mathrm{d}m_1}\frac{\mathrm{d}n}{\mathrm{d}m_2}f_1(\boldsymbol{x}-\boldsymbol{x}_1,m_1)\\
&\times f_2(\boldsymbol{y}-\boldsymbol{x}_2,m_2)\xi^{hh}(m_1,m_2,\boldsymbol{x}_1,\boldsymbol{x}_2).
\end{aligned}
\tag{5.33}
$$

To derive the above expression we considered the density field as the sum of independent perturbation seeds, such as a discrete mass region for a gravitational tracer. The mass is indicated by m, and the density is $\mathrm{d}n/\mathrm{d}m = \langle \sum_a \delta_D^3(\boldsymbol{x} - \boldsymbol{x}_a)\delta_D(m - m_a)\rangle$, where the brackets indicate the ensemble average of all perturbation distributions. One can check that:

$$\begin{aligned}&\langle \sum_a \delta_D^3(\boldsymbol{x}_1 - \boldsymbol{x}_a)\delta_D(m_1 - m_a) \sum_b \delta_D^3(\boldsymbol{x}_2 - \boldsymbol{x}_b)\delta_D(m_2 - m_b)\rangle = \\ &\frac{\mathrm{d}n}{\mathrm{d}m_1}\frac{\mathrm{d}n}{\mathrm{d}m_2}\left[1 + \xi^{hh}(m_1, m_2, \boldsymbol{x}_1 - \boldsymbol{x}_2)\right] + \frac{\mathrm{d}n}{\mathrm{d}m_1}\delta_D^3(\boldsymbol{x}_1 - \boldsymbol{x}_2)\delta_D(m_1 - m_2).\end{aligned} \tag{5.34}$$

The integrals over $\boldsymbol{x}_1$ and $\boldsymbol{x}_2$ would yield $\xi^{hh}(m_1, m_2, \boldsymbol{x} - \boldsymbol{y})$, with $\boldsymbol{x}_1 - \boldsymbol{x}_2 = (\boldsymbol{x} - \boldsymbol{y}) + (\boldsymbol{y} - \boldsymbol{x}_2) - (\boldsymbol{x} - \boldsymbol{x}_1)$.

On large scales, the bias determines $\xi^{hh}(m_1, m_2, \boldsymbol{x} - \boldsymbol{y}) \approx b(m_1)b(m_2)\xi(\boldsymbol{x} - \boldsymbol{y})$. The $\xi(\boldsymbol{x} - \boldsymbol{y})$ can be taken outside of the integrals over m_1 and m_2, it makes the two integrals separately. Fig. 5.2 shows a cartoon illustrating the *1 halo* (1h) and *2 halo* (2h) terms. The last item ξ^{hh} is the two-point correlation between two halos. Therefore, when considering large typical halo, $\xi^{2h}(\boldsymbol{x} - \boldsymbol{y}) \approx \xi^{hh}(\boldsymbol{x} - \boldsymbol{y}) \approx \xi^{lin}(\boldsymbol{x} - \boldsymbol{y})$, in general the 2h term is roughly equal to the linear correlation function.

Thus, we can separate the ξ by

$$\xi(\boldsymbol{x} - \boldsymbol{y}) = \xi^{1h}(\boldsymbol{x} - \boldsymbol{y}) + \xi^{2h}(\boldsymbol{x} - \boldsymbol{y}). \tag{5.35}$$

When matter is distributed in multiple halos, we can write the matter density in a point $\boldsymbol{x}$ as

$$\begin{aligned}\rho(\boldsymbol{x}) &= \sum_i f_i(\boldsymbol{x} - \boldsymbol{x}_i) = \sum_i \rho(\boldsymbol{x} - \boldsymbol{x}_i|m_i) = \sum_i m_i u(\boldsymbol{x} - \boldsymbol{x}_i|m_i) \\ &= \sum_i \int \mathrm{d}m\mathrm{d}^3\boldsymbol{y}\delta(m - m_i)\delta^3(\boldsymbol{y} - \boldsymbol{x}_i)m\, u(\boldsymbol{x} - \boldsymbol{y}|m),\end{aligned} \tag{5.36}$$

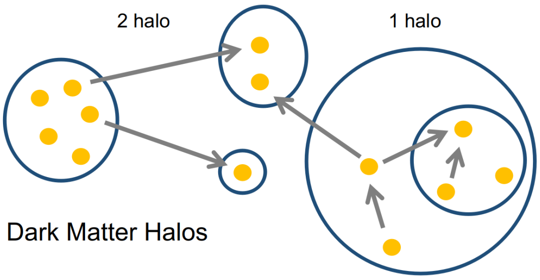

Figure 5.2: The cartoon diagram depicting 1 halo and 2 halo terms.

where f_i is the i-th halo density profile, the second equation is based on the assumption that the density around the halo only depends on its mass, and the last one introduces a normalization function $\int \mathrm{d}^3\boldsymbol{y}\ u(\boldsymbol{x}-\boldsymbol{y}|m) = 1$. The number density of DM halo is

$$< \sum_i \delta(m-m_i)\delta^3(\boldsymbol{y}-\boldsymbol{x}_i) > \equiv n(m), \tag{5.37}$$

and average density is

$$\begin{aligned}\bar{\rho} &=< \rho(\boldsymbol{x}) >=< \sum_i m_i\ u(\boldsymbol{x}-\boldsymbol{x}_i|m_i) > \\ &= \int \mathrm{d}m n(m) m \int \mathrm{d}^3\boldsymbol{y} u(\boldsymbol{x}-\boldsymbol{y}|m) \\ &= \int \mathrm{d}m n(m) m.\end{aligned} \tag{5.38}$$

Detailing the last two items, we have

$$\xi^{1h}(\boldsymbol{x}-\boldsymbol{y}) = \int \mathrm{d}m \frac{m^2 n(m)}{\bar{\rho}^2} \int \mathrm{d}^3\boldsymbol{r} u(\boldsymbol{r}|m) u(\boldsymbol{r}+\boldsymbol{x}-\boldsymbol{y}|m), \tag{5.39}$$

$$\begin{aligned}\xi^{2h}(\boldsymbol{x}-\boldsymbol{y}) &= \int \mathrm{d}m_1 \frac{m_1^2 n(m_1)}{\bar{\rho}} \int \mathrm{d}m_2 \frac{m_2^2 n(m_2)}{\bar{\rho}} \\ &\times \int \mathrm{d}^3\boldsymbol{x_1} u(\boldsymbol{x}-\boldsymbol{x_1}|m_1) \int \mathrm{d}^3\boldsymbol{x_2} u(\boldsymbol{x}-\boldsymbol{x_2}|m_2) \\ &\times \xi^{hh}(\boldsymbol{x_1}-\boldsymbol{x_2}|m_1, m_2).\end{aligned} \tag{5.40}$$

In an homogeneous universe, the density perturbation spectrum has no preferred direction, so in a 3D space, the correlation function is

$$\xi(r) = \frac{V}{(2\pi)^3} \int P(k) \frac{\sin kr}{kr} 4\pi k^2 dk. \tag{5.41}$$

Clearly, the power spectrum is the Fourier transform of ξ. It can be also expressed in a dimensionless form:

$$\Delta^2(k) \equiv \frac{V}{(2\pi)^3} 4\pi k^3 P(k) = \frac{2}{\pi} k^3 \int_0^\infty \xi(r) \frac{\sin kr}{kr} r^2 \mathrm{d}r. \tag{5.42}$$

Its physical meaning can be understood by noting that $\Delta^2(k) = 1$ represents the order unit density fluctuation around the wavenumber k.

Analogously, in Fourier space, the power spectrum can be split into 1h and 2h terms, given by:

$$P(k) = P^{1h}(k) + P^{2h}(k), \tag{5.43}$$

$$P^{1h}(k) = \int \mathrm{d}m n(m) (\frac{m}{\bar{\rho}})^2 u(k|m)^2, \tag{5.44}$$

and

$$\begin{aligned} P^{2h}(k) = &\int \mathrm{d}m_1 n(m_1) (\frac{m_1}{\bar{\rho}}) u(k|m_1) \\ \times &\int \mathrm{d}m_2 n(m_2) (\frac{m_2}{\bar{\rho}}) u(k|m_2) P^{hh}(k|m_1, m_2), \end{aligned} \tag{5.45}$$

where $u(k|m)$ is the Fourier transform of the halo density profile under consideration, e.g, here we adopted the formation of equation 2.43 (also see the Fig. 2.5), then we can obtain

$$P^{hh}(k|m_1, m_2) \approx b(m_1)\, b(m_2) P^{\mathrm{lin}}(k). \tag{5.46}$$

CHAPTER 6

Constraining the WIMP dark matter

In chapter 2, I have introduced the theoretical foundations and observational evidences for the evolution of our Universe. DM as the key factor related to the formation of large scale structures, contributes about 27% [15] to the total energy density of the universe, and it is one of the most essential components.

As I already mentioned in section 3, plenty of DM theoretical models have been proposed in the literature. Among them, WIMP DM is one of the most promising candidates. They have non-negligible interactions with ordinary substances, and are expected to be able to annihilate or decay producing high energy γ-ray photons.

The indirect detection method consists in looking for products of the annihilation or decay of DM particles such as γ-ray photons.

The study of the CAPS between gravitational tracers of DM and electromagnetic signals (the UGRB full-sky maps in the case of γ-rays) can be a powerful tool to constrain DM microscopic properties. Previous attempts to search for DM already brought a large amount of results, using different DM tracers like galaxies [105, 131–139], galaxies clusters [111, 140], CMB lensing [141, 142], weak lensing cosmic shear [143–149].

Chapter 4 has outlined the sources contributing to the UGRB, which include various astrophysical sources [150–153]. The cross-correlation between the UGRB and other observations can improve the characterization of the UGRB components.

In our research, we use the galaxy cluster catalogs to trace the location of DM. We fit the CAPS measurements with a physical model including astrophysical γ-ray emitters and WIMP DM, in order to obtain bounds on the WIMP properties. Data and methods were introduced in chapter 5 and chapter 4.

6.1 Theoretical Background

6.1.1 Dark Matter

In this chapter, I consider γ-rays generated from WIMP DM and correlate them with the gravitational DM tracer, given by galaxy cluster catalogs. The window function of the cosmological signal originated from DM annihilations can be written as

$$\begin{aligned} W_{\delta^2}(D_c) =& \frac{(\Omega_{\rm DM}\rho_c)^2}{4\pi}\frac{\langle\sigma_{\rm ann}v\rangle}{2m_{\rm DM}^2}[1+z]^3\Delta^2(D_c) \\ & \int_{E_\gamma > E_{\rm min}} {\rm d}E_\gamma \frac{{\rm d}N_{\delta_2}}{{\rm d}E_\gamma}[E_\gamma(D_c)]e^{-\tau[D_c,E_\gamma(D_c)]}, \end{aligned} \tag{6.1}$$

where $m_{\rm DM}$ is the mass of DM and $\langle\sigma_{\rm ann}v\rangle$ is the velocity-averaged annihilation cross section of the DM. ${\rm d}N_{\delta^2}/{\rm d}E_\gamma$ expresses the γ-ray energy spectrum from final states of its annihilation or decay. Here we use simulation table `PPPC4DMID` [154] to do calculation of final products energy spectrum, and it was verified with the events from `Pythia` and `Herwig`[1]. We considered four channels of DM annihilation separately: $\tau^+\tau^-$, $b\bar{b}$, W^+W^- and $\mu^+\mu^-$, with 100% branching ratio in each case. The factor $\tau\left[D_c, E_\gamma(D_c)\right]$ is the attenuation function of γ-rays caused by the absorption due to pair production with extragalactic background light [155].

Photons from both prompt emission and inverse Compton processes are considered here. Prompt γ-ray emission traces the spatial morphology along LOS of the DM density, for which, as we mentioned in chapter 2, a NFW profile is chosen.

Inverse Compton radiation is computed under the assumption of no spatial diffusion of electrons and positrons produced by the DM annihilation, taking only the CMB as target photons and disregarding synchrotron losses. The first supposition is driven by the fact that the average size of a cluster is typically much longer than the diffusion length of $\mathrm{GeV/TeV}$ electrons. The latter two (no spatial diffusion and no synchrotron loss) are educated guesses: such model-independent description was adopted in former works like Ref. [156] and can avoid including an uncertain characterization of the interstellar radiation field and magnetic field in all halos.

The *Clumping factor* $\Delta^2(D_c(z))$ in the equation 6.1 is defined as

$$\begin{aligned}\Delta^2(D_c(z)) \equiv \frac{\langle\rho^2_{\mathrm{DM}}\rangle}{\bar{\rho}^2_{\mathrm{DM}}} = &\int_{M_{\min}}^{M_{\max}} \mathrm{d}M \frac{\mathrm{d}n}{\mathrm{d}M}(M,z) \\ &\times\left[1+b_{\mathrm{sub}}(M,z)\right]\int \mathrm{d}^3\boldsymbol{x}\,\frac{\rho^2_h(\boldsymbol{x}|M,z)}{\bar{\rho}^2_{\mathrm{DM}}}.\end{aligned} \tag{6.2}$$

This quantity depicts the situation of emission “boosted” by the DM clumpiness with respect to the case of a smooth density. The DM substructures contribution is accounted

---

[1] http://home.thep.lu.se/Pythia/ for `Pythia`, https://herwig.hepforge.org/ for `Herwig`.

for by $b_{\rm sub}$. We considered three models: One is used in the main analysis of this work [157], and with the other two we try to bracket the uncertainty, considering a lower concentration [158] and a higher concentration [159]. They lead to lower or higher expected γ-ray flux from DM and, since the question is open (i.e., current N-body simulations are not able to resolve the small scales of DM substructures), this leaves uncertainties in the final results. So we will present all three models. We can notice that the equation of the window function 6.1 relies on the mass and annihilation rate of DM particles. In our CAPS analysis, we fix other parameters and derive upper limits as a function of the DM mass and annihilation rate.

The 3D power spectrum of cross-correlation between cluster catalogs and γ-rays from annihilataing DM is given by

$$P^{1h}_{C_j,\delta^2}(k,z) = \int_{M_{\rm min}}^{M_{\rm max}} dM\, \frac{dn}{dM}\, \frac{\langle N_{C_j}\rangle}{\bar{n}_{C_j}}\, \frac{u^2(k|M)}{\Delta^2}, \tag{6.3}$$

and

$$\begin{aligned} P^{2h}_{C_j,\delta^2}(k,z) = &\left[\int_{M_{\rm min}}^{M_{\rm max}} dM\, \frac{dn}{dM} b_h(M) \frac{\langle N_{C_j}\rangle}{\bar{n}_{C_j}}\right] \\ &\times \left[\int_{M_{\rm min}}^{M_{\rm max}} dM\, \frac{dn}{dM} b_h(M) \frac{u^2(k|M)}{\Delta^2}\right] P^{\rm lin}(k)\,, \end{aligned} \tag{6.4}$$

where $u^2(k|M)$ is the Fourier transform of square of the DM spatial profile (Here we adopted NFW profile, the analytical solution is shown in appendix C), and b_h is the halo bias. $\bar{n}_{C_j}(z) = \int dM \langle N_{C_j}\rangle\, dn/dM$ refers to the average number density of galaxy clusters at the redshift z.

6.1.2 Astrophysical Sources

Among the contributions of the UGRB one has certainly to include those from astrophysical sources. For the γ-ray sources of SFG, BLZ and mAGN, the window functions can be expressed in terms of their γ-ray luminosity function Φ:

$$\begin{aligned} W_S(D_c) =& D_c^2(z) \int_{\mathcal{L}_{\min}}^{\mathcal{L}_{\max}} \mathrm{d}\mathcal{L}\, \Phi_S(\mathcal{L}, z) \\ & \times \frac{\mathrm{d}N_S}{\mathrm{d}E}(\mathcal{L}, z) \times e^{-\tau[E(1+z),z]}, \end{aligned} \tag{6.5}$$

where $\mathcal{L}$ is the γ-ray rest-frame luminosity in energy interval 0.1 to $100\,\mathrm{GeV}$, S represents a generic population. $\mathrm{d}N_S/\mathrm{d}E$ is the correspondent energy spectrum. The upper limit of integration is $\mathcal{L}_{\max}\left(F_{\text{sens}}, z\right)$ given by the sensitivity of detection $F_{\text{sens}} = 5 \times 10^{-10}\,\text{photons cm}^{-2}\text{s}^{-1}$ (here we refer to the *Fermi*-LAT):

$$\mathcal{L}_{\max}\left(F_{\text{sens}}, z\right) = 4\pi D_L^2(z) F_{\text{sens}}(1+z)^{-2+\Gamma_S}, \tag{6.6}$$

where D_L is the luminosity distance[2]. and Γ_S is the power-law index of the energy spectrum.

Blazars There are actually many kinds of Blarzars (BLZ), which are generally divided into two types: BLLac and FSRQ. The γ-ray luminosity function is adopted from Ref. [160, 161]. Luminosity Dependent Density Evolution (LDDE) of blazars can be described by

$$\Phi\left(L_\gamma, z=0, \Gamma\right) = \frac{A}{\ln(10) L_\gamma}\left[\left(\frac{L_\gamma}{L_*}\right)^{\gamma_1} + \left(\frac{L_\gamma}{L_*}\right)^{\gamma 2}\right]^{-1} \times e^{-\frac{(\Gamma-\mu(L_\gamma))^2}{2\sigma^2}}. \tag{6.7}$$

---

[2] The luminosity distance $D_L \equiv \sqrt{L/(4\pi F)}$, where L is the luminosity of the object and F is the measured flux from the object.

A smoothly-joined double power-law function in parentheses expresses the luminosity function of local blazars. The exponential term means that the intrinsic distribution of photon spectral indexes at a given redshift and luminosity is taken to follow a Gaussian. The average spectral index is expressed as

$$\mu\left(L_\gamma\right)=\mu^*+\beta\times\left(\log_{10}\left(L_\gamma\right)-46\right). \tag{6.8}$$

The luminosity function dependent on the redshift is

$$\Phi\left(L_\gamma, z, \Gamma\right)=\Phi\left(L_\gamma, z=0, \Gamma\right)\times e\left(z, L_\gamma\right), \tag{6.9}$$

where

$$e\left(z, L_\gamma\right)=\left[\left(\frac{1+z}{1+z_c\left(L_\gamma\right)}\right)^{-p_1\left(L_\gamma\right)}+\left(\frac{1+z}{1+z_c\left(L_\gamma\right)}\right)^{-p_2}\right]^{-1}. \tag{6.10}$$

The two parameters are defined as

$$p_1\left(L_\gamma\right)=p_1^*+\tau\times\left(\log_{10}\left(L_\gamma\right)-46\right), \tag{6.11}$$

and

$$z_c\left(L_\gamma\right)=z_c^*\cdot\left(L_\gamma/10^{48}\right)^\alpha. \tag{6.12}$$

In this work, we unified the BLLac and FSRQ, the parameters for their LDDE is adopted from Ref. [160, 161]. The bias of the sources here can be given by the redshift-dependent AGN bias proposed by Ref. [162], the same for both BLLac and FSRQ.

Star Forming Galaxy SFG luminosity function is derived from the best fit of infrared photometric one [163], and assuming that γ-rays are related to infrared luminosity. The infrared luminosity function is composed of three different contributions. They are normal spiral galaxies (SP), starburst (SB) and galaxies hosting an AGN but with infrared emission still mostly provided by by star-forming activity (SF-AGN).

The final γ-ray luminosity function is obtained from the combination of these three components. The spectral index is taken to be $\Gamma_{\mathrm{SFG}} = -2.7$ for a single power law.

Misaligned Active Galactic Nucleus Similar to SFG, the misaligned Active Galactic Nucleus (mAGN) also needs the observational results from other energy bands to determine the γ-ray luminosity function. Here we used the relationship between the radio band and the γ-ray band from Ref. [153] and the radio luminosity function from Ref. [164]. The redshift distribution is similar to the one of SFGs, so there will be some degeneracy between these two components. The index of power-law for the energy spectrum is $\Gamma_{\mathrm{mAGN}} = -2.37$.

For the astrophysical sources, the one-halo contribution to the cross-correlation power spectrum with cluster catalogs is given by

$$P^{1h}_{C_j,S_n}(k,z) = \int_{\mathcal{L}_{\min,i}(z)}^{\mathcal{L}_{\max,i}(z)} d\mathcal{L}\,\Phi_n(\mathcal{L},z)\,\frac{\mathcal{L}}{\langle f_{S_n}\rangle}\,\frac{\langle N_{C_j}(\mathcal{L})\rangle}{\bar{n}_{C_j}}, \tag{6.13}$$

and the two-halo part is

$$\begin{aligned} P^{2h}_{C_j,S_n}(k,z) = & \left[\int_{\mathcal{L}_{\min,i}(z)}^{\mathcal{L}_{\max,i}(z)} d\mathcal{L}\,\Phi_n(\mathcal{L},z)\,b_{S_n}(\mathcal{L})\,\frac{\mathcal{L}}{\langle f_{S_n}\rangle}\right] \\ & \times\left[\int_{M_{\min}}^{M_{\max}} dM\,\frac{dn}{dM} b_h(M)\,\frac{\langle N_{C_j}\rangle}{\bar{n}_{C_j}}\right] P^{\mathrm{lin}}(k)\,. \end{aligned} \tag{6.14}$$

where $b_{S_n}(\mathcal{L})$ is the bias of the γ-ray astrophysical sources with respect to the matter for type n, and here we adopt $b_{S_n}(\mathcal{L}) = b_h(M(\mathcal{L}))$. The modeling of $M(\mathcal{L})$ is derived from Ref. [143], and is in agreement with autocorrelation studies in the Refs. [165–170].

6.1.3 Galaxy Clusters Catalog

The window function of the galaxy cluster catalogs is obtained from the observational data and can be expressed as

$$W_{C_j}(z) = \frac{4\pi D_c(z)^2}{N_{C_j}} \int dM \, \frac{d^2 n_{C_j}}{dM\, dV} \,, \tag{6.15}$$

The number of objects contained in a catalog is

$$N_{C_j} = \int dM \, dV \, \frac{d^2 n_{C_j}}{dM\, dV} \,. \tag{6.16}$$

We take redshift and mass estimates provided by the different galaxy cluster catalogs, and recast them according to our conventions (essentially, converting virial mass or M_{200} into M_{500}) where necessary.

6.2 Phenomenological Model of CAPS Signals

In addition to above theoretical sources, we also describe how to model the expected CAPS between the γ-ray sky and galaxy clusters in a way that is independent from the details of the physical models introduced above. There are two expected contributions to the CAPS provided by different γ-ray emissions in the cluster: one can arise from compact sources located inside the cluster like AGNs and the other is a diffuse emission from the Intra-Cluster Medium (ICM). If the correlation between the γ-ray emission and clusters is at zero angular separation or, more concretely, if it is at scales smaller than the *Fermi*-LAT PSF, then the APS has a flat behavior in multipoles (besides the correction due to the *Fermi*-LAT beam window function). This contribution can be called *FLAT* (shot-noise) term and can be computed as:

$$C_{\ell,\mathrm{FLAT}}^{C_j\gamma_i} = \left(\frac{1}{N_{C_j}} \sum_{n=0}^{N_{C_j}} F_{\Delta E_i,j}^{\gamma} \right) W_\ell^{\Delta E_i} \,, \tag{6.17}$$

where N_{C_j} is the number of objects in the cluster catalog j, $F_{\Delta E_i,n}^{\gamma}$ is the γ-ray flux coming from the center of the cluster j in the energy bin ΔE_i. The beam window function $W_\ell^{\Delta E}$ reports the finite angular resolution of the *Fermi*-LAT instrument that suppresses high multipoles. It is given by $W_\ell(E) = 2\pi \int_{-1}^{1} \mathrm{d}\cos\theta \, P_\ell(\cos\theta) \, \mathrm{PSF}(\theta, E)$ and averaging over the energy bin by using an energy spectrum of index -2.3 [171].

Since actually we do not know the γ-ray flux coming from clusters and since γ-ray sources typically have energy spectra that can be well approximated by a power-law, we modify the equation 6.17 as

$$C_{\ell,\mathrm{FLAT}}^{C_j\gamma_i} \;=\; C_p^j \, \bar{E}_i^{-\alpha_{1,j}} \, \Delta E_i \, W_\ell^{\Delta E_i} \,, \tag{6.18}$$

where $\bar{E}_i = \sqrt{E_i \, E_{i+1}}$ represents the geometric mean of the lower and upper bounds of each energy bin, $\Delta E_i = E_{i+1} - E_i$ is the size of bins, C_p^j is the normalization of the power-law relation and spectral index shows as $\alpha_{1,j}$ (that will be obtained from the fit). The index j refers to the catalog of galaxy clusters we used in CAPS.

On top of the shot-noise, we expect also multipole-dependent contributions. As introduced in section 5.4, the 1h refers to the correlation between two points remaining in the same halo and 2h is for two points belonging to different physical halos. Generally speaking, for the cross-correlation that can appear on angular scales larger than the *Fermi*-LAT PSF, a 1h term would likely be the contribution from the extended ICM, while a 2h term is most probably associated to AGNs in different structures. For definiteness, since the prediction of γ-ray emission from ICM suffers of large uncertainties [172], we limit our modeling of the 2h term to the case of the more robust AGN emission.

All the ingredients in subsection 6.1.2 allow us to model a large-scale correlation, i.e., a non-flat dependence on the multipole angular scale. A certain level of flexibility is allowed to intercept possible large-scale deviations from the specific AGN emission. The second contribution is thus defined by a free power-law index for the energy dependence and a free overall normalization parameter:

$$C_{\ell,\mathrm{AGN}}^{C_j\gamma_i} = C_{\ell,\mathrm{FLAT}}^{C_j\gamma_i}(C_p^j, \alpha_{1,j}) + A_j(\frac{\bar{E}_i}{\bar{E}_0})^{-\alpha_{2,j}} \, \Delta E_i \, C_\ell^{\Delta E_0} \, W_\ell^{\Delta E_i}. \tag{6.19}$$

It contains the expected small-scale shot-noise term and adds an *AGN-like* model, with the fudging free parameters α_2 and A. The energy range of ΔE_0 is chosen to be $(1, 2)$ GeV, $\bar{E}_i$, selected from Tab. 4.1. Index j labels the galaxy catalog, for the sake of brevity we will omit it in the following section. There are two free parameters in the FLAT model, including the spectral index α_1 and the normalization factor C_p; while the AGN-like model is endowed with 2 additional free parameters, the spectral index α_2 and another normalization A, which is used to characterize the behavior of the non-flat part.

6.3 Statistical Analysis

This section includes the discussion on how to detect the cross-correlation signal between the low-redshift cluster catalogs introduced in chapter 4.3.2 and γ-rays from the *Fermi*-LAT maps, and also how to distinguish between the detection of a flat and a multipole-dependent signal.

To quantify the presence of a signal against a null hypothesis we define a signal to noise (SNR) ratio [173] for the null hypothesis:

$$\mathrm{SNR} = \frac{C_{\ell,\mathrm{DATA}}\, \Gamma^{-1}_{\ell\ell'}\, C_{\ell',\mathrm{MODEL}}}{\sqrt{C_{\ell,\mathrm{MODEL}}\, \Gamma^{-1}_{\ell\ell'}\, C_{\ell',\mathrm{MODEL}}}}\,, \tag{6.20}$$

where $C_{\ell,\mathrm{DATA}}$ is for the measured CAPS, $C_{\ell,\mathrm{MODEL}}$ is the model prediction that grabs the physical features and $\Gamma^{-1}_{\ell,\ell'}$ is the inverse of the CAPS covariance matrix. Theoretical models are described in the previous section, and the estimation of the covariance matrix is in appendix A. The model employed to assess the significance of the presence of a signal is $C_{\ell,\mathrm{MODEL}} = C_{\ell,\mathrm{FLAT}}$.

The calculation of SNR is performed using best-fitting parameters. As a second analysis we investigate whether a more refined and complete model for the cross APS is preferred over the simpler FLAT case. The statistical preference is determined by means of the χ^2 function

$$\chi^2 = \sum_{i=1}^{N_{\mathrm{bin}}} \sum_{\ell=\ell_{\mathrm{min}}}^{\ell_{\mathrm{max}}} \sum_{\ell'=\ell_{\mathrm{min}}}^{\ell_{\mathrm{max}}} [(C_{\ell,\mathrm{DATA}})^i - (C_{\ell,\mathrm{MODEL}})^i](\Gamma^{-1}_{\ell\ell'})^i[(C_{\ell',\mathrm{DATA}})^i - (C_{\ell',\mathrm{MODEL}})^i], \tag{6.21}$$

where i denotes the energy bins.

The best-fitting FLAT and AGN models are determined by maximizing the Gaussian likelihood $\mathcal{L}$ defined as:

$$-2\ln\mathcal{L} = \chi^2. \tag{6.22}$$

Then, the value of $\Delta\chi^2 = \chi^2_{\mathrm{FLAT}} - \chi^2_{\mathrm{AGN}}$ determine the preference between the two models.

We also involve the Akaike Information Criterion (AIC) [174] defined by

$$\mathrm{AIC} = 2m - 2\ln\mathcal{L}\,, \tag{6.23}$$

where m is the number of parameters of the model. This criterion can be used to estimate the information lost by a given model to further understand and compare the relative quality of models: the smaller is the information loss, the better the model can reproduce the data.

In principle, we do not expect the covariance matrix of a given energy bin to be Gaussian and in order to test it we look at the off-diagonal terms and compare them to diagonal ones by means of the coefficient:

$$r = \frac{\Gamma^{\gamma_i}_{\ell\ell'}}{\sqrt{\Gamma^{C\gamma_i}_{\ell\ell}\Gamma^{C\gamma_i}_{\ell'\ell'}}}. \tag{6.24}$$

One can verify that the size of off-diagonal terms of the mocks covariance matrix with respect to the diagonal ones. Concerning the covariance between different energy bins, we again find that the cross APS between galaxy catalogs and γ-rays is quite diagonal, especially for energy bins of the size of those adopted in our analysis. This can be seen by evaluating the Gaussian estimator for the covariance in energy (at fixed multipole):

$$\Gamma^{C\gamma_i\gamma_j}_{\ell\ell} \equiv \mathrm{cov}\left[C^{C\gamma_i}_{\ell}, C^{C\gamma_j}_{\ell}\right] = \frac{C^{CC}_{\ell}C^{\gamma_j\gamma_i}_{\ell} + C^{C\gamma_i}_{\ell}C^{C\gamma_j}_{\ell}}{(2\ell+1)f_{\mathrm{sky}}}. \tag{6.25}$$

The corresponding correlation coefficient is:

$$r_{\mathrm{E}} = \frac{\Gamma^{C\gamma_i\gamma_j}_{\ell\ell}}{\sqrt{\Gamma^{C\gamma_i\gamma_i}_{\ell\ell}\Gamma^{C\gamma_j\gamma_j}_{\ell\ell}}}. \tag{6.26}$$

Fig. 6.1 shows r_{E} for some selected angular scales from MCXCsub. For most of the angular scales, the off-diagonal elements of the covariance matrix are well below a 5%

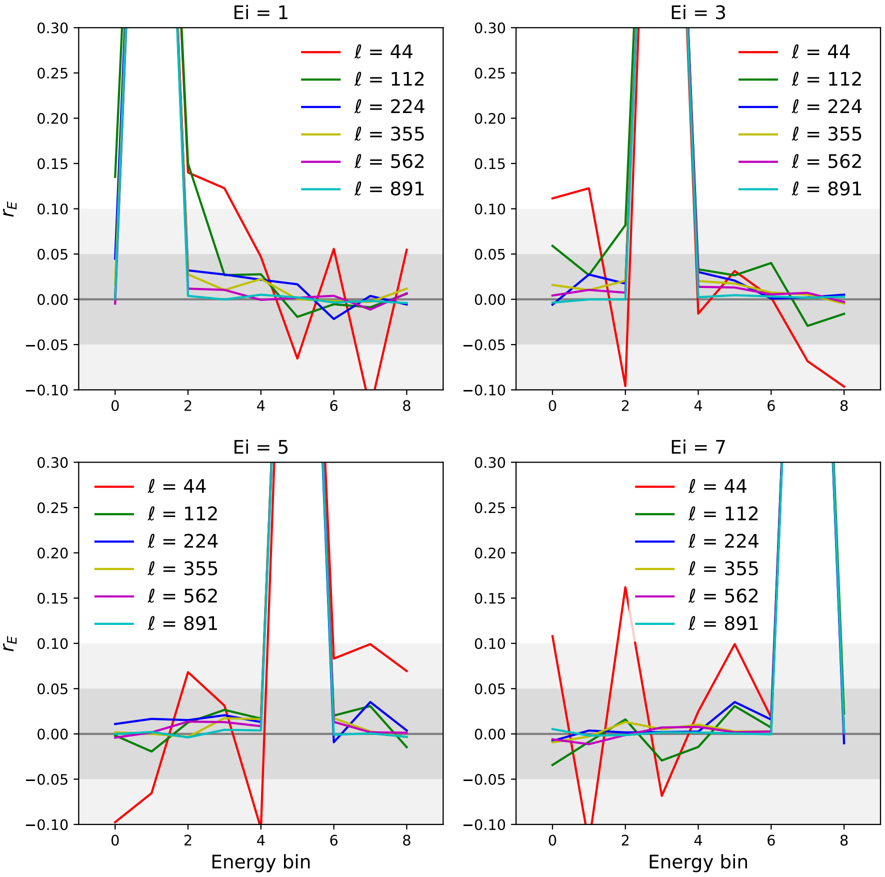

Figure 6.1: Cross-correlation coefficient 6.26 defined as the equation. It shows the size of the off-diagonal terms of the covariance matrix under energy bins. These four panels are selected arbitrarily from all energy bins, which behave pretty general. Each line identified by a different color to indicate a different multipole ℓ. While the horizontal axis stands for all other energy bins. The peaks appear when the two energy bins are the same, sit on the diagonal, its value is 1 according to the definition. The figure is taken from Ref. [175].

deviation from the diagonal elements. Only for smaller angular scales the effect reaches deviations of the order of 10%. Results are similar at different angular scales and for the other cluster catalogues.

6.4 Analysis of Results

6.4.1 Phenomenological Model Results

Fig. 6.2 shows the measured cross-correlation APS for four different cluster catalogs after binning in multipoles and taklng the third energy bin as an example. The error bars are the diagonal entries of the covariance matrix obtained from the mock analysis.

Fig. 6.3 is the average CAPS related to energy bin i, where $C_\ell^{C\gamma_i}$ is averaged over ℓ:

$$P_{E_i} = \frac{1}{\Delta\ell} \sum_{\ell_{\min}}^{\ell_{\max}} C_\ell^{C\gamma_i} \,, \tag{6.27}$$

the error bars of P_E are obtained from

$$\sigma^2_{P_{E_i}} = \frac{1}{\Delta\ell} \left(\frac{1}{\Delta\ell} \sum_{\ell_{\min}}^{\ell_{\max}} \sigma^2_{C_\ell^{C\gamma_i}} \right), \tag{6.28}$$

where $\sigma^2_{C_\ell^{C\gamma_i}} = \Gamma_{\ell\ell}^{C\gamma_i}$. To easy the visualization, the vertical coordinate of Fig. 6.3 has been multiplied by $E^{2.2}\Delta E^{-1}$.

We use MCMC techniques described above in order to determine the presence of a positive cross-correlation signal. Tab. 6.1 gives the SNR results obtained with the best fit of the featureless FLAT model.

According to Tab. 6.1, WHY18 and SDSSDR9 catalogs show weak positive correlation signals, while MCXCsub and HIGLUGCS have a more pronounced evidence of the existence of a correlation between cluster catalogs and γ-ray sources, since the SNR exceeds 3.

In order to discriminate between the two models introduced above, we further calculated $\Delta\chi^2 = \chi^2_{\mathrm{FLAT}} - \chi^2_{\mathrm{AGN}}$. Tab. 6.1 reveals that only MCXCsub shows a preference

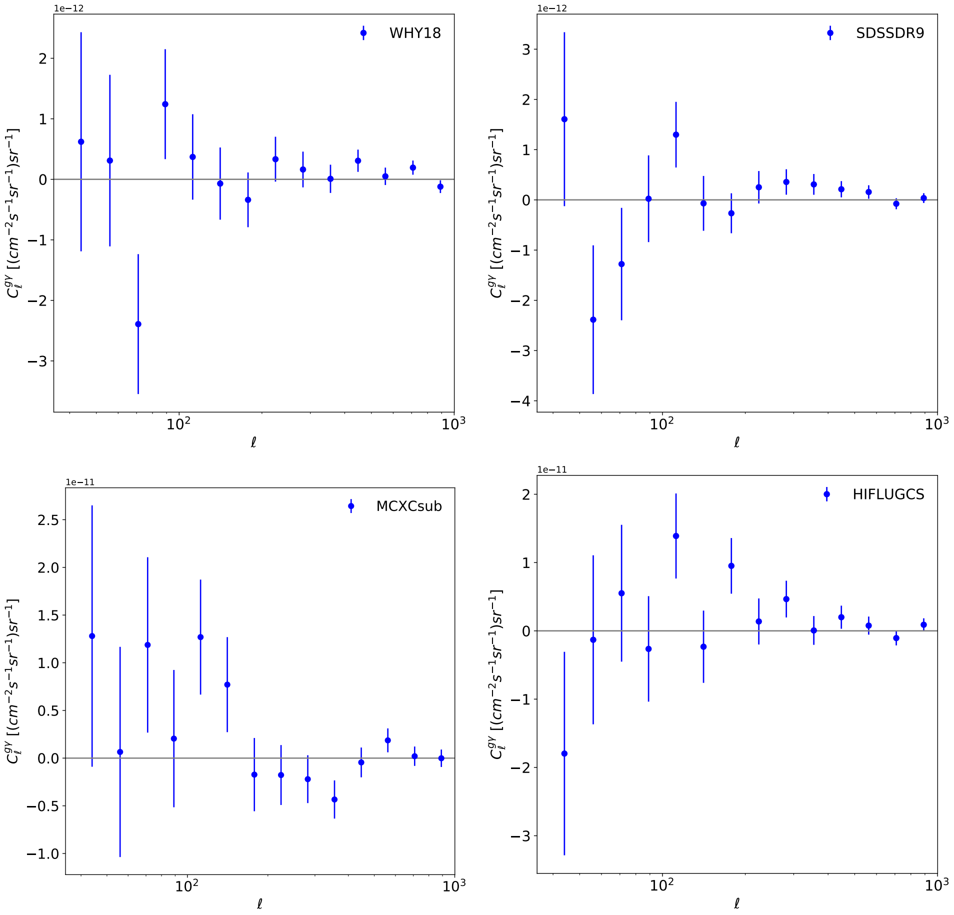

Figure 6.2: The APS of γ-rays and galaxy clusters. The error bars are obtained from the binned angular-power-spectrum covariance matrix estimated from 2,000 mocks. The figure is taken from Ref. [175].

Table 6.1: For each cluster catalog, we give the SNR and the difference between the best-fit χ^2 of the FLAT model and the AGN-like model.

Catalogue	Type	SNR	$\Delta\chi^2_{\mathrm{FLAT-AGN}}$
WHY18	infrared	2.1	0.6
SDSSDR9	optical	2.3	0.2
MCXCsub	X-ray	3.5	4.5
HIFLUGCS	X-ray	3.2	0.6

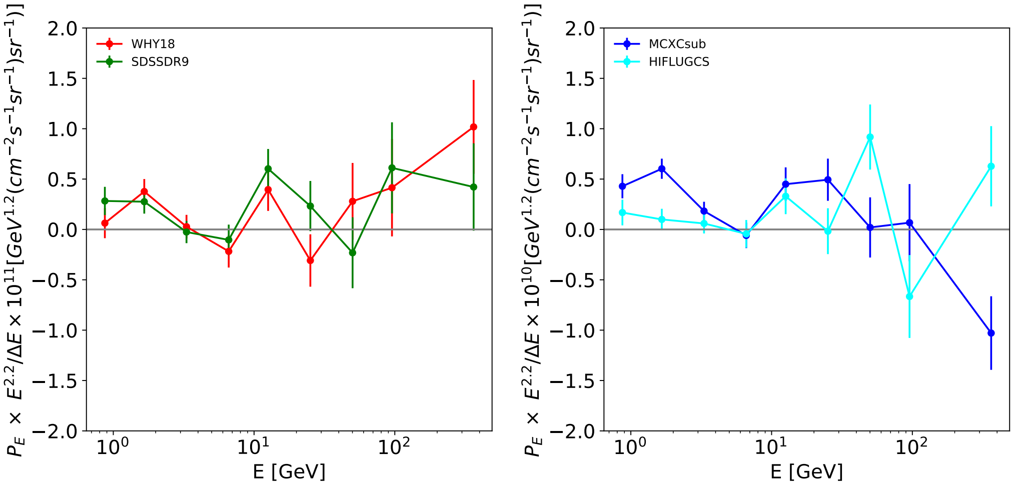

Figure 6.3: Energy spectrum P_E of the cross-correlation APS for each of the four cluster catalogs. The plot has redefined $E^{2.2}/\Delta E$ with ΔE, error bars are provided by the estimation from 2,000 mocks. The figure is taken from Ref. [175].

for a large scale correlation.

We would expect HIFLUGCS and MCXCsub samples to provide similar results, since the clusters in the two catalogs share similar mass function and flux distributions. On the other hand, a statistical difference of less than 2σ between two different samples of (possibly) the same population is nevertheless plausible. The AIC test confirms the preference for a large-scale contribution in MCXCsub: in particular $\mathrm{AIC}_{\mathrm{FLAT}} = 152.05$ against $\mathrm{AIC}_{\mathrm{AGN}} = 151.35$ is the indication that the AGN model allows for a smaller loss of information, even though with a somewhat smaller evidence than in the χ^2 analysis. The AIC results of the other three cluster catalogs are in the opposite direction.

Fig. 6.4 shows the allowed regions obtained for the AGN model parameters in the MCXCsub case. The contours refer to the 68% (dark blue) and 95% (light blue) confidence levels. The constraints are not very strong, but consistent with an AGN-like model,

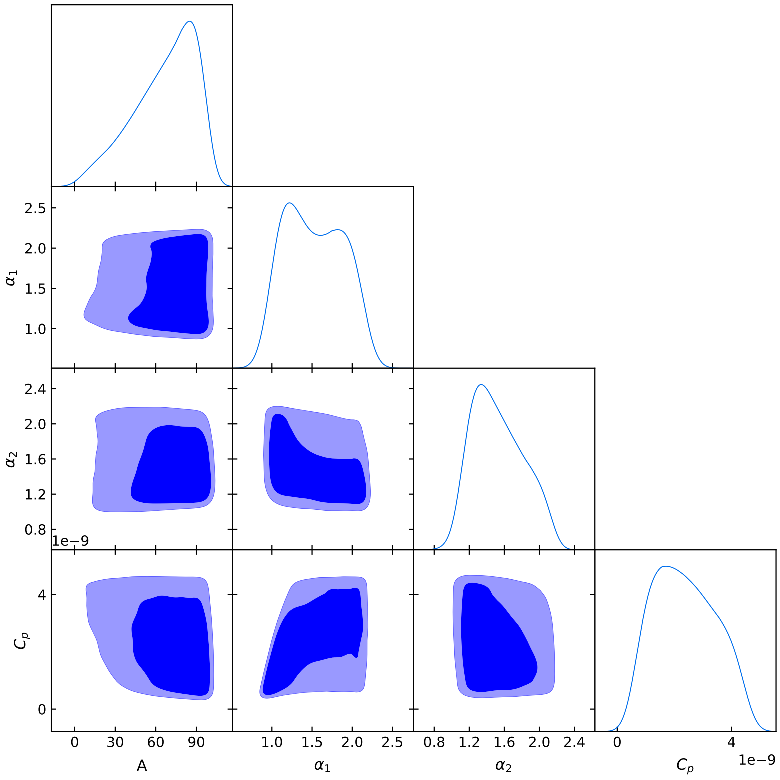

Figure 6.4: Triangular plot for the bounds on the AGN model with MCXCsub catalog. The dark blue and light blue refer to 68% and 95% confidence levels, respectively. The figure is taken from Ref. [175].

and with a spectrum close to the average one found for the γ-ray emission of BLZ in Ref. [176]. A spectral index lower than 2 is however indicative of a hardening of the unresolved population of BLZ. A result that agrees with findings of Ref. [177]. The model used in our analysis is normalized so that the integral of the window function over the redshift provides (approximately) the observed UGRB intensity if $A \simeq 1$. $A = 71.5^{+19.9}_{-29.9}$ is the value we found from MCMC, and we checked it is independent from the specific model of AGN or BLZ used in equation 6.19.

For any cosmological population, the 2h term is directly related to the total γ ray emission, since both essentially depend on the setting of the window function, while other ingredients (e.g., the bias) can only vary the 2h size in a limited way, due to cosmological constraints. Therefore, if the detected signal is due to the 2h term, the large value of the normalization factor would make the AGN contribution greatly exceeding the intensity of UGRB.

For what concerns the 1h term, there is instead an additional ingredient, that is poorly constrained, and can significantly change the strength of the correlation without affecting the window function (and thus the intensity), which is the relation between γ-ray luminosity and mass for clusters. Making this function steeply increasing with the cluster mass can boost the 1h term. The result we found might thus indicate that the model we implemented is able to effectively capture a large-scale contribution, but such correlation is not due to a 2h term involving γ-rays from AGNs (or other galactic sources) in two different halos at large physical distances. On the contrary, it might be regarded as a potential indication in favor of a diffuse emission from the ICM. Indeed, a relevant 1h term providing correlation on scales above *Fermi*-LAT PSF (i.e., around 0.5-1 degree) associated to γ-rays from the ICM can be obtained [111, 114], with no obvious violation of other existing bounds.

To clarify this conjecture, we divided the MCXCsub catalog into two subsets. We calculated the angular diameter $\theta_{500} = r_{500}/D_A(z)$[3] for each galaxy cluster, and then compared with the average $\bar{\theta}_{500}$ that we found to be $\bar{\theta}_{500} = 0.267$. There are 37 (72) clusters that larger (smaller) than this angle. If the measured signal is provided by the

---

[3] The diameter distance can be derived by luminosity distance: $D_A(z) = D_L(z)/(1+z)^2$.

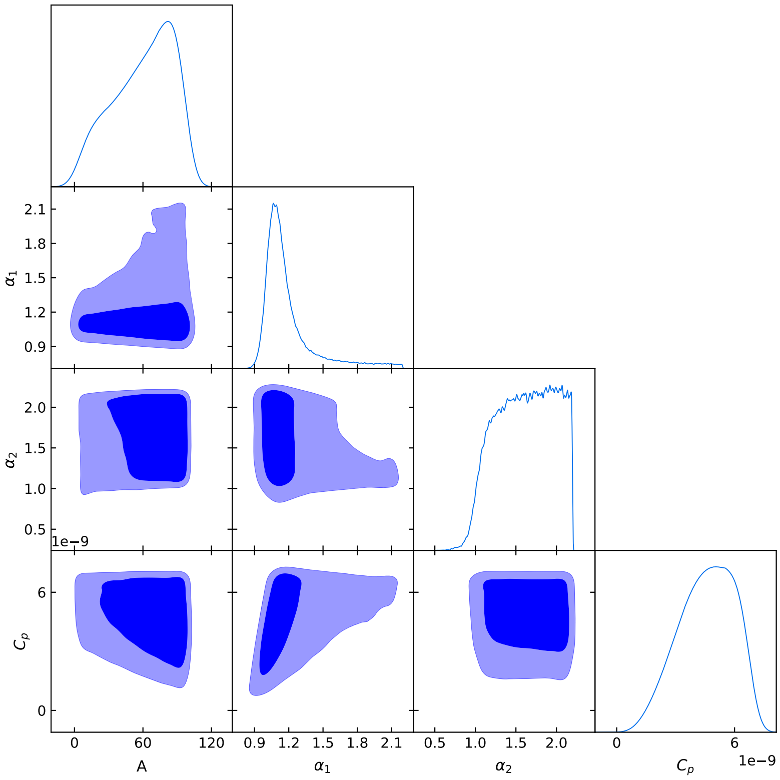

Figure 6.5: The same as in Fig. 6.4 but the clusters selected from $\theta_{500} > \bar{\theta}_{500}$. The figure is taken from Ref. [175].

ICM term, we would expect the sample including big clusters to provide the largest evidence in favor of a large scale emission. Let us note that, in most energy bins, the size of the clusters from the MCXCsub catalog is larger than the *Fermi*-LAT PSF. We perform the same MCMC fitting as above but on the sample with clusters larger than the average angle. Results in Fig. 6.5 shows $\Delta\chi^2_{\rm AGN-FLAT} = 2.1$, equivalent to 0.96σ.

Contrary to the expectations for an ICM signal, the statistical significance does not increase when only the largest clusters are considered: instead, it rather decreases as compared to the full MCXCsub sample. This significantly weakens a possible ICM interpretation, and leaves other alternatives open. The best-fit normalization of this case is similar to the one of the full MCXCsub, $A = 65.0^{+24.8}_{-35.7}$.

6.4.2 WIMP DM Results

In this Section, we use above results to constrain WIMP DM. We can write the physical CAPS model in the energy bin i as

$$\begin{aligned} C^{(C\gamma_i)}_{\ell,\mathrm{MODEL-DM}} = & \; N_{\mathrm{SN}}\, E_i^{-\alpha_{\mathrm{SN}}}\, \Delta E_i \\ & + N_{\mathrm{BLZ}}\, C^{\Delta E_i}_{\ell,\mathrm{BLZ}} + N_{\mathrm{mAGN}}\, C^{\Delta E_i}_{\ell,\mathrm{mAGN}} \\ & + N_{\mathrm{SFG}}\, C^{\Delta E_i}_{\ell,\mathrm{SFG}} + N_{\mathrm{DM}}\, C^{\Delta E_i}_{\ell,\mathrm{DM}}(M_{\mathrm{DM}}). \end{aligned} \tag{6.29}$$

We add $E_i^{-\alpha_{\mathrm{SN}}}\Delta E_i$ as the “shot-noise” (since it is not easy to precisely estimate it from the modeling). The contribution of DM in equation 6.29 is normalized with N_{DM}, which is defined as $\langle\sigma_{\mathrm{ann}} v\rangle / \langle\sigma_{\mathrm{ann}} v_0\rangle$, and $\langle\sigma_{\mathrm{ann}} v_0\rangle = 3 \times 10^{-26}\mathrm{cm}^3\mathrm{s}^{-1}$ is the cross-section mentioned in chapter 2.

In Fig. 6.6, we illustrate an example of the CAPS model, in the case of SDSSDR9 and energy bin $0.6 - 1.2$ GeV and considering DM mass of 200 GeV. Colorful solid lines are for different annihilation channels of DM, black lines refer to the astrophysical terms, and dotted lines are the shot-noise contributions. The obtained measurements are showed with brown points and error bars. As expected the shot-noise is important at very small angular scale (large ℓ) and it is dominated by astrophysical 2h contributions at large scales.

We also produce the angular 2P CCF in Fig. 6.7, which is the Legendre transformation of the CAPS. The color coding is the same as in Fig. 6.6.

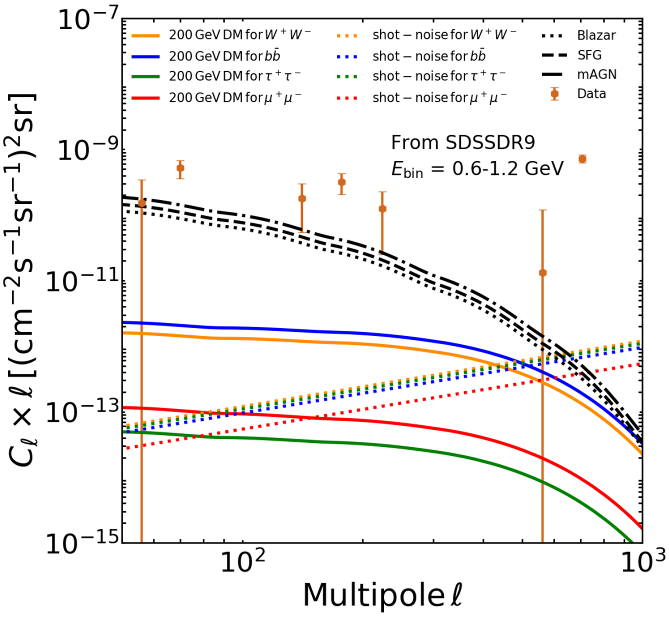

Figure 6.6: CAPS for the case of SDSSDR9 and energy bin from 0.6 to 1.2 GeV. For the DM model, we considered a mass of 200 GeV. Lines represent the different contributions to the model of equation 6.29. The solid lines are from the DM terms, with different annihilation channels showed with different colors. The corresponding colored dotted lines show the shot-noise terms, while astrophysical contributions are reported in black. The observed data are also shown in the plot together with their error bars. The figure is taken from Ref. [178].

Similarly to what we did in the previous Section, in order to compare the CAPS model with data, we define the χ^2 as:

$$\chi^2 = \sum_{i=1}^{N_{E_{\text{bin}}}} \sum_{\ell,\ell'} (C_\ell^{C\gamma_i} - C_{\ell,\text{MODEL}-\text{DM}}^{C\gamma_i}) \, (\Gamma_{\ell\ell'}^{C\gamma_i})^{-1} \, (C_{\ell'}^{C\gamma_i} - C_{\ell',\text{MODEL}-\text{DM}}^{C\gamma_i}) \, , \tag{6.30}$$

where $N_{E_{\text{bin}}}$ denotes the number of energy bins, ℓ and ℓ' show the minimum and maximum multipoles in Tab. 4.1, $C_\ell^{C\gamma_i}$ is the measured CAPS in the a energy bin, and $C_{\ell,\text{MODEL}-\text{DM}}^{C\gamma_i}$ is from theoretical prediction.

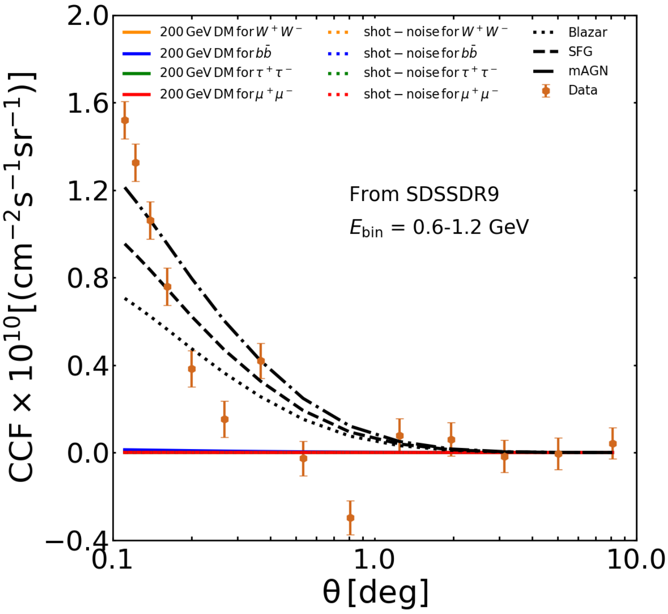

Figure 6.7: Angular 2P CCF for the case of SDSSDR9 and energy bin from 0.6 to 1.2 GeV. The DM and astrophysical models, and the color and style of lines is the same as in Fig. 6.6. The figure is taken from Ref. [178].

We use the MCMC algorithm to find the allowed regions on the 7 parameters ($N_{\rm SN}, \alpha_{\rm SN}, N_{\rm BLZ}, N_{\rm mAGN}, N_{\rm SFG}, N_{\rm DM}, M_{\rm DM}$) of the model. As an example of the data analysis, we show in Fig. 6.8 the triangle plot of the normalization parameters of DM and astrophysical sources for the case of the WHY18 catalog. The probability distributions shown are for a DM model annihilating into W^+W^- final state. Dark blue regions identify the 95% C.L. and light blue is for 68% C.L.. The dotted vertical lines in the marginal 1D distributions show the 68% C.L. upper limits.

From this figure we notice that all the posterior distributions tend to peak below one and slightly above zero. This is due to the degeneracy between the different astrophysical populations. A motivation for such behavior can be found by looking at the angular

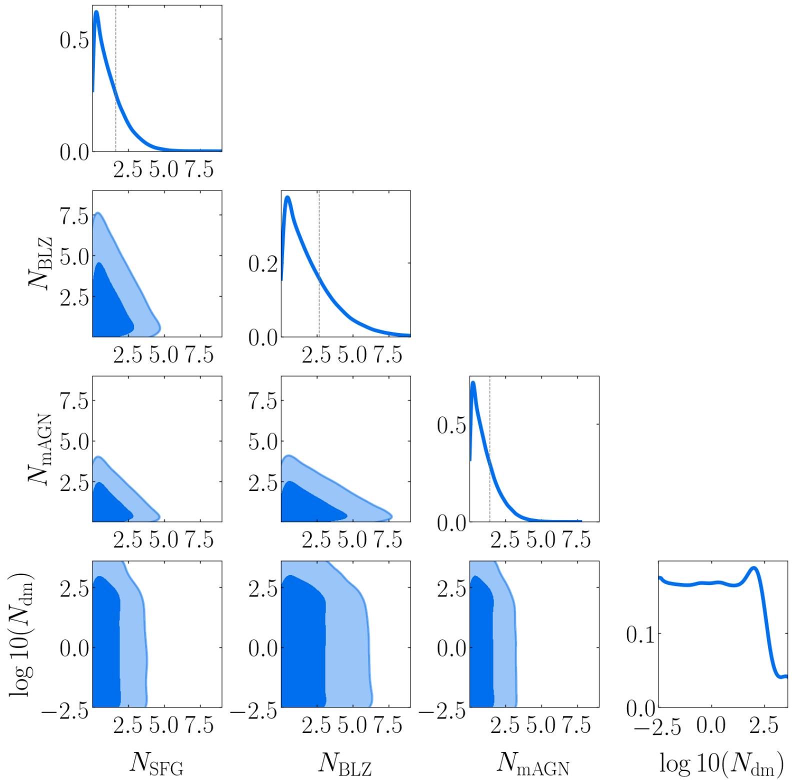

Figure 6.8: Triangle plot reporting the posterior distribution for the astrophysical DM normalized parameters of the cross-section in the case of the W^+W^- annihilation channel and from the WHY18 cluster catalog. The dark blue region and light blue region represent 95% and 68% C.L., respectively. The figure is taken from Ref. [178].

power spectrum shown in Fig. 6.6: it is clear that the 1h and 2h terms of the astrophysical components have similar shapes.

In Tab. 6.2 we report 68% C.L. upper limits for the normalization parameters of the astrophysical components in the various cases considered in the analysis.

Tab. 6.3 shows the χ^2 values of the best-fit models for the various catalogs and annihilation channels.

Table 6.2: Strongest upper limits on the normalization of the astrophysical components. First line reports the case of SFG, second line BLZ, and third line mAGN. In the first column, we indicate the catalog providing the most constraining bound. Using different DM channels does not make a sizable difference but nevertheless we report the most constraining case in brackets.

catalog	68% C.L. upper bounds	
WHY18($b\bar{b}$)	$N_{\rm SFG}$	1.6
WHY18($b\bar{b}$)	$N_{\rm BLZ}$	2.7
HIFLUGCS($\tau^+\tau^-$)	$N_{\rm mAGN}$	1.0

Table 6.3: χ^2 of the best-fit model for all catalogs and annihilation channels considered in this analysis. The number of degrees of freedom is 110 for all samples.

	$\chi^2(\tau^+\tau^-)$	$\chi^2(b\bar{b})$	$\chi^2(W^+W^-)$	$\chi^2(\mu^+\mu^-)$
WHY18	91.01	91.76	91.03	91.39
SDSSDR9	109.5	110.5	109.5	109.7
MCXCsub	137	137.1	139.2	137.8
HIFLUGCS	91.46	91.16	91.58	90.84

Finally, from the MCMC analysis, we build the 2D posterior distribution involving two DM parameters, by marginalizing the 7D distribution over the five astrophysical parameters. In Fig. 6.9, we show the 95% C.L. upper limits on the DM cross-section as a function of the DM mass for the four annihilation channels.

As mentioned before, we discuss also the impact of different substructure models. We show how the bounds on the DM cross-section change with the substructure model for the channel $b\bar{b}$ and in the case SDSSDR9 in Fig. 6.10: the red line represents the reference model [157], blue and green color represent lower [158] and higher [159] boost factors, respectively. As expected the constraints become more stringent when we consider highly concentrated substructures while they become less stringent in the opposite scenario.

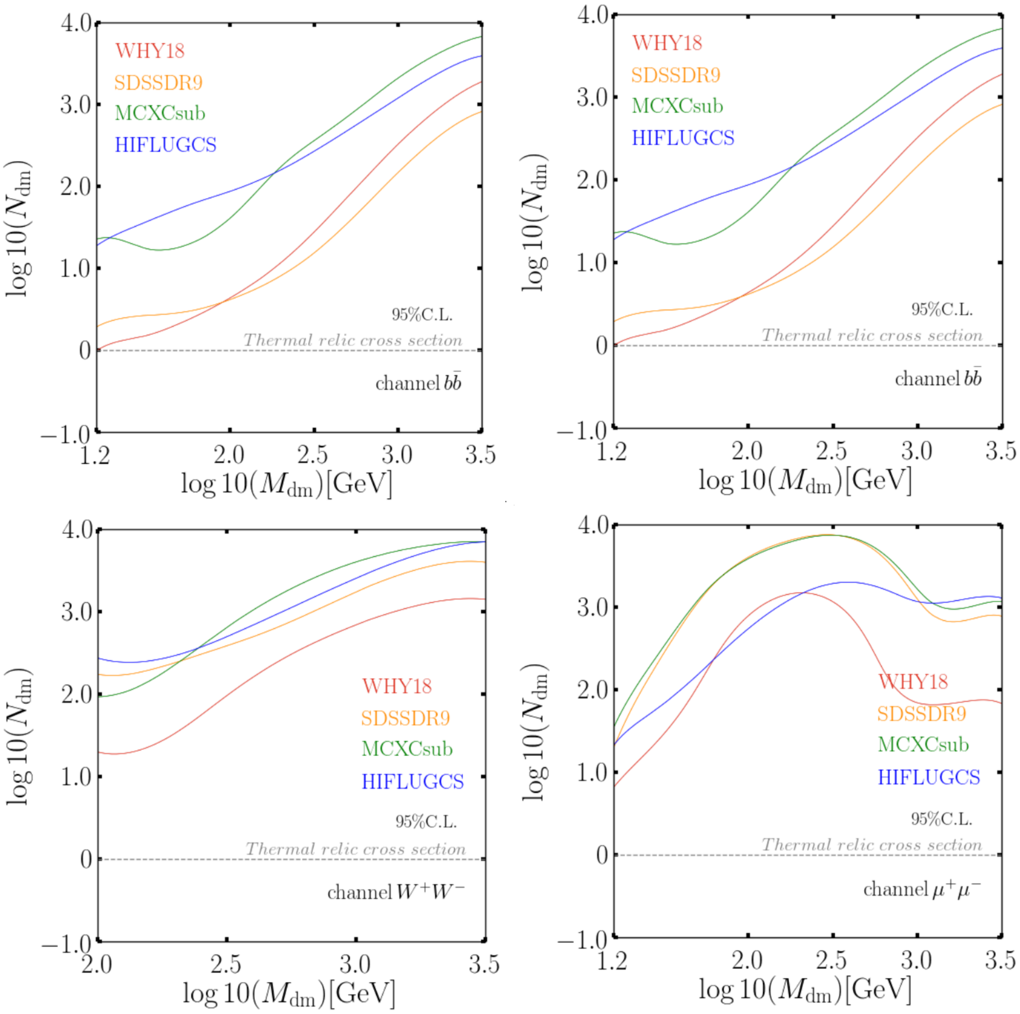

Figure 6.9: Upper bounds of 95% C.L. on the DM annihilation rate ratio $N_{\rm DM} = \langle\sigma v\rangle/\langle\sigma v\rangle_0$ as a function of the DM mass. Here we show in logarithm in order to be more intuitive. From left to right, and upper to bottom is $\tau^+\tau^-$, $b\bar{b}$, W^+W^- and $\mu^+\mu^-$, separately. The figure is taken from Ref. [178].

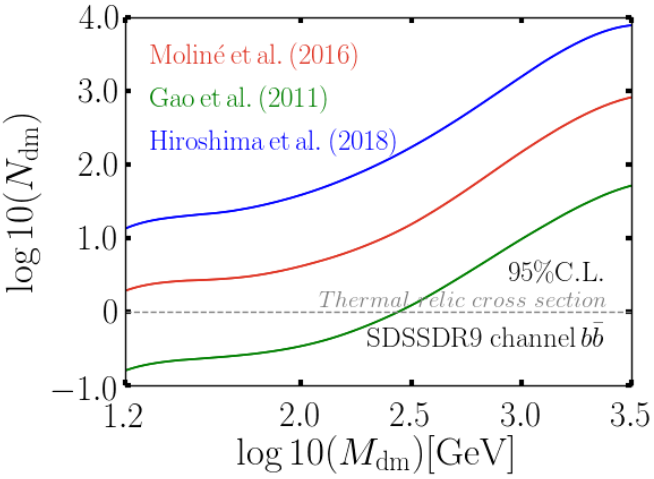

Figure 6.10: Upper bounds of 95% C.L. on the DM annihilation rate ratio $N_{\rm DM} = \langle\sigma v\rangle/\langle\sigma v\rangle_0$ in logarithm. Here we show three substructure models for conservative, higher and lower concentration of halo substructure models, they are from SDSSDR9 catalog and in $b\bar{b}$ channel. The figure is taken from Ref. [178].

6.5 Summary

In the work presented in this chapter, we have obtained the CAPS of the WIMP DM model and γ-ray astrophysical sources to interpret the correlation between the *Fermi*-LAT UGRB and the catalog of four galaxy clusters. Our main results and conclusions are summarized as following:

1. Astrophysical sources

   Due to the small volume $z < 0.2$ and the relative low number of objects in the catalogs considered in our analysis, only upper bounds can be derived for the contributions from γ-ray astrophysical sources, as appear to be clear from Fig. 6.8. As we have already stressed, there is a degeneracy between the different astrophys-

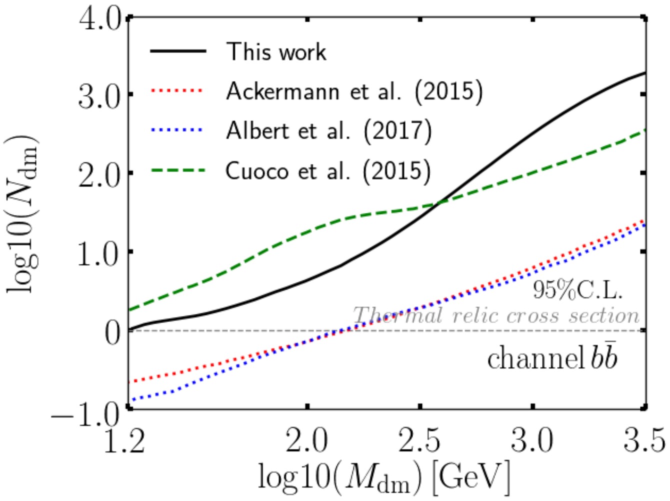

Figure 6.11: 95% upper bounds on the DM annihilation rate ratio $N_{DM} = \langle\sigma v\rangle/\langle\sigma v\rangle_0$ in logarithm as a function of the DM mass compared with other works. The dashed and dotted lines: green is taken from Ref. [133], red is from Ref. [179] and blue is given by Ref. [180]. Our work show in the black solid line, and it is the best constraints obtained from 100% branching ratio into $b\bar{b}$ annihilation channel. The line font is to discriminate the types of source: dotted lines refer to dSphs while dashed and solid lines are from galaxy cluster catalogs. The figure is taken from Ref. [178].

ical contributions. One possible way to reduce such degeneracy with future data is to having a more precise measurement of the energy dependence of the signal or to aim at deriving an accurate luminosity-mass relation to have a precise determination of the 1h term, which would allow us to set the relative amplitude of the 1h and 2h terms for a given population.

We found that BLZ are only weakly constrained ($N_{\mathrm{BLZ}} \leq 2.7$ at 68% C.L.) since their unresolved component is predominantly located at redshift higher than the ones considered here. More stringent bounds can be obtained for SFG ($N_{\mathrm{SFG}} \leq 1.6$ at 68% C.L.) and, in particular, for mAGN ($N_{\mathrm{mAGN}} \leq 1.0$ at 68% C.L.), which are believed to be the main contribution of the UGRB in the Local Universe [105].

2. DM - substructures

   The details of the adopted DM halo substructure scenario have a significant effect on the constraints of DM microscopic properties. With respect to our reference scenario, we found that the bounds can improve by about one order of magnitude a model with higher concentration, whilst to a relaxation of the bound by about one order of magnitude in the case of lower concentration, see Fig, 6.10.

3. DM - comparison among different catalogs

   From Fig. 6.9 one can notice that the most constraining catalogs for DM properties are WHY18 and SDSSDR9. This behavior can be explained considering that these catalogs have a larger number of objects (and thus statistics) than the X-ray catalogs, whilst, the latter one has a weaker signal (for more details see Ref. [175]).

4. DM - comparison among different channels

   At low DM masses, the dominant mechanisms of γ-ray production is through prompt emission occurring mostly via π^0-decay for the cases of $b\bar{b}$, $\tau^+\tau^-$ and W^+W^-, while through the final state radiation for $\mu^+\mu^-$. The latter case is the one that is less constrained below 100 GeV.

   At high energies, the inverse Compton of CMB photon with electrons and positrons generated by DM annihilation can provide a sizeable γ-ray contribution. The injection of electrons and positrons is enhanced in leptonic channels with respect to $b\bar{b}$ and W^+W^- channels and, for this reason, $\mu^+\mu^-$ is the most constraining final state at TeV energies (followed by the other leptonic channel, $\tau^+\tau^-$).

5. DM - comparison with previous works

   In this work, we obtain DM bounds comparable with those obtained with similar techniques (namely, through the study of the cross-correlation of γ-rays with LSS tracers) from Refs. [105, 132, 133]. Moreover, we employed a new approach to estimate the cross-correlation covariance matrix, i.e., using mocks for both the γ-ray and LSS contributions, which assures to have robust constraints. In Fig. 6.11, we show the comparison of the bounds on the DM cross-section, in the $b\bar{b}$ channel, with the work of Ref. [133]. We also include the constraints reported in Refs. [179, 180]: the bounds coming from dwarf spheroidal galaxies are often considered to be the most constraining and robust ones on WIMP annihilation arising from γ-rays. The constraints obtained in this work are about one order of magnitude weaker (for the conservative substructure scenario), but are derived from a completely independent technique.

CHAPTER 7

Constraining the Integrated Sachs-Wolfe Effect

Various kinds of cosmological observations, including type-Ia supernovae (SNIa) (e.g., observed by the Hubble Space Telescope [181–183]), BAO peak (e.g., in the distribution of SDSS luminous red galaxies [184, 185]), and study of weak gravitational lensing [186, 187] have indicated that the expansion of the Universe is accelerating.

The most common solution to this phenomenon is given by the introduction of a dark energy component, namely, by adding a component with a negative pressure term to the matter field in the Einstein field equation. The cosmological constant Λ in equations 2.3 and 2.4 has been introduced as the simplest physical term to provide a dark energy component. From current observational data, dark energy accounts for about $(68.47 \pm 0.73)\%$ [15] of the energy content of the Universe, i.e., dominates the composition of the Universe.

The CMB description can be considered as a milestone in the confirmation of the theoretical model of cosmology. On the other hand, many questions on the CMB are still open. They include CMB lensing effects and Sunyaev-Zel'dovich effects (SZ effects) [188], where both of them have the possibility to produce anisotropies in CMB photon temperature. The CMB anisotropy on large cosmological scales can be estimated by cross-correlating the ISW temperature fluctuation and the density of astrophysical objects. The first ISW detection was achieved by combining the measurement of High Energy Astronomy Observatory (HEAO) X-ray data and CMB anisotropies from Cosmic Background Explorer (COBE) [189, 190]. Afterwards, several similar analyses have been carried out using CMB data from the Wilkinson Microwave Anisotropy Probe (WMAP) satellite with a set of LSS data, which included the NRAO VLA Sky Survey (NVSS) radio galaxies [191], Micron All-Sky Survey galaxy (2MASS) [192–194], SDSS [195–197], the Wide-field Infrared Survey Explorer (WISE) [198, 199] and also X-ray background HEAO [200, 201]. Furthermore, some works [202–204] detected the ISW effect with very high significance by combining all these measurements together. Based on the Planck CMB data [205], different methods gave a significance of detection ranging from 2 to $\sim 4\sigma$ [206, 207].

This chapter discusses the analysis of the secondary CMB anisotropies related to ISW by cross-correlating *Fermi*-LAT data and Planck data.

7.1 Cross Correlation Signal of ISW Effect

The ISW effect is a secondary anisotropic effect in the CMB, which is caused by the change of the gravitational potential well between the local observer and the last scattering surface due to the expansion of the Universe, dominated by dark energy.

Photons move along geodesic, and the CMB radiation, propagating in the Universe from the last scattering surface to the observer, climb potential wells, in a way as dictated by general relativity. The energy of photons remains the same if the gravitational potential well is independent on time, e.g., in the matter domination era. This is because the energy gain for photons entering the well is compensated by the energy loss when they climb out the well. However, when dark energy or curvature plays a leading role, the energy losses and gains due to the gravitational potential well are different. This effect of gravitational redshift alters the frequency of photons. Fig. 7.1 shows such a process. If $\lambda_i = \lambda_{f1}$, the red-shift and blue shift cancel out with each other; but if the potential well changes over time, it leads the frequency of photons to become $\lambda_i > \lambda_{f2}$, and this is the ISW effect. An additional CMB anisotropy is generated in this case.

Therefore, the observation of late ISW can be a powerful way to detect dark energy and its evolution, and it can also be used to determine the equation of state of dark energy.

However, unfortunately, the most significant ISW signal is related to large-scale anisotropies and thus it is heavily affected by *Cosmic variance* [208], so it is challenging to extract ISW information directly from CMB observations. This problem can be solved using the cross correlation between the temperature fluctuations induced by ISW and

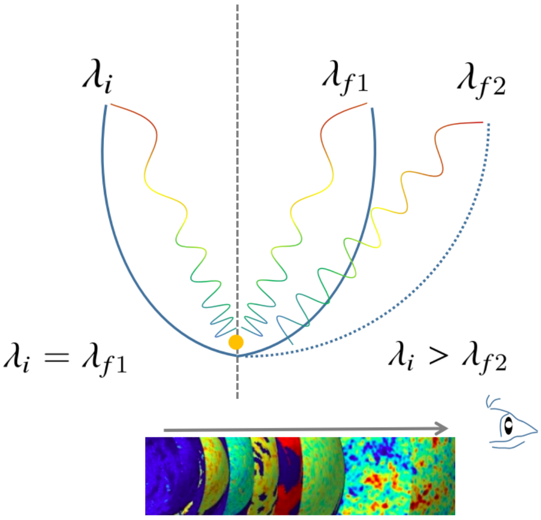

Figure 7.1: The schematic diagram of the ISW effect: photons go through gravitational wells from left to right and then are captured by the observer. If dark energy or curvature plays a leading role, the potential well changes and the photon wavelength goes from $\lambda_i = \lambda_{f1}$ to $\lambda_i > \lambda_{f2}$, which causes the ISW effect.

the density fluctuations of astrophysical sources such as galaxies [209].

The temperature perturbation of ISW caused by CMB photons along the LOS due to gravitational potential is

$$(\frac{\Delta T}{T})_{\mathrm{ISW}} = -2\int_{\eta'}^{\eta_0} \Phi'((\eta_0 - \eta)\hat{n}, \eta)\mathrm{d}\eta, \tag{7.1}$$

where T is the average temperature of today CMB photons, and η is time in comoving coordinate. η' and η_0 are representing the time at last scattering and today, respectively. $\hat{n}$ indicates the direction of LOS. Φ expresses a gravitational potential well, $\Phi' \equiv \mathrm{d}\Phi/\mathrm{d}\eta$.

The signal of ISW in real space is given by

$$\Psi(\hat{n}) = -2\int \frac{\mathrm{d}\Phi(\hat{n}D_c)}{\mathrm{d}D_c}\mathrm{d}D_c. \tag{7.2}$$

Here we ignore the optical depth factor $e^{-\tau}$, for the reason that correction is very tiny compared to the typical accuracy of the ISW effect itself and this will not affect our results. Within the event horizon, the gravitational potential is associated with the mass density disturbance in Fourier space $\delta = \delta\rho/\rho_0$, using the Poisson equation:

$$\Phi(k, z) = -\frac{3}{2c^2}\frac{\Omega_m(1+z)}{a(z)}\frac{H_0^2}{k^2}\delta(k, z). \tag{7.3}$$

As mentioned earlier, Ω_m is the matter density today, $\delta(k, z)$ is the Fourier transform of matter disturbance field, and the window function of CMB temperature field is

$$W_\ell^T(k) = \frac{3\Omega_m}{c^2}\frac{H_0^2}{k^2}T_{\text{CMB}}\int\frac{\mathrm{d}}{\mathrm{d}z}\left[\frac{G(z)}{az}\right]j_\ell(kD_c(z))\mathrm{d}z. \tag{7.4}$$

We consider the astrophysical sources which contribute to the *Fermi*-LAT data not to be very local and we set the maximum multipole to be 512. This implies that the linear theory can be adopted. The number density perturbation of unresolved sources $n_\gamma(\hat{D}_c, z)$ is related to the local disturbances of γ-ray luminosity density $\rho_\gamma(\hat{n}D_c, z)$, as follows:

$$\frac{\rho_\gamma(\hat{n}D_c, z) - \rho_\gamma(z)}{\rho_\gamma(z)} = \frac{n_\gamma(\hat{n}D_c, z) - n_\gamma(z)}{n_\gamma(z)}. \tag{7.5}$$

We define the local linear bias between number density and mass density $b_\gamma(z)$ as

$$\delta_{n_\gamma}(\hat{n}D_c, z) \equiv b_\gamma(z)\delta_m(\hat{n}D_c, z) = b_\gamma(z)\frac{\rho_m(\hat{n}D_c, z) - \rho_m(z)}{\rho_m(z)}. \tag{7.6}$$

Expressing the bias factor of γ rays as a function of redshift, we can write the window function of UGRB sources as

$$W_\ell^\gamma(k) = \int \rho_\gamma(z)b_\gamma(z)G(z)j_\ell(kD_c(z))\mathrm{d}z\ , \tag{7.7}$$

where $\rho_\gamma(z)$ is the (normalized) luminosity density. In the analysis of this chapter, we assume the astrophysical γ-ray emission from SFG to account for the UGRB. Since the statistical significance of the ISW effect in this work is almost independent from the selected theoretical model, we choose to use the bias parameters and normalized photometric density provided in Ref. [134].

As described in the previous section 5.4, the angular power spectrum between γ sky map and the CMB temperature anisotropy map can be written as:

$$C_\ell^{\gamma T} = \frac{2}{\pi} \int k^2 P(k) \left[W_\ell^\gamma(k)\right] \left[W_\ell^T(k)\right] \mathrm{d}k, \tag{7.8}$$

the superscript γ and T represent γ-ray and CMB temperature, respectively. We adopt the three-dimensional power spectrum described in the previous chapters, relying on the flat ΛCDM framework; for alternatives with non-zero curvature or gravitational modification, please refer to studies in Refs. [210, 211].

We adopt the Limber approximation, since we will consider relatively small scales $\ell > 10$. Finally, we can write the angular power spectrum by

$$\begin{aligned} C_\ell^{\gamma \mathrm{T}} = & \frac{3\Omega_m \mathrm{H}_0^2 T_{\mathrm{CMB}}}{c^3 \left(\ell + 0.5\right)^2} \int dz \rho_\gamma b_\gamma(z) H(z) G(z) \\ & \times \frac{d}{dz}\left(\frac{G(z)}{a(z)}\right) P\left(k = \frac{\ell + 0.5}{D_c(z)}\right) B(\ell). \end{aligned} \tag{7.9}$$

Here we include the correction of a Gaussian beam $B(\ell)$ with the beam size being $\Theta_{\mathrm{FWHM}} = 5'$. The observed power spectrum can have a different amplitude from the standard ΛCDM one. In order to quantify such difference, we define a free amplitude parameter A_{amp}

$$\hat{C}_\ell^{\gamma \mathrm{T}} = A_{\mathrm{amp}} C_\ell^{\gamma \mathrm{T}}, \tag{7.10}$$

where $\hat{C}_\ell$ and C_ℓ are the measured and theoretical cross correlation power spectrum, respectively.

7.2 Analysis of Results

We have calculated the power spectrum between two maps and used it to determine the signal intensity of the ISW effect, and the latest Planck data [15] are adopted here.

`PolSpice` offers the results and covariance matrix on measurement. Fig. 7.2 and Fig. 7.3 show the measured cross-correlation power spectra between Planck and *Fermi* maps in each energy bin. Besides these gray observed data points, provided by the `Polspice`, we also show the binned measurements with blue points for illustrated purpose. The error bars are taken from the diagonal term of the covariance matrix corresponding to each multipole. We have corrected the angular power spectrum by the beam window functions which are associated with PSF effects we mentioned in chapter 4. It is computed from *Fermi* tools `gtpsf` and varies with energy and specific IRFs, as the same consideration with [105]. However, since we only discuss the scales $\ell < 512$ and the main ISW information comes from even smaller ℓ, we found these effects are negligible.

First of all, calculation of the Gaussian likelihood function for the observed data theoretical cross-correlation power spectrum is

$$\mathcal{L} = (2\pi)^{-N/2} \left[\det(\Gamma_{ij})\right]^{-1/2} \exp\left[-\chi^2/2\right] , \tag{7.11}$$

where Γ_{ij} is covariance matrix, the index i of each χ^2 is

$$\chi^2(A_i) = \left[\hat{C}_{\ell,i} - A_i C_\ell\right]^T \Gamma_{ij}^{-1} \left[\hat{C}_{\ell,i} - A_i C_\ell\right] , \tag{7.12}$$

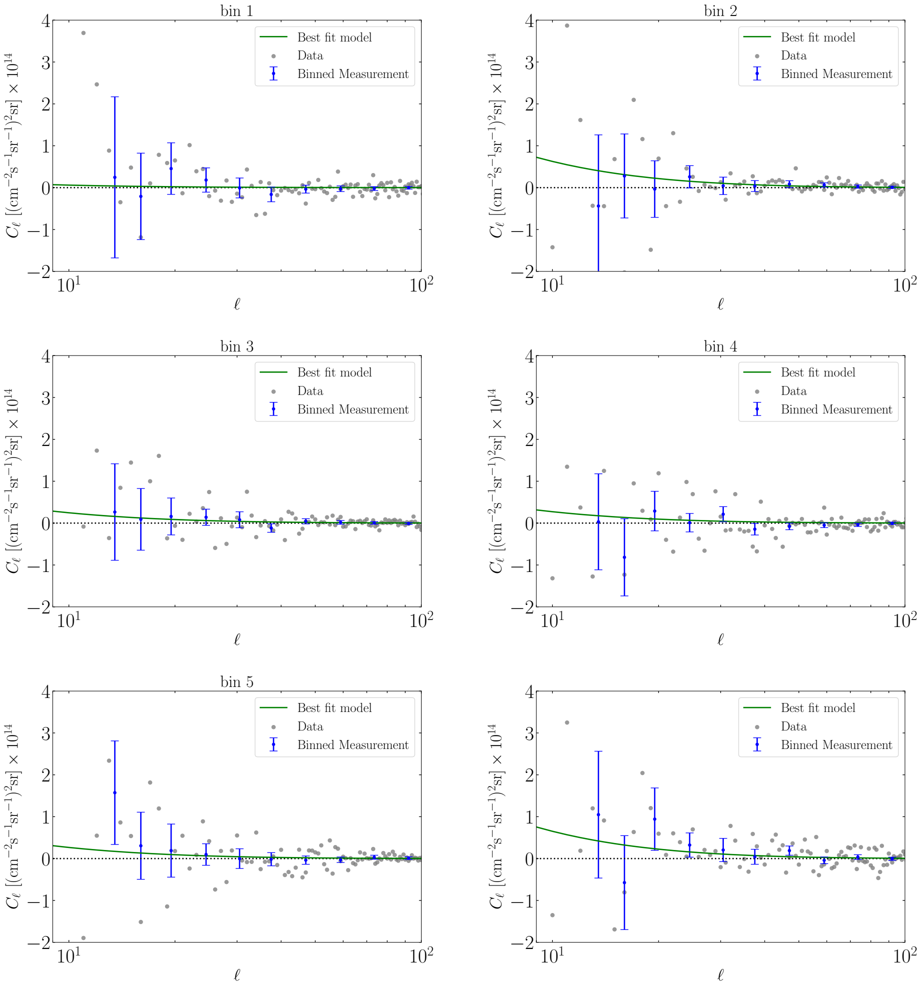

Figure 7.2: The cross-correlation results for the first six energy bins. The gray points in the figure are the original measured power spectrum, the one with the error bar is after rebinning, and the green one is the best fitting model in each energy bin. The figure is taken from Ref. [212].

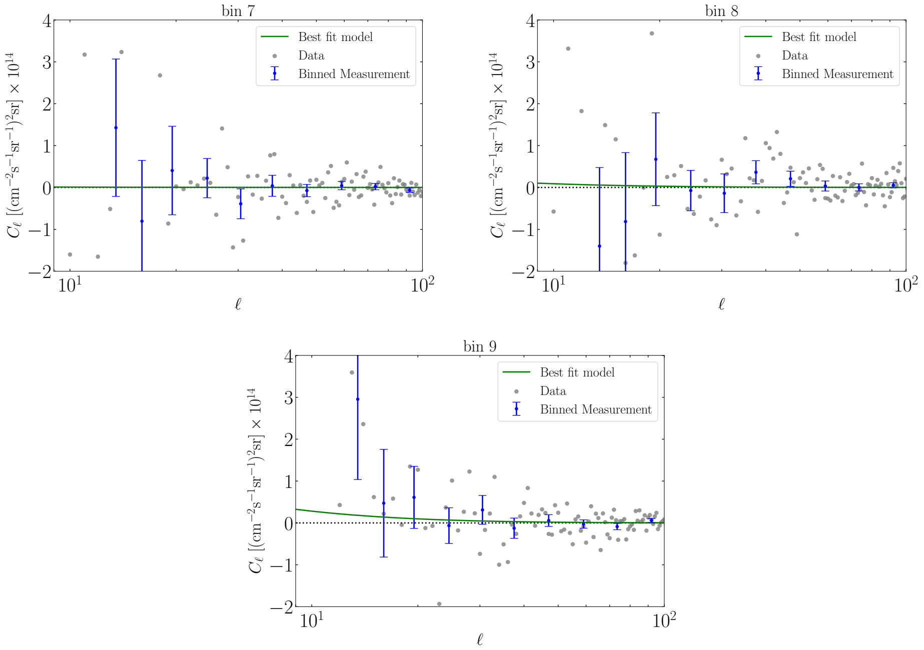

Figure 7.3: The cross-correlation results for the last three energy bins with the same legend as Fig. 7.2. The figure is taken from Ref. [212].

the A_i in the above equation is the amplitude parameter in the energy bin of index i mentioned earlier.

The range of multipole ℓ of CAPS is $\ell = 11 \sim 512$, here enumerates three reasons:

- the reason why ℓ starts with 11 is because the ISW effect mainly comes from large-scale regions, but it can be affected by the foreground of *Fermi* data according to chapter 4;
- When calculating the cross power spectrum, the adoption of Limber approximation will also lead to 10% level of uncertainty at small ℓ;
- Although there will not be any additional improvement to our analysis at the large

ℓ, we also choose to abandon them because of the influence of PSF correction. Especially when the beam window function starts deviating significantly. So the upper limit on ℓ is defined by the condition that the beam window function does not drop below a threshold corresponding approximately to the 68% containment of the PSF in the specific energy bin.

Finally, to quantify the significance of the measurement, we also use another statistic of test quantity

$$\mathrm{TS} = \chi_0^2 - \chi_{\mathrm{min}}^2, \tag{7.13}$$

where χ_{min}^2 is the minimum χ^2 calculated in equation (7.12), and χ_0^2 is the χ^2 with no ISW effect hypothesis, i.e. of the case $A_i = 0$. Under the null hypothesis, TS has a predominance that it can examine the χ^2 distribution with a number of degrees of freedom. We can derive the significance level of measurement based on the measured TS. In this case, we have only one free parameter here, the significance in σ is given by $\sqrt{\mathrm{TS}}$. In Tab. 7.1, we list the $\sqrt{\mathrm{TS}}$ results from different data combinations, another column with the results of SNR, which is $\mathrm{S/N} = A/\sigma_A$. From the value of every single bins, we can perceive that they are consistent with each other. We will use the values of SNR to represent the significance level in the following.

Among these nine energy bins, we found that only the second and sixth bins provide a significance level of around 1.8σ and 1.9σ significance of the ISW effect detection. While in the other seven energy bins, the measured cross-correlation power spectra show no signal comparing with null detection. If we look closer, in the second panel of Fig. 7.2, the data points in $30 < \ell < 40$ seems the main contribution to the 1.8σ ISW

Table 7.1: Results of the significance of the ISW effect for different data combinations. χ_0^2 and $\chi_{\rm min}^2$ are the χ^2 for no ISW effect hypothesis and the minimum for equation (7.12). Amplitude is the constraint result of A and σ_A, and $\sqrt{\rm TS}$ gives the significant for different bins.

Data	Amplitude	SNR/σ	χ_0^2	$\chi_{\rm min}^2$	$\sqrt{\rm TS}/\sigma$
bin1	0.28 ± 1.49	0.2	210.184	210.180	0.1
bin2	1.99 ± 1.09	1.8	182.88	180.04	1.8
bin3	0.74 ± 1.10	0.7	263.76	263.30	0.7
bin4	1.01 ± 1.22	0.9	293.01	292.32	0.9
bin5	0.72 ± 1.44	0.5	272.57	272.11	0.7
bin6	2.36 ± 1.22	1.9	269.11	265.76	1.8
bin7	0.49 ± 1.71	0.3	276.08	275.97	0.3
bin8	0.78 ± 1.84	0.4	300.48	300.15	0.6
bin9	1.34 ± 1.59	0.8	330.01	328.79	1.1
all (binning)	0.95 ± 0.53	1.8	2398.07	2395.16	1.7
all (unbinning)	0.64 ± 1.83	0.4	202.42	202.24	0.4

detection. Moreover, even if we neglect the low multipole information ($\ell < 21$ and $\ell < 31$), there are still 1.7σ and 1.4σ significance of the ISW effect appearing, respectively. However, the situation will be different in the sixth energy bin. When we also discard the data from large scales, the significance of the ISW effect will quickly drop down to 1.2σ and 0.4σ, respectively, which indicates the main signal comes from the larger scales.

Since we compute the cross-correlation signal in nine energy bins for this work, for the relationship between them, we can use a single power-law model, which includes an explicit energy dependence, to normalize the amplitudes:

$$\bar{C}_\ell^i = C_\ell^i \frac{(E_{\rm min}^i E_{\rm max}^i)^{-\alpha_0}}{\Delta E^i} \,, \tag{7.14}$$

where $E_{\rm min}^i$ and $E_{\rm max}^i$ are the minimal and maximal energy in each bin which are listed in Tab. 4.1, $\Delta E = E_{\rm max} - E_{\rm min}$ is the width of the energy bin considered in the cross-correlation analysis, and α is the slope. Ref. [177] used the angular correlation power spectrum of *Fermi*-LAT UGRB map to constrain the slope of the single power law model and obtained the tight limit $\alpha = 0.13 \pm 0.03$ (68% C.L.), and corresponds to α_0 in equation 7.14: $\alpha_0 = \alpha + 1$.

Here, we use the same *Fermi*-LAT UGRB data with slightly different energy separation, which should not significantly change the constraint. We also try to use our ISW measurements in nine energy bins to constrain this slope, due to the strong degeneracy between the slope and the amplitude, the limited accuracy of data points, we can not obtain any reasonable constraint from the current ISW measurements. Therefore, here we directly fix the slope to be the best fit value $\alpha_0 = 1.13$ and only focus on the constraint of the amplitude.

By combining ISW measurements of the nine energy bins, we can constrain the amplitude parameter:

$$A_{\rm amp} = 0.95 \pm 0.53 \ \ (68\% \ {\rm C.L.}) \ . \tag{7.15}$$

When analyzing separately, the significances from single second or sixth energy bin are slightly larger than 1.8σ. We find the reason comes from the single power-law model after some careful checks. In this model, we normalize all the amplitudes of energy bins to one single parameter. So the normalized amplitude parameter was suppressed by other components with a non-detection result, which causes underestimation of the theoretical predictions in the second and sixth energy bin. In the meanwhile, the error bars of data points in these two bins still remain the same value. The final significance of ISW detection has dropped down to $\sqrt{\mathrm{TS}} \sim 1.3\sigma$. If only take data points from the second and sixth bins to measure the amplitude parameter, it would be improved to 2.7σ detection of the ISW effect to get $A_{\mathrm{amp}} = 2.59 \pm 0.95$ at 68% confidence level.

Furthermore, we combine all the UGRB information into one single energy bin, which is basically one map of the full energy band, to measure the cross-correlation power spectrum between Planck and *Fermi*-LAT UGRB maps. Different from the binning results above, using one energy bin will significantly lose all of the LSS information and only give very weak significance, about 0.3σ confidence level.

7.3 Hypothesis Testing

For the sake of validation by summing energy bins together when estimate all bins χ^2 in Tab. 7.1, we implement a correlation coefficient to describe the covariance between different energy bins. This Gaussian estimator is determined by equation A.7 and 6.26 in section 6.3, The quantity f_{sky} in equation A.7 is the coverage percentage of CMB map over full sky map.

With fixed multipole, the r_E illustrates the off-diagonal elements of the covariance between γ-ray maps and CMB map.

There are four arbitrary energy slices among 9 bins of cross-correlation coefficient r_E in Fig. 7.4. For instance, the left-top one gives the result of the first bin with the other 9 bins. Those peaks are from the diagonal of covariance which equals 1 by definition. The results of other points illustrate by off-diagonal terms. They show the off-diagonal elements of the covariance matrix in high multipole are mainly below 10% deviation,

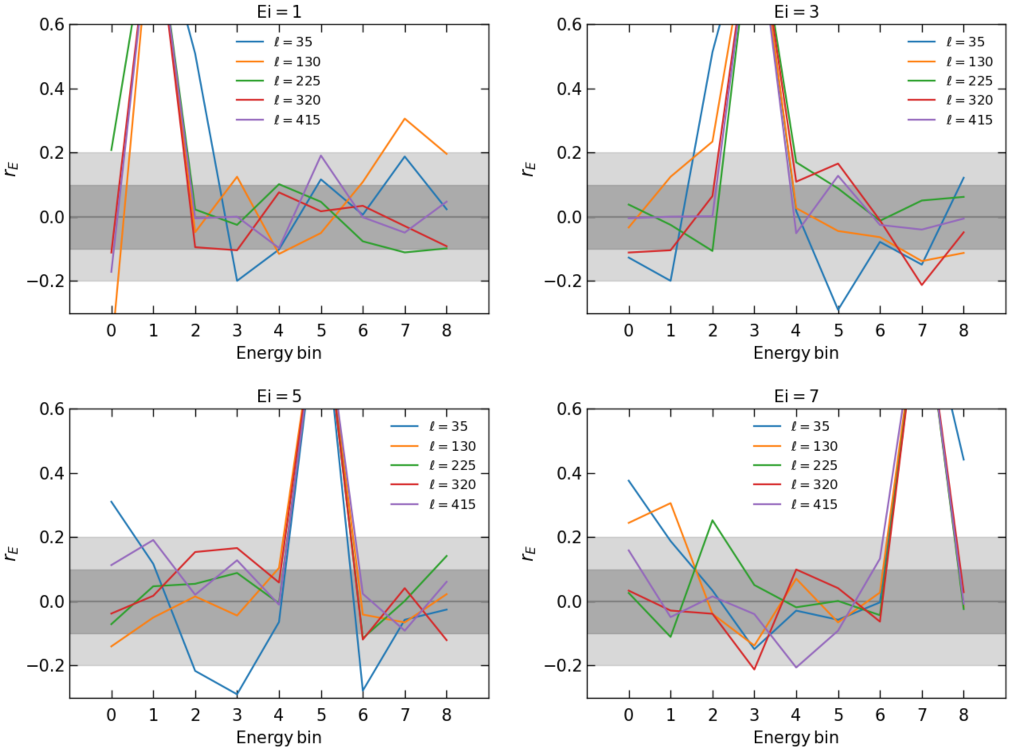

Figure 7.4: Four energy slices of the cross-correlation coefficient as defined by equation 6.26. The title of E_i refers to index i or j energy bin of $r_E^{i,j}$, the other one represents on the horizontal scale of each panel. Each colored line stands different multipole in our analysis range. The peaks are diagonal covariance that namely, $r_E^{i,i}$, which equals to 1 by definition. Therefore other points are off-diagonal terms of the covariance matrix. The figure is taken from Ref. [212].

which means the independence between them. Despite the correlation are a little higher at low ℓ than other places, which means the different energy bin maps contribute to the ISW signal in a similar way. it allows us to sum them up for analysis because of most of the values are under 10% deviation.

To check the robustness of the results, we performed further tests using mock catalogs with no cross-correlation with the CMB temperature fluctuations, verifying that the computed cross-correlation power spectra are compatible with a null signal.

In each energy bin, we create a Monte Carlo catalog that redistributed the galaxies of the catalog randomly over the sky area and remains the same total flux with the original map. In this case, the new catalog should not contain any intrinsic clustering. Following the procedures above, we use these random mock catalog to cross-correlate with the Planck map and measure the normalized amplitude parameter. As we expected, the obtained significance is very close to zero, $\mathrm{S/N} < 0.1\sigma$. The clustering feature disappears when using the random mock catalog.

Furthermore, we vary the galactic cut from $20°$ to $40°$ in order to ascertain the robustness from the range of galactic mask. We computed the residuals of real *Fermi* maps using different galactic cut on the mask in all energy bins and measured the cross-correlation power spectra with the Planck map to estimate the significance of ISW detection.

In Tab. 7.2, we list the obtained significances using different galactic cuts on the mask. As we expected, the highest significance comes from the *Fermi* map with the galactic cut $|b| < 30°$, which is consistent with our previous result [203]. When we increase the galactic cut area, the UGRB information will be substantially lost, e.g., the area size of the *Fermi* map with the $|b| < 40°$ cut is only half of that of the map with $|b| < 20°$ cut. Therefore, the obtained error bar of the normalized amplitude parameter turns to larger than before. Consequently, the values of SNR go in the opposite direction, become lower. On the contrary, when decreasing the galactic cut area, the galactic contamination will be strong and the systematic errors could affect the significance.

Table 7.2: Results of the significance of ISW detection using different galactic cuts.

Samples	Amplitude	SNR	$\sqrt{\mathrm{TS}}$
$\|b\| < 20°$	0.49 ± 0.51	1.0	1.0
$\|b\| < 25°$	0.81 ± 0.49	1.7	1.6
$\|b\| < 30°$	0.95 ± 0.53	1.8	1.8
$\|b\| < 35°$	0.63 ± 0.65	1.0	0.9
$\|b\| < 40°$	0.34 ± 0.79	0.4	0.4

7.4 Summary

In this chapter, we used the UGRB data in the energy range [0.631, 1000] GeV from the latest *Fermi*-LAT γ-ray observations to estimate the cross-correlation power spectra with the Planck CMB map, in order to investigate its capability for detecting the well-known ISW effect. Following the procedure of foreground cleaning as in Ref. [134, 136, 177], for the first time, we obtained positive evidence at about 1.8σ significance for the ISW detection.

Here we summarize the main conclusions in more details:

1. We reported the positive evidence at about 1.8σ confidence level from the cross-correlation power spectra of *Fermi* γ-ray maps and Planck CMB map in the energy range [1.202, 2.290] GeV and [17.38, 36.31] GeV. When combining these two energy bins together, there is a 2.7σ evidence of the ISW effect for $A_{\mathrm{amp}} = 2.59 \pm 0.95$ (68% C.L.).

2. We use the single power-law model to normalize the amplitude in each energy bin and estimate the normalized amplitude parameter from all nine energy bins

together. The significance of the ISW effect is at about 1.8σ confidence level, with $A_{\rm amp} = 0.95 \pm 0.53$. When comparing with the result of Ref. [203], we found the main improvement comes from the updated *Fermi*-LAT data.

3. Furthermore, we implemented a null hypothesis to test the cross-correlation between CMB and the UGRB by randomizing the *Fermi* maps of the nine energy bins. These randomized mock maps contain no intrinsic clustering. We found a significance compatible with zero. This null test confirms real nature of the above signal.

4. Finally, we generated several mask maps with different galactic cuts to check the influence of these galactic cuts on the obtained significance of the ISW effect. Similar to our previous work, we found the galactic cut at $|b| < 30^\circ$ gives the highest SNR.

CHAPTER 8

Conclusions and Outlook

Thanks to the accurate observational data provided in recent years by the *Fermi*-LAT telescope, researches on cosmology at γ-ray frequencies can be conducted successfully. This has been the subject of the present thesis. On one side, we have processed *Fermi*-LAT γ-ray data, generated photon count and exposure sky maps and masks, and obtained images of the unresolved extragalactic γ-ray background. This required also to carry out the energy binning and resolution calibration. In addition, we collected multiple-band information on galaxy cluster catalogs, computed the mass M_{500} for every clusters, determined the overlap among catalogs, implemented sample screening, and then selected the low-redshift and massive clusters which are the most promising LSS tracers to detect the γ-ray emission from clusters. As for the case of γ-rays we created the sky maps and masks for the cluster catalogs. Similarly we processed the Planck CMB temperature anisotropy to use the ISW as LSS tracers.

Then, we derived and computed the correlation function both for what concerns the theoretical modeling and the observational measurements. Besides, we improved the treatment of the covariance matrix for this analysis and applied different robustness checks for our works.

The major outcomes are summarized in the following:

- For all the four cluster catalogs considered, we confirmed that the unresolved γ-ray emission observed by *Fermi*-LAT is correlated with LSS. We found that the largest significance for the correlation signal between catalog and *Fermi*-LAT data occurs for the galaxy clusters identified in the X-ray band, i.e. MCXCsub and HIFLUGCS, for which the SNR is 3.5 and 3.2, respectively. Concerning the scale of the correlation, we found that the MCXCsub catalog exhibits a preference for a large scale contribution (whilst no clear indication can be derived for the other catalogs). The determination of its origin requires further investigation since both a 1h term given by large-scale emission from the intra-cluster medium and a 2h term from the AGN distribution cannot explain the signal in a completely satisfactory way. Our analysis is in agreement with the hint found in [213].

- We tested different procedures to derive the multi-dimensional covariance matrix, which is a key factor in the study of cross-correlation signals. We started from mock maps and, later, we developed a semi-analytical framework that allows the two covariance matrices (one for the catalog and one for the γ-ray data) to be properly combined without overestimating the error. A rigorous prescription is clearly important for estimating the existence of signals and inferring the significance of model parameters. The techniques we developed can be used also in other similar statistical analysis of correlation between LSS and γ-rays.

- Through the analysis of the CAPS involving galaxy clusters at low-redshift $0 < z < 0.2$ and with large mass $M_{500} > 10^{13} M_{\odot}$, we have ruled out the thermal cross-section for WIMP DM at masses below 20 GeV for channel $\tau^+\tau^-$ and 15 GeV for channel $b\bar{b}$.

- The correlation function between the UGRB and CMB temperature anisotropic map shows a positive signal at 1.8σ confidence in the energy bin of [1.202, 2.290] GeV and [17.38, 36.31] GeV; it raises to 2.7σ when joining these two energy bins. We used a single power law model to normalize the amplitude of the signal in each energy bins and estimated the normalization parameters from all energy bins. For the first time a correlation with ISW is obtained with amplitude $A_{\rm amp} = 0.95 \pm 0.53$ and 1.8σ confidence of detection (combining all energy bins) . Our results are compatible with a previous analysis of the *Fermi*-LAT data and ISW [131], and update it adding hints of detection.

These studies were inspired by the goal of obtaining a clear comprehension of the constituents of the UGRB through correlation analyses. At present, there is still a significant degeneracy between the signals from different astrophysical sources and DM. The characterization of the observed γ-ray sky is an important open issue in today's astrophysics that future researches have to tackle. Clearly, better results crucially depend also on the possibility of obtaining high-quality and precise data. A more profound understanding of the specific UGRB-related issues discussed in this thesis might help to describe more accurately and vividly big open problems in cosmology and particle physics.

APPENDIX A

Covariance from Mocks

In order to determine the existence and confidence of signals, we need an accurate way to calculate the covariance matrix to create a robust likelihood function for model constraint. Therefore, we compared and evaluated the different solutions to select the best one. After extensive and detailed studies on the measurement of the CAPS between the galaxy clusters catalogs and the UGRB, we found that the Gaussian approximation, which means to reduce the matrix to its diagonal elements both in energy and multipole, works fairly well. This is particularly true after binning data. Nevertheless, in the analysis we have retained the full covariance, for what concerns the multipole dimension. Although we have retained the covariance with the entire multipole range in the analysis, the error estimate of this type of CAPS can be approximated by Gaussian estimation. At the same time, we derive a general method that I describe in the following. The method we started with to obtain the CAPS covariance matrix is based on `Polspice`, which on the other hand, adopts a non-minimum variance algorithm.

Therefore, we investigated methods based on the production of mock realizations of two kinds of maps, from which we derived the estimation of the CAPS covariances. Our design starts from the real map, and generates mocks from it, in a very versatile way. Since there are two observables in the CAPS, we have to generate N maps for each observable. It means there are $N \times N$ crossing cases, and it makes the calculation of covariance very demanding because N should be very large to make all the process reliable. Thus we designed, tested and verified a method that allows computing resources to increase linearly with N rather than quadratically.

Here we list five scenarios for generating mock maps:

A.1 Bootstrap

A map in `Healpix` format is an array of pixels where each element represents the intensity of the specific pixel. To make one bootstrap realization we follow these steps:

- We divided the full array in $N_{\rm sub}$ sub-arrays, so that each of them has $N_{\rm pix}/N_{\rm sub}$ pixels;
- We label each of the sub-array;
- We randomly pick $N_{\rm sub}$ sub-arrays with replacements and form a new resampled `Healpix` map.

Reiterating these three steps would produce N_r bootstrap realizations. The new `Healpix` map originated in this way is characterized by the same number of pixels of the original data set, but each of the sub-array can be selected more than one times or not selected at all; for this reason we have to weight each sub-array by the number of times it is selected. This procedures is called bootstrap with replacements [214].

In this case the estimator of the APS covariance matrix is given by:

$$\widehat{\Gamma_{\mathrm{B}}} = \frac{1}{N_r - 1} \sum_{k=1}^{N_r} (x_i^k - \bar{x}_i)(x_j^k - \bar{x}_j)\,, \tag{A.1}$$

where x_i is the i-th bootstrap realization and N_r is the number of realizations and,

$$\bar{x}_i = \frac{1}{N_r} \sum_{k=1}^{N_r} x_i^k\,. \tag{A.2}$$

A.2 Jackknife

As for the bootstrap technique, also for the jackknife method the map is divided in N_{sub} sub-arrays with the same number of pixels. Each of the sub-arrays is labeled, but in this case a realization is obtained by systematically omitting one of the sub-array in each realization. The resampling of the data-set consists of $N_{\mathrm{sub}} - 1$ remaining sub-arrays with volume $(N_{\mathrm{sub}} - 1)/N_{\mathrm{sub}}$ times the volume of the original data-set [214]. By definition there are only $N_r = N_{\mathrm{sub}}$ different copies of the data set that are created in this way. In this case the APS covariance matrix estimator reads:

$$\widehat{\Gamma_{\mathrm{J}}} = \frac{N_r - 1}{N_r} \sum_{k=1}^{N_r} (x_i^k - \bar{x}_i)(x_j^k - \bar{x}_j)\,, \tag{A.3}$$

where $\bar{x}_i$ is given by equation A.2. The factor $(N_r - 1)$ accounts for the lack of independence between the N_r copies of the data set.

A.3 Phase Randomization

The implementation of this procedure is described in [215]. It based on the fact that it is always possible to write an intensity map as a linear combination of spherical harmonics:

$$f(\theta, \phi) = \sum_{\ell=0}^{\infty} \sum_{m=-\ell}^{\ell} a_{\ell m} \, Y_{\ell m}(\theta, \phi) \, . \tag{A.4}$$

from which the angular power spectrum is obtained:

$$C_\ell = \frac{1}{2\ell + 1} \sum_{m=-1}^{\ell} |a_{\ell m}|^2 \, . \tag{A.5}$$

It is clear that equation A.5 is invariant under a phase rotation on the harmonic amplitudes $a_{\ell m}$:

$$a_{\ell m} \quad \longrightarrow \quad a_{\ell m} e^{i \varphi_{\ell m}} \qquad \varphi_{\ell m} \in \mathbb{R} \, ; \tag{A.6}$$

Taking advantage of this symmetry, we can build independent realizations of the initial intensity map, each sharing the same APS. Since we determine the true-map APS from a masked sky, we need to correct for it, in order to produce a mock map that contains the correct statistical properties of the original map. The procedure we adopt is:

- Measure the auto APS ($C_\ell^{\gamma\gamma}$ or C_ℓ^{CC} for γ rays or galaxies/clusters) from the masked data maps;
- Transform: $a_{\ell m} \longrightarrow \tilde{a}_{\ell m} = a_{\ell m} e^{i \varphi_{\ell m}}$;
- Construct a full-sky mock map: $\tilde{f}(\theta, \phi) = \sum_{\ell=0}^{\infty} \sum_{m=-\ell}^{\ell} \tilde{a}_{\ell m} \, Y_{\ell m}(\theta, \phi)$;
- Correct the mock map for incomplete sky: $\tilde{f}(\theta, \phi) \longrightarrow \tilde{f}(\theta, \phi) \times W(\theta, \phi) \times f_{\text{sky}}^{-1/2}$.

The $(f_{\rm sky})^{-1/2}$ accounts for the fact that the original map was masked and therefore the obtained harmonic amplitudes has reduced power as compared to the true one. $W(\theta,\phi)$ restores the mask on the mock map. Let us notice that this method looses information on the shot-noise, and therefore it can produce underestimate of the covariance in situations where the shot-noise is large.

The evaluation of the APS covariance matrix is finally done with equation A.3.

A.4 Gaussian Realizations (Synfast)

`Synfast`[1] is a `Healpix` routine that allows to generate realizations of a Gaussian random fields on a sphere, starting from an input APS. The procedure We therefore start from the APS describing the statistical distribution of the data sample we want to replicate:

- Measure the auto APS ($C_\ell^{\gamma\gamma}$ or C_ℓ^{CC} for γ rays or galaxies/clusters) from the masked data maps;
- The obtained APS is fed to `Synfast`, which outputs a full-sky mock map: $\tilde{f}(\theta,\phi)$;
- Mask the mock map: $\tilde{f}(\theta,\phi) \longrightarrow \tilde{f}(\theta,\phi)\ \times W(\theta,\phi)$.

The evaluation of the APS covariance matrix is finally done with equation A.3.

---

[1] https://healpix.jpl.nasa.gov/html/facilitiesnode14.htm

A.5 Log-normal Realizations (FLASK)

Flask[2] is a C++ code, parallelized with OpenMP, based on the work of [216] and created to generate mock realizations of galaxy distributions starting from their 3D power spectrum. Like `Synfast`, it generates multiple correlated fields on spherical shells, after providing the power spectrum describing the distribution to be replicated. Differently from `Synfast`, the generated maps are obtained from a log-normal distribution. The tomographic approach used by Flask slices the three dimensional space into spherical shells (redshift slices), each one discretized in `Healpix` maps. After generating the fields, Flask can apply selection functions and noise to them. The output can be in the form of a source catalog and/or `Healpix` maps, among others.

We use Flask to generate N_r independent realizations. The evaluation of the APS covariance matrix is finally done with equation A.3. Although the code is thought to work for galaxy distributions in different redshift bins, we tried to use it also for γ ray maps, by using the APS instead of the 3D power spectrum.

A.6 Covariance Estimators' Relations

As we have shown in the previous sections, we can set a different APS covariance matrix estimator for each of the methods we use to produce mocks. It can be useful to have a look to the relation between the different estimators.

Given a data vector $\boldsymbol{X} = \{x_1, x_2, ..., x_{N_r}\}$ we can write the generic expression for

---

[2] http://www.astro.iag.usp.br/ flask

the covariance matrix of $\boldsymbol{X}$ as:

$$\text{cov}[\boldsymbol{X}] = \frac{1}{N_r} \sum_{k=1}^{N_r} (x_i^k - \bar{x}_i)(x_j^k - \bar{x}_j)\,, \tag{A.7}$$

with $\bar{x}_i$ is given by equation A.2. Equation A.7 can also be rewritten as:

$$\text{cov}[\boldsymbol{X}] = \frac{1}{N_r} \sum_{k=1}^{N_r} x_i^k x_j^k - \frac{1}{N_r^2} \sum_{k=1}^{N_r} x_i^k \sum_{k=1}^{N_r} x_j^k\,. \tag{A.8}$$

The unbiased definition of the sample covariance when the mean is derived from the sample itself is:

$$\begin{aligned} \widehat{\Gamma}_{\text{U}} &\equiv \frac{N_r}{N_r - 1} \times \text{cov}[\boldsymbol{X}] \\ &= \frac{1}{N_r - 1} \sum_{k=1}^{N_r} x_i^k x_j^k - \frac{1}{N_r} \frac{1}{N_r - 1} \sum_{k=1}^{N_r} x_i^k \sum_{k=1}^{N_r} x_j^k\,. \end{aligned} \tag{A.9}$$

We can relate the estimator of equation A.9 to the ones obtained with the jackknife A.3 and bootstrap A.1 techniques as:

$$\begin{aligned} \text{Jackknife:} \quad \widehat{\Gamma}_{\text{J}} &= \frac{(N_r - 1)^2}{N_r} \times \widehat{\Gamma}_{\text{U}}; \\ \text{Bootstrap:} \quad \widehat{\Gamma}_{\text{J}} &= \widehat{\Gamma_{\text{U}}}. \end{aligned} \tag{A.10}$$

Appendix B

Semi-analytic Prediction of the Cross-Correlation Covariance

The derivation of the covariance matrix of the CAPS requires a combinations of information from many different sky maps. As mentioned in appendix A, in order to obtain stable results, we need a large number of realizations and moreover we have to consider several energy bins and redshift bins. So here we show a faithful estimate of the complete covariance matrix by a simpler combination, which involves (1) the real measurement γ-ray sky maps and catalogs mocks; (2) the real measurement catalogs and γ-ray sky maps mocks. This can reduce the number of calculations from $(N_r)^2 \times (n_E \times n_z)$ to $2(N_r \times n_E \times n_z)$, where N_r represents the number of mock maps for each of the n_E energy bins and n_z redshift bins), so the speed is $N_r/2$ times faster than before. We show that this approach is correct in the limit of a large number of realizations, by following a theoretical derivation based on the Gaussian prediction for the APS covariance matrix. We have verified it numerically and the results shown here are also valid in a more general case when Gaussianity is not necessarily present. The derivation assumes the cross-correlation term is small when compared to the product of the autocorrelations for galaxies and γ-rays.

We start with the Gaussian prediction of the APS covariance matrix [217]:

$$\Gamma_{\ell\ell}^{C\gamma_i} \equiv \mathrm{cov}[C_\ell^{C\gamma_i}, C_\ell^{C\gamma_i}] = \frac{C_\ell^{CC} C_\ell^{\gamma_i\gamma_i} + (C_\ell^{C\gamma_i})^2}{(2\ell+1)\Delta\ell\, f_{\mathrm{sky}}} \delta^{\mathrm{D}}_{\ell\ell'}\,, \tag{B.1}$$

where $\Delta\ell$ is multipole interval size, f_{sky} is the fraction of sky surveyed. Here the measured quantity of the real sky map is represented by the $\hat{C}_\ell$ and C_ℓ is obtained from mock realization.

The following equation is for the case of real cluster catalogs and mock, from equation B.1 and considering that we construct the covariance by averaging over N_r realizations,

$$\Gamma_{\ell\ell'}^{\hat{C}\gamma_i} \equiv \mathrm{cov}[C_\ell^{\hat{C}\gamma_i}, C_{\ell'}^{\hat{C}\gamma_i}] \,\propto\, \hat{C}_\ell^{CC} \frac{1}{N_r} \sum_{n=1}^{N_r} C_\ell^{\gamma_i\gamma_i,n} + \frac{1}{N_r} \sum_{n=1}^{N_r} (C_\ell^{\hat{C}\gamma_i,n})^2, \tag{B.2}$$

and on the contrary,

$$\Gamma_{\ell\ell'}^{C\hat{\gamma}_i} \propto \hat{C}_\ell^{\gamma_i\gamma_i} \frac{1}{N_r} \sum_{n=1}^{N_r} C_\ell^{CC,n} + \frac{1}{N_r} \sum_{n=1}^{N_r} (C_\ell^{C\hat{\gamma}_i,n})^2, \tag{B.3}$$

is for the real γ-ray maps and catalogs mocks. When we only take the realization mocks into account, equation B.1 become

$$\Gamma_{\ell\ell'}^{C\gamma_i} \,\propto\, \left(\frac{1}{N_r} \sum_{n=1}^{N_r} C_\ell^{CC,n} \right) \left(\frac{1}{N_r} \sum_{n=1}^{N_r} C_\ell^{\gamma_i\gamma_i,n} \right) + \frac{1}{N_r^2} \sum_{n=1}^{N_r^2} (C_\ell^{C\gamma_i,n})^2\,. \tag{B.4}$$

Then the average of the expressions B.2 and B.3 is given by

$$\begin{aligned}(\Gamma^{C\gamma_i}_{\ell\ell'})_{\rm ave} &= \frac{1}{2}(\Gamma^{\hat{C}\gamma_i}_{\ell\ell'} + \Gamma^{C\hat{\gamma}_i}_{\ell\ell'}) \\ &\propto \hat{C}_\ell^{\gamma_i\gamma_i}\frac{1}{N_r}\sum_{n=1}^{N_r} C_\ell^{CC,n} + \hat{C}_\ell^{CC}\frac{1}{N_r}\sum_{n=1}^{N_r} C_\ell^{\gamma_i\gamma_i,n} + \frac{1}{N_r}\sum_{n=1}^{N_r}(C_\ell^{C\gamma_i,n})^2 \,. \qquad \text{(B.5)}\end{aligned}$$

The measured APS ($\hat{C}_\ell^{CC}$ and $\hat{C}_\ell^{\gamma\gamma}$) of real sky maps can be well reproduced by mocks

$$\begin{aligned}\hat{C}_\ell^{CC} &\simeq \frac{1}{N_r}\sum_{n=1}^{N_r} C_\ell^{CC,n}, \\ \hat{C}_\ell^{\gamma_i\gamma_i} &\simeq \frac{1}{N_r}\sum_{n=1}^{N_r} C_\ell^{\gamma_i\gamma_i,n}\,,\end{aligned} \qquad \text{(B.6)}$$

and we can get

$$(\Gamma^{C\gamma_i}_{\ell\ell'})_{\rm ave} \propto \left(\frac{1}{N_r}\sum_{n=1}^{N_r} C_\ell^{CC,n}\right)\left(\frac{1}{N_r}\sum_{n=1}^{N_r} C_\ell^{\gamma_i\gamma_i,n}\right) + \frac{1}{N_r^2}\sum_{n=1}^{N_r^2}(C_\ell^{C\gamma_i,n})^2 \,. \qquad \text{(B.7)}$$

Then, in the limit of large N_r it is

$$\frac{1}{N_r^2}\sum_{n=1}^{N_r^2}(C_\ell^{C\gamma_i,n})^2 \simeq \frac{1}{N_r}\sum_{n=1}^{N_r}(C_\ell^{C\gamma_i,n})^2 \,. \qquad \text{(B.8)}$$

In this situation, equation B.4 and B.7 have the same results. Therefore, we can obtain a reliable estimate of the covariance by simply averaging over the sum of the two "half" contributions

$$\Gamma^{C\gamma_i}_{\ell\ell'} = \frac{1}{2}(\Gamma^{\hat{C}\gamma_i}_{\ell\ell'} + \Gamma^{C\hat{\gamma}_i}_{\ell\ell'}) \,. \qquad \text{(B.9)}$$

Fig. B.1 shows the comparison between the covariance matrix generated from the above description and `Polspise`. We verify that the latter is not a minimum variance estimator. It can be seen that the covariance obtained by our realization mocks is very closed to the Gaussian estimate. On large scale region, the residuals from WHY18 and SDSSDR9 catalogs are around 10%, while MCXCsub and HIFLUGCS catalogs are always less than 10%. For small scales, the case of the SDSSDR9 catalog have differences while smaller than all the other cluster catalogs; all catalogs have very small residuals in the middle part.

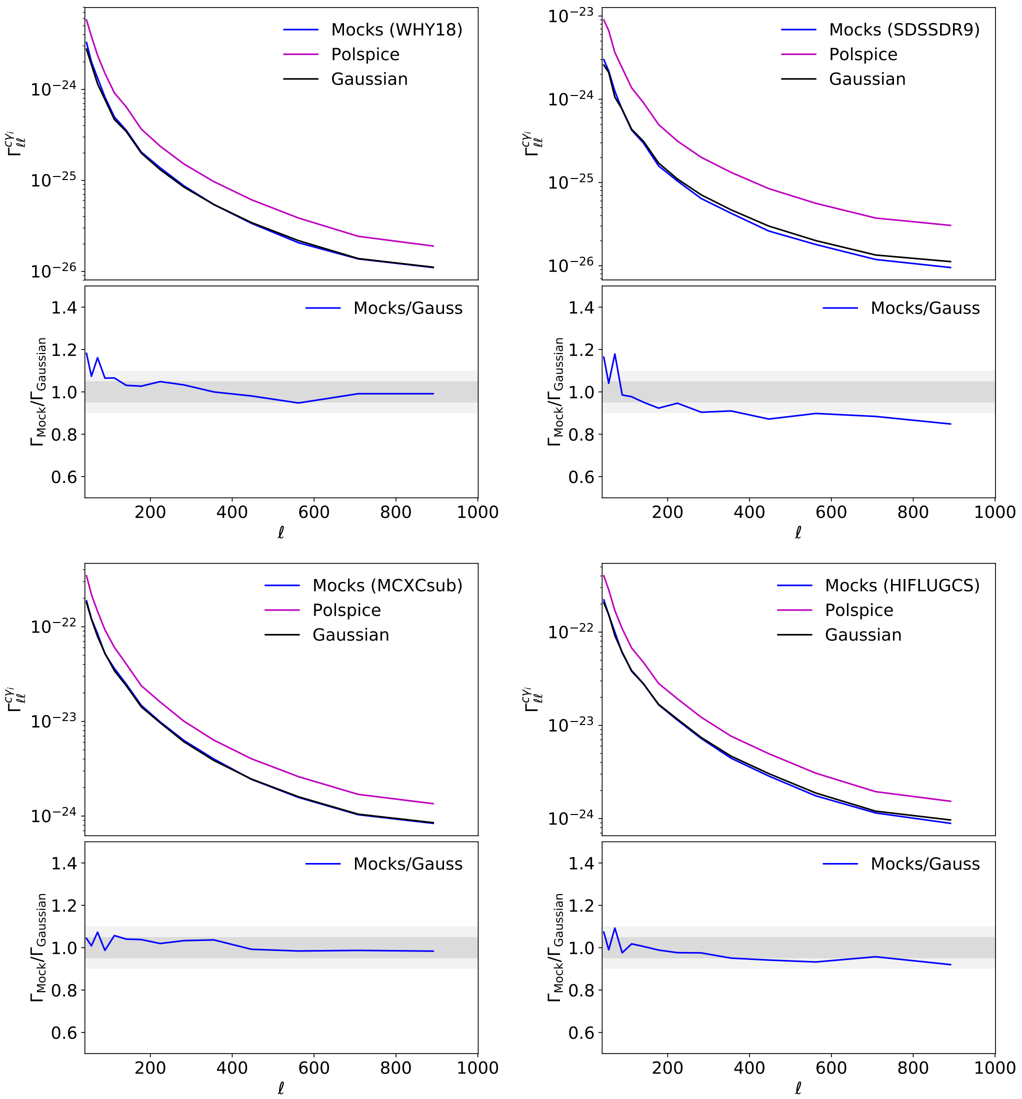

Figure B.1: The covariance of CAPS from mocks (blue), `PolSpice` (magenta) and Gaussian estimator (black), from the 3rd energy bins in Tab. 4.1. The upper panels are WYH18 and SDSSDR9 and bottom illustrates MCXCsub and HIGLUCS catalogs, respectively. The small panels are the ratio of mocks and Gaussian prediction, dark gray for 5% and light gray for 10%. The figure is taken from Ref. [175].

Appendix C

Fourier Transform of NFW Profile Square

Let us define some abbreviations for several special functions:

$$\begin{aligned}
\mathrm{Si}_1 &= \mathrm{Si}(k \cdot r_s); \\
\mathrm{Ci}_1 &= \mathrm{Ci}(k \cdot r_s); \\
\mathrm{Si}_2 &= \mathrm{Si}(k \cdot (r_s + r_{\mathrm{vir}})); \\
\mathrm{Ci}_2 &= \mathrm{Ci}(k \cdot (r_s + r_{\mathrm{vir}})); \\
\mathrm{Si}_3 &= \mathrm{Si}(k \cdot r_{\mathrm{vir}}); \\
\mathrm{Ci}_3 &= \mathrm{Ci}(k \cdot r_{\mathrm{vir}}),
\end{aligned} \tag{C.1}$$

where γ is Euler's constant, functions Ci and Si are taken from equation 2.47 and 2.46, respectively. Then the analytical solution for the Fourier transform of NFW profile square is given by

$$
\begin{aligned}
u^2(k|M) =&(r_s^2(-4kr_s^4 - 12kr_s^3 r_{\mathrm{vir}} - 12kr_s^2 r_{\mathrm{vir}}^2 - 4kr_s r_{vir}^3 + 4kr_s^4 \cos(kr_{\mathrm{vir}}) \\
&+ 7kr_s^3 r_{\mathrm{vir}} \cos(kr_{\mathrm{vir}}) + 3kr_s^2 r_{\mathrm{vir}}^2 \cos(kr_{\mathrm{vir}}) - (r_s + r_{\mathrm{vir}})^3 \\
&\mathrm{Ci}_1(kr_s(-6 + k^2 r_s^2) \cos(kr_s) - 3(-2 + k^2 r_s^2) \sin(kr_s)) + (r_s + r_{\mathrm{vir}})^3 \\
&\mathrm{Ci}_2(kr_s(-6 + k^2 r_s^2) \cos(kr_s) - 3(-2 + k^2 r_s^2) \sin(kr_s)) + 11.r_s^3 \sin(kr_{\mathrm{vir}}) \\
&- k^2 r_s^5 \sin(kr_{\mathrm{vir}}) + 15.r_s^2 r_{\mathrm{vir}} \sin(kr_{\mathrm{vir}}) - 2k^2 r_s^4 r_{\mathrm{vir}} \sin(kr_{\mathrm{vir}}) \\
&+ 6r_s r_{\mathrm{vir}}^2 \sin(kr_{\mathrm{vir}}) - k^2 r_s^3 r_{\mathrm{vir}}^2 \sin(kr_{\mathrm{vir}}) + 6r_s^3 \cos(kr_s)\mathrm{Si}_1 \\
&- 3k^2 r_s^5 \cos(kr_s)\mathrm{Si}_1 + 18r_s^2 r_{vir} \cos(kr_s)\mathrm{Si}_1 - 9k^2 r_s^4 r_{\mathrm{vir}} \cos(kr_s)\mathrm{Si}_1 \\
&+ 18r_s r_{\mathrm{vir}}^2 \cos(kr_s)\mathrm{Si}_1 - 9k^2 r_s^3 r_{\mathrm{vir}}^2 \cos(kr_s)\mathrm{Si}_1 + 6r_{\mathrm{vir}}^3 \cos(kr_s)\mathrm{Si}_1 \\
&- 3k^2 r_s^2 r_{\mathrm{vir}}^3 \cos(kr_s)\mathrm{Si}_1 + 6kr_s^4 \sin(kr_s)\mathrm{Si}_1 - k^3 r_s^6 \sin(kr_s)\mathrm{Si}_1 \\
&+ 18kr_s^3 r_{\mathrm{vir}} \sin(kr_s)\mathrm{Si}_1 - 3k^3 r_s^5 r_{\mathrm{vir}} \sin(kr_s)\mathrm{Si}_1 + 18kr_s^2 r_{\mathrm{vir}}^2 \sin(kr_s)\mathrm{Si}_1 \\
&- 3k^3 r_s^4 r_{\mathrm{vir}}^2 \sin(kr_s)\mathrm{Si}_1 + 6kr_s r_{\mathrm{vir}}^3 \sin(kr_s)\mathrm{Si}_1 - k^3 r_s^3 r_{\mathrm{vir}}^3 \sin(kr_s)\mathrm{Si}_1 \\
&+ 6r_s^3\mathrm{Si}_3 + 18r_s^2 r_{\mathrm{vir}}\mathrm{Si}_3 + 18r_s r_{\mathrm{vir}}^2\mathrm{Si}_3 + 6r_{\mathrm{vir}}^3\mathrm{Si}_3 - 6r_s^3 \cos(kr_s)\mathrm{Si}_2 \\
&+ 3k^2 r_s^5 \cos(kr_s)\mathrm{Si}_2 - 18r_s^2 r_{\mathrm{vir}} \cos(kr_s)\mathrm{Si}_2 + 9k^2 r_s^4 r_{\mathrm{vir}} \cos(kr_s)\mathrm{Si}_2 \\
&- 18r_s r_{\mathrm{vir}}^2 \cos(kr_s)\mathrm{Si}_2 + 9k^2 r_s^3 r_{\mathrm{vir}}^2 \cos(kr_s)\mathrm{Si}_2 - 6r_{\mathrm{vir}}^3 \cos(kr_s)\mathrm{Si}_2 \\
&+ 3k^2 r_s^2 r_{\mathrm{vir}}^3 \cos(kr_s)\mathrm{Si}_2 - 6kr_s^4 \sin(kr_s)\mathrm{Si}_2 + k^3 r_s^6 \sin(kr_s)\mathrm{Si}_2 \\
&- 18kr_s^3 r_{\mathrm{vir}} \sin(kr_s)\mathrm{Si}_2 + 3k^3 r_s^5 r_{\mathrm{vir}} \sin(kr_s)\mathrm{Si}_2 - 18kr_s^2 r_{\mathrm{vir}}^2 \sin(kr_s)\mathrm{Si}_2 \\
&+ 3k^3 r_s^4 r_{\mathrm{vir}}^2 \sin(kr_s)\mathrm{Si}_2 - 6kr_s r_{\mathrm{vir}}^3 \sin(kr_s)\mathrm{Si}_2 \\
&+ k^3 r_s^3 r_{\mathrm{vir}}^3 \sin(kr_s)\mathrm{Si}_2))/(6k(r_s + r_{\mathrm{vir}})^3) \\
&(M^2/(4/3\pi r_s^3)/(\log(1 + c) - c/(1 + c))^2).
\end{aligned}
\tag{C.2}
$$

---

where c is the same as in equation 2.42.

Bibliography

[1] A. Einstein, "Die feldgleichungen der gravitation", Sitzungsberichte der Königlich Preußischen Akademie der Wissenschaften (Berlin, 844–847 (1915).

[2] `https://www.cfa.harvard.edu/~dfabricant/huchra/zcat/`.

[3] S. Dodelson, *Modern Cosmology* (Academic Press, Amsterdam, 2003).

[4] E. Hubble, "A Relation between Distance and Radial Velocity among Extra-Galactic Nebulae", Proceedings of the National Academy of Science **15**, 168–173 (1929).

[5] A. A. Penzias and R. W. Wilson, "A Measurement of Excess Antenna Temperature at 4080 Mc/s.", The Astrophysical Journal **142**, 419–421 (1965).

[6] T. P. Walker, G. Steigman, D. N. Schramm, K. A. Olive, and H.-S. Kang, "Primordial nucleosynthesis redux", Astrophys. J. **376**, 51–69 (1991).

[7] M. S. Smith, L. H. Kawano, and R. A. Malaney, "Experimental, computational, and observational analysis of primordial nucleosynthesis", Astrophys. J. Suppl. **85**, 219–247 (1993).

[8] G. Steigman, D. N. Schramm, and J. E. Gunn, "Cosmological limits to the number of massive leptons", Physics Letters B **66**, 202–204 (1977).

[9] I. Bars, J. Terning, and F. Nekoogar, *Extra dimensions in space and time* (Springer, 2010).

[10] `https://www.sdss.org/science/orangepie/`.

[11] E. P. Hubble, "Extragalactic nebulae.", Astrophys.J. **64**, 321–369 (1926).

[12] E. Hubble, "The Distribution of Extra-Galactic Nebulae", Astrophys.J. **79**, 8 (1934).

[13] M. J. GELLER and J. P. HUCHRA, "Mapping the universe", Science **246**, 897–903 (1989).

[14] D. G. York et al., "The Sloan Digital Sky Survey: Technical Summary", Astron. J. **120**, 1579–1587 (2000).

[15] N. Aghanim et al., "Planck 2018 results. VI. Cosmological parameters", arXiv e-prints (2018).

[16] A. Friedman, "Über die krümmung des raumes", Zeitschrift für Physik **10**, 377–386 (1922).

[17] A. H. Guth and S.-Y. Pi, "Fluctuations in the new inflationary universe", Phys. Rev. Lett. **49**, 1110–1113 (1982).

[18] R. H. Brandenberger, “Quantum field theory methods and inflationary universe models”, Rev. Mod. Phys. **57**, 1–60 (1985).

[19] A. H. Guth, “Inflationary universe: a possible solution to the horizon and flatness problems”, Phys. Rev. D **23**, 347–356 (1981).

[20] A. Linde, “A new inflationary universe scenario: a possible solution of the horizon, flatness, homogeneity, isotropy and primordial monopole problems”, Physics Letters B **108**, 389–393 (1982).

[21] A. Starobinsky, “Dynamics of phase transition in the new inflationary universe scenario and generation of perturbations”, Physics Letters B **117**, 175–178 (1982).

[22] S. Hawking, “The development of irregularities in a single bubble inflationary universe”, Physics Letters B **115**, 295–297 (1982).

[23] A. Albrecht and P. J. Steinhardt, “Cosmology for grand unified theories with radiatively induced symmetry breaking”, Phys. Rev. Lett. **48**, 1220–1223 (1982).

[24] F. Lucchin and S. Matarrese, “Power-law inflation”, Phys. Rev. D **32**, 1316–1322 (1985).

[25] V. Mukhanov, H. Feldman, and R. Brandenberger, “Theory of cosmological perturbations”, Physics Reports **215**, 203–333 (1992).

[26] D. J. Fixsen, “The Temperature of the Cosmic Microwave Background”, Astrophys. J. **707**, 916–920 (2009).

[27] S. Weinberg et al., *Cosmology* (Oxford university press, 2008).

[28] J. Peacock, “Models for large scale structure”, (1998).

[29] E. R. Harrison, “Fluctuations at the threshold of classical cosmology”, Phys. Rev. D **1**, 2726–2730 (1970).

[30] Y. B. Zeldovich, “A hypothesis, unifying the structure and the entropy of the Universe”, Mon. Not. Roy. Astron. Soc. **160**, 1P (1972).

[31] R. K. Sheth and T. Giuseppe, “An excursion set model of hierarchical clustering: ellipsoidal collapse and the moving barrier”, Mon.Not.Roy.Astron.Soc. **329**, 61–75 (2002).

[32] J. Comparat, “Stellar population properties for 2 million galaxies from SDSS DR14 and DEEP2 DR4 from full spectral fitting”, PoS **FRAPWS2018**, 036 (2019).

[33] J. F. Navarro, C. S. Frenk, and S. D. M. White, “The Structure of Cold Dark Matter Halos”, Astrophys.J. **462**, 563 (1996).

[34] J. Einasto, “On the Construction of a Composite Model for the Galaxy and on the Determination of the System of Galactic Parameters”, Trudy Astrofizicheskogo Instituta Alma-Ata **5**, 87–100 (1965).

[35] B. Diemer and A. V. Kravtsov, “Dependence of the outer density profiles of halos on their mass accretion rate”, Astrophys. J. **789**, 1 (2014).

[36] A. Cooray and R. K. Sheth, “Halo Models of Large Scale Structure”, Phys. Rept. **372**, 1–129 (2002).

[37] H. J. Mo, Y. P. Jing, and S. D. M. White, “High-order correlations of peaks and haloes: a step towards understanding galaxy biasing”, Monthly Notices of the Royal Astronomical Society **284**, 189–201 (1997).

[38] R. K. Sheth, H. J. Mo, and G. Tormen, “Ellipsoidal collapse and an improved model for the number and spatial distribution of dark matter haloes”, Mon.Not.Roy.Astron.Soc. **323**, 1–12 (2001).

[39] J. L. Tinker, B. E. Robertson, A. V. Kravtsov, A. Klypin, M. S. Warren, G. Yepes, and S. Gottlöber, “The Large-scale Bias of Dark Matter Halos: Numerical Calibration and Model Tests”, Astrophys.J. **724**, 878–886 (2010).

[40] J. A. Peacock and R. E. Smith, “Halo occupation numbers and galaxy bias”, Mon.Not.Roy.Astron.Soc. **318**, 1144–1156 (2000).

[41] I. Zehavi et al., “On departures from a power law in the galaxy correlation function”, Astrophys. J. **608**, 16–24 (2004).

[42] R. E. Smith, J. A. Peacock, A. Jenkins, S. D. M. White, C. S. Frenk, F. R. Pearce, P. A. Thomas, G. Efstathiou, and H. M. P. Couchman, “Stable clustering, the halo model and non-linear cosmological power spectra”, Monthly Notices of the Royal Astronomical Society **341**, 1311–1332 (2003).

[43] F. Zwicky, “Die Rotverschiebung von extragalaktischen Nebeln”, Helvetica Physica Acta **6**, 110–127 (1933).

[44] V. C. Rubin and J. Ford W. Kent, “Rotation of the Andromeda Nebula from a Spectroscopic Survey of Emission Regions”, Astrophys.J. **159**, 379 (1970).

[45] T. S. van Albada, J. N. Bahcall, K. Begeman, and R. Sancisi, “Distribution of dark matter in the spiral galaxy NGC 3198.”, Astrophys.J. **295**, 305–313 (1985).

[46] B. Famaey and S. McGaugh, “Modified Newtonian Dynamics (MOND): Observational Phenomenology and Relativistic Extensions”, Living Rev. Rel. **15**, 10 (2012).

[47] `https://hubblesite.org/contents/news-releases/2007/news-2007-17.html`.

[48] M. J. Jee, “Tracing the Peculiar Dark Matter Structure in the Galaxy Cluster Cl 0024+17 with Intracluster Stars and Gas”, Astrophys.J. **717**, 420–434 (2010).

[49] D. Clowe, M. Bradač, A. H. Gonzalez, M. Markevitch, S. W. Randall, C. Jones, and D. Zaritsky, “A direct empirical proof of the existence of dark matter”, The Astrophysical Journal **648**, L109–L113 (2006).

[50] M. Davis, G. Efstathiou, C. S. Frenk, and S. D. M. White, “The evolution of large-scale structure in a universe dominated by cold dark matter”, Astrophys.J. **292**, 371–394 (1985).

[51] G. Bertone, D. Hooper, and J. Silk, “Particle dark matter: Evidence, candidates and constraints”, Phys. Rept. **405**, 279–390 (2005).

[52] J. L. Feng, “Dark Matter Candidates from Particle Physics and Methods of Detection”, Ann. Rev. Astron. Astrophys. **48**, 495–545 (2010).

[53] S. Dodelson and L. M. Widrow, “Sterile neutrinos as dark matter”, Phys. Rev. Lett. **72**, 17–20 (1994).

[54] P. B. Pal and L. Wolfenstein, “Radiative decays of massive neutrinos”, Phys. Rev. D **25**, 766–773 (1982).

[55] M. Drewes et al., “A White Paper on keV Sterile Neutrino Dark Matter”, JCAP **01**, 025 (2017).

[56] K. N. Abazajian, “Sterile neutrinos in cosmology”, Phys. Rept. **711-712**, 1–28 (2017).

[57] A. Boyarsky, M. Drewes, T. Lasserre, S. Mertens, and O. Ruchayskiy, “Sterile neutrino Dark Matter”, Prog. Part. Nucl. Phys. **104**, 1–45 (2019).

[58] G. G. Raffelt, “Astrophysical axion bounds”, Lect. Notes Phys. **741**, edited by M. Kuster, G. Raffelt, and B. Beltran, 51–71 (2008).

[59] H. Primakoff, “Photo-production of neutral mesons in nuclear electric fields and the mean life of the neutral meson”, Phys. Rev. **81**, 899–899 (1951).

[60] K. Zioutas et al., “First results from the CERN Axion Solar Telescope (CAST)”, Phys. Rev. Lett. **94**, 121301 (2005).

[61] M. Tada, Y. Kishimoto, K. Kominato, M. Shibata, H. Funahashi, K. Yamamoto, A. Masaike, and S. Matsuki, “Carrack ii — a new large-scale experiment to search for axions with rydberg-atom cavity detector”, Nuclear Physics B - Proceedings Supplements **72**, Proceedings of the 5th IFT Workshop on Axions, 164–168 (1999).

[62] N. Du, N. Force, R. Khatiwada, E. Lentz, R. Ottens, L. J. Rosenberg, G. Rybka, G. Carosi, N. Woollett, D. Bowring, et al., “Search for invisible axion dark matter with the axion dark matter experiment”, Phys. Rev. Lett. **120**, 151301 (2018).

[63] F. Della Valle, A. Ejlli, U. Gastaldi, G. Messineo, E. Milotti, R. Pengo, G. Ruoso, and G. Zavattini, “The PVLAS experiment: measuring vacuum magnetic bire-

fringence and dichroism with a birefringent Fabry–Perot cavity", Eur. Phys. J. C **76**, 24 (2016).

[64] K. Griest, "Galactic Microlensing as a Method of Detecting Massive Compact Halo Objects", Astrophys. J. **366**, 412 (1991).

[65] B. Carr, F. Kuhnel, and M. Sandstad, "Primordial Black Holes as Dark Matter", Phys. Rev. D **94**, 083504 (2016).

[66] R. Laha, "Primordial Black Holes as a Dark Matter Candidate Are Severely Constrained by the Galactic Center 511 keV γ -Ray Line", Phys. Rev. Lett. **123**, 251101 (2019).

[67] L. Roszkowski, E. M. Sessolo, and S. Trojanowski, "WIMP dark matter candidates and searches—current status and future prospects", Rept. Prog. Phys. **81**, 066201 (2018).

[68] T. Han, ed., *Proceedings of Theoretical Advanced Study Institute in Elementary Particle Physics on The dawn of the LHC era (TASI 2008): Boulder, USA, June 2-27, 2008* (World Scientific, Hackensack, USA, Nov. 2010).

[69] C. Muñoz, "Models of supersymmetry for dark matter", EPJ Web Conf. **136**, 01002 (2017).

[70] G. Jungman, M. Kamionkowski, and K. Griest, "Supersymmetric dark matter", Phys. Rept. **267**, 195–373 (1996).

[71] E. W. Kolb and M. S. Turner, *The Early Universe*, Vol. 69 (1990).

[72] M. Drees and F. Hajkarim, “Neutralino Dark Matter in Scenarios with Early Matter Domination”, JHEP **12**, 042 (2018).

[73] T. Flacke, D. W. Kang, K. Kong, G. Mohlabeng, and S. C. Park, “Electroweak Kaluza-Klein Dark Matter”, JHEP **04**, 041 (2017).

[74] P. Nath et al., “The Hunt for New Physics at the Large Hadron Collider”, Nucl. Phys. B Proc. Suppl. **200-202**, edited by G. Alverson, P. Nath, and B. D. Nelson, 185–417 (2010).

[75] M. W. Goodman and E. Witten, “Detectability of certain dark-matter candidates”, Phys. Rev. D **31**, 3059–3063 (1985).

[76] R. J. Gaitskell, “Direct detection of dark matter”, Annual Review of Nuclear and Particle Science **54**, 315–359 (2004).

[77] R. Bernabei et al., “Dark matter particles in the Galactic halo: Results and implications from DAMA/NaI”, Int. J. Mod. Phys. D **13**, 2127–2160 (2004).

[78] R. Bernabei et al., “First results from DAMA/LIBRA and the combined results with DAMA/NaI”, Eur. Phys. J. C **56**, 333–355 (2008).

[79] C. Savage, G. Gelmini, P. Gondolo, and K. Freese, “Compatibility of DAMA/LIBRA dark matter detection with other searches”, JCAP **04**, 010 (2009).

[80] Z. Ahmed et al., “Dark Matter Search Results from the CDMS II Experiment”, Science **327**, 1619–1621 (2010).

[81] C. Aalseth et al., “Results from a Search for Light-Mass Dark Matter with a P-type Point Contact Germanium Detector”, Phys. Rev. Lett. **106**, 131301 (2011).

[82] E. Aprile, K. Arisaka, F. Arneodo, A. Askin, L. Baudis, A. Behrens, K. Bokeloh, E. Brown, J. M. R. Cardoso, B. Choi, et al., "First dark matter results from the xenon100 experiment", Phys. Rev. Lett. **105**, 131302 (2010).

[83] G. Angloher, M. Bauer, I. Bavykina, A. Bento, C. Bucci, C. Ciemniak, G. Deuter, F. von Feilitzsch, D. Hauff, P. Huff, et al., "Results from 730 kg days of the CRESST-II Dark Matter search", European Physical Journal C **72**, 1971, 1971 (2012).

[84] R. Agnese et al., "Silicon Detector Dark Matter Results from the Final Exposure of CDMS II", Phys. Rev. Lett. **111**, 251301 (2013).

[85] D. Akerib et al., "First results from the LUX dark matter experiment at the Sanford Underground Research Facility", Phys. Rev. Lett. **112**, 091303 (2014).

[86] L. Bergstrom, "Dark Matter Evidence, Particle Physics Candidates and Detection Methods", Annalen Phys. **524**, 479–496 (2012).

[87] H. Abdalla et al., "H.E.S.S. first public test data release", (2018) `10.5281/zenodo.1421098`.

[88] F. Krennrich, I. Bond, P. Boyle, S. Bradbury, J. Buckley, D. Carter-Lewis, O. Celik, W. Cui, M. Daniel, M. D'Vali, et al., "Veritas: the very energetic radiation imaging telescope array system", New Astronomy Reviews **48**, 2nd VERITAS Symposium on the Astrophysics of Extragalactic Sources, 345–349 (2004).

[89] V. Acciari et al., "A search for dark matter in Triangulum II with the MAGIC telescopes", Phys. Dark Univ. **28**, 100529 (2020).

[90] B. Bartoli, P. Bernardini, X. J. Bi, C. Bleve, I. Bolognino, P. Branchini, A. Budano, A. K. Calabrese Melcarne, P. Camarri, Z. Cao, et al., “Observation of the cosmic ray moon shadowing effect with the argo-ybj experiment”, Phys. Rev. D **84**, 022003 (2011).

[91] G. Di Sciascio, “Latest results from the ARGO-YBJ experiment”, J. Phys. Conf. Ser. **632**, 012089 (2015).

[92] X. Bai et al., “The Large High Altitude Air Shower Observatory (LHAASO) Science White Paper”, (2019).

[93] M. Cirelli, “Indirect Searches for Dark Matter: a status review”, Pramana **79**, edited by R. Godbole and N. K. Mondal, 1021–1043 (2012).

[94] L. Zhao and J. Liu, “Experimental search for dark matter in China”, Front. Phys. (Beijing) **15**, 44301 (2020).

[95] W. B. Atwood, A. A. Abdo, M. Ackermann, W. Althouse, B. Anderson, M. Axelsson, L. Baldini, J. Ballet, D. L. Band, G. Barbiellini, et al., “THE LARGE AREA TELESCOPE ON THEFERMI GAMMA-RAY SPACE TELESCOPEMISSION”, The Astrophysical Journal **697**, 1071–1102 (2009).

[96] L. Baldini, “The large area telescope in the context of the extended fermi mission”, Nuclear Physics B - Proceedings Supplements **243-244**, Proceedings of the IV International Conference on Particle and Fundamental Physics in Space, 125–130 (2013).

[97] C. Meegan, G. Lichti, P. N. Bhat, E. Bissaldi, M. S. Briggs, V. Connaughton, R. Diehl, G. Fishman, J. Greiner, A. S. Hoover, et al., “The fermi gamma-ray burst monitor”, The Astrophysical Journal **702**, 791–804 (2009).

[98] W. Atwood, A. A. Abdo, M. Ackermann, W. Althouse, B. Anderson, M. Axelsson, L. Baldini, J. Ballet, D. Band, G. Barbiellini, et al., “The large area telescope on the fermi gamma-ray space telescope mission”, The Astrophysical Journal **697**, 1071 (2009).

[99] A. Abdo, M. Ackermann, M. Ajello, J. Ampe, B. Anderson, W. Atwood, M. Axelsson, R. Bagagli, L. Baldini, J. Ballet, et al., “The on-orbit calibration of the fermi large area telescope”, Astroparticle Physics **32**, 193–219 (2009).

[100] `https://www.slac.stanford.edu/exp/glast/groups/canda/lat_Performance.html`.

[101] S. Abdollahi, F. Acero, M. Ackermann, M. Ajello, W. B. Atwood, M. Axelsson, L. Baldini, J. Ballet, G. Barbiellini, D. Bastieri, et al., “Fermi Large Area Telescope Fourth Source Catalog”, Astrophys. J. Suppl. **247**, 33, 33 (2020).

[102] M. Ackermann, M. Ajello, A. Albert, A. Allafort, W. B. Atwood, M. Axelsson, L. Baldini, J. Ballet, G. Barbiellini, D. Bastieri, et al., “THE FERMI LARGE AREA TELESCOPE ON ORBIT: EVENT CLASSIFICATION, INSTRUMENT RESPONSE FUNCTIONS, AND CALIBRATION”, The Astrophysical Journal Supplement Series **203**, 4 (2012).

[103] M. Ajello, R. Angioni, M. Axelsson, J. Ballet, G. Barbiellini, D. Bastieri, J. Becerra Gonzalez, R. Bellazzini, E. Bissaldi, E. D. Bloom, et al., “The Fourth Catalog of

Active Galactic Nuclei Detected by the Fermi Large Area Telescope", Astrophys.J. **892**, 105, 105 (2020).

[104] M. Ajello, W. B. Atwood, L. Baldini, J. Ballet, G. Barbiellini, D. Bastieri, R. Bellazzini, E. Bissaldi, R. D. Blandford, E. D. Bloom, et al., "3FHL: The Third Catalog of Hard Fermi-LAT Sources", Astrophys. J. Suppl. **232**, 18, 18 (2017).

[105] S. Ammazzalorso, N. Fornengo, S. Horiuchi, and M. Regis, "Characterizing the local gamma-ray Universe via angular cross-correlations", Phys. Rev. **D98**, 103007 (2018).

[106] Y. Akrami et al., "Planck 2018 results. IV. Diffuse component separation", arXiv e-prints (2018).

[107] E. L. Wright, P. R. M. Eisenhardt, A. K. Mainzer, M. E. Ressler, R. M. Cutri, T. Jarrett, J. D. Kirkpatrick, D. Padgett, R. S. McMillan, M. Skrutskie, et al., "The Wide-field Infrared Survey Explorer (WISE): Mission Description and Initial On-orbit Performance", Astron.J. **140**, 1868–1881 (2010).

[108] N. Hambly, M. Irwin, and H. MacGillivray, "The SuperCOSMOS Sky Survey — II. Image detection, parametrization, classification and photometry", Monthly Notices of the Royal Astronomical Society **326**, 1295–1314 (2001).

[109] Z. L. Wen, H. J. J. L., and F. Yang, "A catalogue of clusters of galaxies identified from all sky surveys of 2mass, wise, and supercosmos", Mon.Not.Roy.Astron.Soc. **475**, 343–352 (2018).

[110] J. Kepner, X. Fan, N. Bahcall, J. Gunn, R. Lupton, and G. Xu, "An Automated Cluster Finder: The Adaptive Matched Filter", Astrophys.J. **517**, 78–91 (1999).

[111] E. Branchini, S. Camera, A. Cuoco, N. Fornengo, M. Regis, M. Viel, and J.-Q. Xia, "Cross-correlating the gamma-ray sky with catalogs of galaxy clusters", The Astrophysical Journal Supplement Series **228**, 8 (2017).

[112] R. Piffaretti, M. Arnaud, G. W. Pratt, E. Pointecouteau, and J. .-.-B. Melin, "The MCXC: a meta-catalogue of x-ray detected clusters of galaxies", Astronomy and Astrophysics **534**, A109, A109 (2011).

[113] W. Voges, B. Aschenbach, T. Boller, H. Bräuninger, U. Briel, W. Burkert, K. Dennerl, J. Englhauser, R. Gruber, F. Haberl, et al., "The ROSAT all-sky survey bright source catalogue", Astronomy and Astrophysics **349**, 389–405 (1999).

[114] I. Reiss and U. Keshet, "Detection of virial shocks in stacked Fermi-LAT galaxy clusters", JCAP **10**, 010, 010 (2018).

[115] T. H. Reiprich and H. Böhringer, "The Mass Function of an X-Ray Flux-limited Sample of Galaxy Clusters", Astrophys.J. **567**, 716–740 (2002).

[116] W. Hu and A. V. Kravtsov, "Sample Variance Considerations for Cluster Surveys", Astrophys.J. **584**, 702–715 (2003).

[117] D. Alonso, A. I. Salvador, F. J. Sánchez, M. Bilicki, J. García-Bellido, and E. Sánchez, "Homogeneity and isotropy in the Two Micron All Sky Survey Photometric Redshift catalogue", Mon.Not.Roy.Astron.Soc. **449**, 670–684 (2015).

[118] G. Schellenberger and T. H. Reiprich, “HICOSMO - cosmology with a complete sample of galaxy clusters - I. Data analysis, sample selection and luminosity-mass scaling relation”, Mon.Not.Roy.Astron.Soc. **469**, 3738–3761 (2017).

[119] F. J. Samaniego, *A comparison of the bayesian and frequentist approaches to estimation* (Springer Science & Business Media, 2010).

[120] W. K. Hastings, “Monte Carlo sampling methods using Markov chains and their applications”, Biometrika **57**, 97–109 (1970).

[121] A. Lewis, “Efficient sampling of fast and slow cosmological parameters”, Phys. Rev. D **87**, 103529 (2013).

[122] J. Akeret, S. Seehars, A. Amara, A. Refregier, and A. Csillaghy, “CosmoHammer: Cosmological parameter estimation with the MCMC Hammer”, arXiv e-prints, arXiv:1212.1721, arXiv:1212.1721 (2012).

[123] D. Foreman-Mackey, D. W. Hogg, D. Lang, and J. Goodman, “emcee: The MCMC Hammer”, The Astronomical Society of the Pacific **125**, 306 (2013).

[124] M. Kilbinger, D. Wraith, C. P. Robert, K. Benabed, O. Cappé, J.-F. Cardoso, G. Fort, S. Prunet, and F. R. Bouchet, “Bayesian model comparison in cosmology with Population Monte Carlo”, Monthly Notices of the Royal Astronomical Society **405**, 2381–2390 (2010).

[125] J. Salvatier, T. Wiecki, and C. Fonnesbeck, “Probabilistic Programming in Python using PyMC”, arXiv e-prints, arXiv:1507.08050, arXiv:1507.08050 (2015).

[126] T. Brinckmann and J. Lesgourgues, “MontePython 3: boosted MCMC sampler and other features”, Phys. Dark Univ. **24**, 100260 (2019).

[127] J. Zuntz, M. Paterno, E. Jennings, D. Rudd, A. Manzotti, S. Dodelson, S. Bridle, S. Sehrish, and J. Kowalkowski, “CosmoSIS: modular cosmological parameter estimation”, Astron. Comput. **12**, 45–59 (2015).

[128] T. H. and K. T., “The Correlation Function for the Distribution of Galaxies”, Publications of the Astronomical Society of Japan **21**, 221 (1969).

[129] P. P. J. P. J. E., *The large-scale structure of the universe* (1980).

[130] D. N. Limber, “The Analysis of Counts of the Extragalactic Nebulae in Terms of a Fluctuating Density Field.”, Astrophys.J. **117**, 134 (1953).

[131] J.-Q. Xia, A. Cuoco, E. Branchini, M. Fornasa, and M. Viel, “A cross-correlation study of the Fermi-LAT gamma-ray diffuse extragalactic signal”, Monthly Notices of the Royal Astronomical Society **416**, 2247–2264 (2011).

[132] M. Regis, J.-Q. Xia, A. Cuoco, E. Branchini, N. Fornengo, and M. Viel, “Particle dark matter searches outside the Local Group”, Phys. Rev. Lett. **114**, 241301 (2015).

[133] A. Cuoco, J.-Q. Xia, M. Regis, E. Branchini, N. Fornengo, and M. Viel, “Dark Matter Searches in the Gamma-ray Extragalactic Background via Cross-correlations With Galaxy Catalogs”, Astrophys. J. Suppl. **221**, 29 (2015).

[134] J.-Q. Xia, A. Cuoco, E. Branchini, and M. Viel, “Tomography of the fermi-lat gamma-ray diffuse extragalactic signal via cross-correlations with galaxy catalogs”, The Astrophysical Journal Supplement Series **217**, 15 (2015).

[135] M. Shirasaki, S. Horiuchi, and N. Yoshida, “Cross-Correlation of the Extragalactic Gamma-ray Background with Luminous Red Galaxies”, Phys. Rev. D **92**, 123540 (2015).

[136] A. Cuoco, M. Bilicki, J.-Q. Xia, and E. Branchini, “Tomographic imaging of the Fermi-LAT gamma-ray sky through cross-correlations: A wider and deeper look”, Astrophys. J. Suppl. **232**, 10 (2017).

[137] Y. Zhao, X.-J. Bi, P.-F. Yin, and X. Zhang, “Constraint on the velocity dependent dark matter annihilation cross section from gamma-ray and kinematic observations of ultrafaint dwarf galaxies”, Phys. Rev. D **97**, 063013 (2018).

[138] S. Li, Y.-F. Liang, Z.-Q. Xia, L. Zu, K.-K. Duan, Z.-Q. Shen, L. Feng, Q. Yuan, and Y.-Z. Fan, “Study of the boxlike dark matter signals from dwarf spheroidal galaxies with fermi-lat data”, Phys. Rev. D **97**, 083007 (2018).

[139] S. Ando, A. Geringer-Sameth, N. Hiroshima, S. Hoof, R. Trotta, and M. G. Walker, “Structure Formation Models Weaken Limits on WIMP Dark Matter from Dwarf Spheroidal Galaxies”, (2020).

[140] D. Hashimoto, A. J. Nishizawa, M. Shirasaki, O. Macias, S. Horiuchi, H. Tashiro, and M. Oguri, “Measurement of redshift dependent cross correlation of HSC clusters and Fermi γ rays”, (2018) `10.1093/mnras/stz321`.

[141] N. Fornengo, L. Perotto, M. Regis, and S. Camera, "Evidence of Cross-correlation between the CMB Lensing and the Γ-ray sky", Astrophys. J. Lett. **802**, L1 (2015).

[142] C. Feng, A. Cooray, and B. Keating, "Planck Lensing and Cosmic Infrared Background Cross-Correlation with Fermi-LAT: Tracing Dark Matter Signals in the Gamma-Ray Background", Astrophys. J. **836**, 127 (2017).

[143] S. Camera, M. Fornasa, N. Fornengo, and M. Regis, "A Novel Approach in the Weakly Interacting Massive Particle Quest: Cross-correlation of Gamma-Ray Anisotropies and Cosmic Shear", Astrophys. J. Lett. **771**, L5 (2013).

[144] S. Camera, M. Fornasa, N. Fornengo, and M. Regis, "Tomographic-spectral approach for dark matter detection in the cross-correlation between cosmic shear and diffuse γ-ray emission", JCAP **6**, 029, 029 (2015).

[145] M. Shirasaki, S. Horiuchi, and N. Yoshida, "Cross-Correlation of Cosmic Shear and Extragalactic Gamma-ray Background: Constraints on the Dark Matter Annihilation Cross-Section", Phys. Rev. D **90**, 063502 (2014).

[146] T. Tröster et al., "Cross-correlation of weak lensing and gamma rays: implications for the nature of dark matter", Mon. Not. Roy. Astron. Soc. **467**, 2706–2722 (2017).

[147] M. Shirasaki, O. Macias, S. Horiuchi, S. Shirai, and N. Yoshida, "Cosmological constraints on dark matter annihilation and decay: Cross-correlation analysis of the extragalactic γ-ray background and cosmic shear", Phys. Rev. D **94**, 063522 (2016).

[148] M. Shirasaki, O. Macias, S. Horiuchi, N. Yoshida, C.-H. Lee, and A. J. Nishizawa, "Correlation of extragalactic γ rays with cosmic matter density distributions from weak gravitational lensing", Phys. Rev. D **97**, 123015 (2018).

[149] S. Ammazzalorso et al., "Detection of Cross-Correlation between Gravitational Lensing and γ Rays", Phys. Rev. Lett. **124**, 101102 (2020).

[150] Y. Inoue and T. Totani, "The Blazar Sequence and the Cosmic Gamma-Ray Background Radiation in the Fermi Era", Astrophys. J. **702**, [Erratum: Astrophys. J.728,73(2011)], 523–536 (2009).

[151] A. Abdo, M. Ackermann, M. Ajello, E. Antolini, L. Baldini, J. Ballet, G. Barbiellini, D. Bastieri, B. Baughman, K. Bechtol, et al., "The fermi-lat high-latitude survey: source count distributions and the origin of the extragalactic diffuse background", The Astrophysical Journal **720**, 435 (2010).

[152] M. Ackermann, M. Ajello, A. Allafort, L. Baldini, et al., "GeV Observations of Star-forming Galaxies with *Fermi* LAT", Astrophys.J. **755**, 164 (2012).

[153] M. Di Mauro, F. Calore, F. Donato, M. Ajello, and L. Latronico, "Diffuse γ-ray emission from misaligned active galactic nuclei", Astrophys.J. **780**, 161 (2014).

[154] M. Cirelli, G. Corcella, A. Hektor, G. Hutsi, M. Kadastik, P. Panci, M. Raidal, F. Sala, and A. Strumia, "PPPC 4 DM ID: A Poor Particle Physicist Cookbook for Dark Matter Indirect Detection", JCAP **1103**, [Erratum: JCAP1210,E01(2012)], 051 (2011).

[155] R. C. Gilmore, R. S. Somerville, J. R. Primack, and A. Dominguez, "Semi-analytic modelling of the extragalactic background light and consequences for extragalactic gamma-ray spectra", Monthly Notices of the Royal Astronomical Society **422**, 3189–3207 (2012).

[156] M. Fornasa et al., "Angular power spectrum of the diffuse gamma-ray emission as measured by the Fermi Large Area Telescope and constraints on its dark matter interpretation", Phys. Rev. **D94**, 123005 (2016).

[157] Á. Moliné, J. A. Schewtschenko, S. Palomares-Ruiz, C. Bœhm, and C. M. Baugh, "Isotropic extragalactic flux from dark matter annihilations: lessons from interacting dark matter scenarios", JCAP **1608**, 069 (2016).

[158] N. Hiroshima, S. Ando, and T. Ishiyama, "Modeling evolution of dark matter substructure and annihilation boost", Phys. Rev. **D97**, 123002 (2018).

[159] L. Gao, C. Frenk, A. Jenkins, V. Springel, and S. White, "Where will supersymmetric dark matter first be seen?", Mon.Not.Roy.Astron.Soc. **419**, 1721 (2012).

[160] M. Ajello et al., "The Cosmic Evolution of Fermi BL Lacertae Objects", Astrophys. J. **780**, 73 (2014).

[161] M. Ajello, M. S. Shaw, R. W. Romani, C. D. Dermer, L. Costamante, O. G. King, W. Max-Moerbeck, A. Readhead, A. Reimer, J. L. Richards, et al., "The luminosity function of fermi-detected flat-spectrum radio quasars", The Astrophysical Journal **751**, 108 (2012).

[162] S. Bonoli, F. Marulli, V. Springel, S. D. White, E. Branchini, and L. Moscardini, “Modeling the cosmological co-evolution of supermassive black holes and galaxies: II. The clustering of quasars and their dark environment”, Mon. Not. Roy. Astron. Soc. **396**, 423 (2009).

[163] C. Gruppioni et al., “The Herschel PEP/HerMES Luminosity Function. I: Probing the Evolution of PACS selected Galaxies to z 4”, Mon. Not. Roy. Astron. Soc. **432**, 23 (2013).

[164] C. J. Willott, S. Rawlings, K. M. Blundell, M. Lacy, and S. A. Eales, “The radio luminosity function from the low-frequency 3CRR, 6CE and 7CRS complete samples”, Monthly Notices of the Royal Astronomical Society **322**, 536–552 (2001).

[165] I. Zehavi et al., “The Luminosity and color dependence of the galaxy correlation function”, Astrophys. J. **630**, 1–27 (2005).

[166] B. A. Reid, H.-J. Seo, A. Leauthaud, J. L. Tinker, and M. White, “A 2.5 per cent measurement of the growth rate from small-scale redshift space clustering of sdss-iii cmass galaxies”, Monthly Notices of the Royal Astronomical Society **444**, 476–502 (2014).

[167] S. Ho, A. Cuesta, H.-J. Seo, R. de Putter, A. J. Ross, M. White, N. Padmanabhan, S. Saito, D. J. Schlegel, E. Schlafly, et al., “Clustering of Sloan Digital Sky Survey III Photometric Luminous Galaxies: The Measurement, Systematics, and Cosmological Implications”, Astrophys. J. **761**, 14, 14 (2012).

[168] M. White, M. Blanton, A. Bolton, D. Schlegel, J. Tinker, A. Berlind, L. da Costa, E. Kazin, Y. Lin, M. Maia, et al., “The Clustering of Massive Galaxies at z 0.5 from the First Semester of BOSS Data”, Astrophys. J. **728**, 126, 126 (2011).

[169] A. J. Ross, S. Ho, A. J. Cuesta, R. Tojeiro, W. J. Percival, D. Wake, K. L. Masters, R. C. Nichol, A. D. Myers, F. de Simoni, et al., “Ameliorating systematic uncertainties in the angular clustering of galaxies: a study using the SDSS-III”, Monthly Notices of the Royal Astronomical Society **417**, 1350–1373 (2011).

[170] V. Allevato, A. Finoguenov, and N. Cappelluti, “Clustering of gamma ray selected 2lacfermiblazars”, The Astrophysical Journal **797**, 96 (2014).

[171] M. Ackermann, M. Ajello, A. Albert, W. B. Atwood, L. Baldini, J. Ballet, G. Barbiellini, D. Bastieri, K. Bechtol, R. Bellazzini, et al., “The Spectrum of Isotropic Diffuse Gamma-Ray Emission between 100 MeV and 820 GeV”, Astrophys.J. **799**, 86, 86 (2015).

[172] F. Zandanel and S. Ando, “Constraints on diffuse gamma-ray emission from structure formation processes in the Coma cluster”, Mon.Not.Roy.Astron.Soc. **440**, 663–671 (2014).

[173] M. R. Becker et al., “Cosmic shear measurements with Dark Energy Survey Science Verification data”, Phys. Rev. **D94**, 022002 (2016).

[174] H. Akaike, “A new look at the statistical model identification”, in *Selected papers of hirotugu akaike* (Springer, 1974), pp. 215–222.

[175] M. Colavincenzo, X. Tan, S. Ammazzalorso, S. Camera, M. Regis, J.-Q. Xia, and N. Fornengo, “Searching for gamma-ray emission from galaxy clusters at low redshift”, Mon. Not. Roy. Astron. Soc. **491**, 3225–3244 (2020).

[176] The Fermi-LAT collaboration, “The Fourth Catalog of Active Galactic Nuclei Detected by the Fermi Large Area Telescope”, arXiv e-prints, arXiv:1905.10771, arXiv:1905.10771 (2019).

[177] M. Ackermann et al., “Unresolved Gamma-Ray Sky through its Angular Power Spectrum”, Phys. Rev. Lett. **121**, 241101 (2018).

[178] X. Tan, M. Colavincenzo, and S. Ammazzalorso, “Bounds on WIMP dark matter from galaxy clusters at low redshift”, Mon. Not. Roy. Astron. Soc. **495**, 114–122 (2020).

[179] M. Ackermann et al., “Searching for Dark Matter Annihilation from Milky Way Dwarf Spheroidal Galaxies with Six Years of Fermi Large Area Telescope Data”, Phys. Rev. Lett. **115**, 231301 (2015).

[180] A. Albert et al., “Searching for Dark Matter Annihilation in Recently Discovered Milky Way Satellites with Fermi-LAT”, Astrophys. J. **834**, 110 (2017).

[181] A. G. Riess, L.-G. Strolger, J. Tonry, S. Casertano, H. C. Ferguson, B. Mobasher, P. Challis, A. V. Filippenko, S. Jha, W. Li, et al., “Type Ia Supernova Discoveries at z > 1 from the Hubble Space Telescope: Evidence for Past Deceleration and Constraints on Dark Energy Evolution”, Astrophys.J. **607**, 665–687 (2004).

[182] M. Kowalski et al., “Improved Cosmological Constraints from New, Old and Combined Supernova Datasets”, Astrophys. J. **686**, 749–778 (2008).

[183] M. Hicken, W. M. Wood-Vasey, S. Blondin, P. Challis, S. Jha, P. L. Kelly, A. Rest, and R. P. Kirshner, “Improved Dark Energy Constraints from ~100 New CfA Supernova Type Ia Light Curves”, Astrophys. J. **700**, 1097–1140 (2009).

[184] D. J. Eisenstein et al., “Detection of the Baryon Acoustic Peak in the Large-Scale Correlation Function of SDSS Luminous Red Galaxies”, Astrophys. J. **633**, 560–574 (2005).

[185] W. J. Percival, B. A. Reid, D. J. Eisenstein, N. A. Bahcall, T. Budavari, J. A. Frieman, M. Fukugita, J. E. Gunn, Ž. Ivezić, G. R. Knapp, et al., “Baryon acoustic oscillations in the Sloan Digital Sky Survey Data Release 7 galaxy sample”, Monthly Notices of the Royal Astronomical Society **401**, 2148–2168 (2010).

[186] T. Schrabback, J. Hartlap, B. Joachimi, M. Kilbinger, P. Simon, K. Benabed, M. Bradač, T. Eifler, T. Erben, C. D. Fassnacht, et al., “Evidence of the accelerated expansion of the Universe from weak lensing tomography with COSMOS”, Astronomy and Astrophysics **516**, A63, A63 (2010).

[187] D. J. Bacon, A. R. Refregier, and R. S. Ellis, “Detection of weak gravitational lensing by large-scale structure”, Monthly Notices of the Royal Astronomical Society **318**, 625–640 (2000).

[188] M. Birkinshaw, “The sunyaev–zel’dovich effect”, Physics Reports **310**, 97–195 (1999).

[189] R. G. Crittenden and N. Turok, "Looking for Lambda with the Rees-Sciama effect", Phys. Rev. Lett. **76**, 575 (1996).

[190] S. P. Boughn, R. G. Crittenden, and N. G. Turok, "Correlations between the cosmic X-ray and microwave backgrounds: Constraints on a cosmological constant", New Astron. **3**, 275–291 (1998).

[191] M. R. Nolta et al., "First year Wilkinson Microwave Anisotropy Probe (WMAP) observations: Dark energy induced correlation with radio sources", Astrophys. J. **608**, 10–15 (2004).

[192] N. Afshordi, Y.-S. Loh, and M. A. Strauss, "Cross - correlation of the Cosmic Microwave Background with the 2MASS galaxy survey: Signatures of dark energy, hot gas, and point sources", Phys. Rev. **D69**, 083524 (2004).

[193] C. L. Francis and J. A. Peacock, "An estimate of the local ISW signal, and its impact on CMB anomalies", Mon. Not. Roy. Astron. Soc. **406**, 14 (2010).

[194] F. .-.-X. Dupe, A. Rassat, J. .-.-L. Starck, and M. J. Fadili, "Measuring the Integrated Sachs-Wolfe Effect", Astron. Astrophys. **534**, A51 (2011).

[195] R. Scranton et al., "Physical evidence for dark energy", (2003).

[196] P. Fosalba, E. Gaztanaga, and F. Castander, "Detection of the ISW and SZ effects from the CMB-galaxy correlation", Astrophys. J. **597**, L89–92 (2003).

[197] B. R. Granett, M. C. Neyrinck, and I. Szapudi, "An Imprint of Super-Structures on the Microwave Background due to the Integrated Sachs-Wolfe Effect", Astrophys. J. **683**, L99–L102 (2008).

[198] S. Chen and D. J. Schwarz, “Angular two-point correlation of NVSS galaxies revisited”, Astron. Astrophys. **591**, A135 (2016).

[199] T. Goto, I. Szapudi, and B. R. Granett, “Cross-correlation of WISE Galaxies with the Cosmic Microwave Background”, Mon. Not. Roy. Astron. Soc. **422**, L77–L81 (2012).

[200] S. Ferraro, B. D. Sherwin, and D. N. Spergel, “WISE measurement of the integrated Sachs-Wolfe effect”, Phys. Rev. **D91**, 083533 (2015).

[201] S. P. Boughn, R. G. Crittenden, and G. P. Koehrsen, “The Large scale structure of the x-ray background and its cosmological implications”, Astrophys. J. **580**, 672–684 (2002).

[202] T. Giannantonio, R. Scranton, R. G. Crittenden, R. C. Nichol, S. P. Boughn, A. D. Myers, and G. T. Richards, “Combined analysis of the integrated Sachs-Wolfe effect and cosmological implications”, Phys. Rev. **D77**, 123520 (2008).

[203] J.-Q. Xia, A. Cuoco, E. Branchini, M. Fornasa, and M. Viel, “A cross-correlation study of the Fermi-LAT γ-ray diffuse extragalactic signal”, Mon. Not. Roy. Astron. Soc. **416**, 2247–2264 (2011).

[204] S. Khosravi, A. Mollazadeh, and S. Baghram, “ISW-galaxy cross correlation: a probe of dark energy clustering and distribution of dark matter tracers”, JCAP **1609**, 003 (2016).

[205] P. A. R. Ade et al., “Planck 2013 results. XIX. The integrated Sachs-Wolfe effect”, Astron. Astrophys. **571**, A19 (2014).

[206] P. A. R. Ade et al., “Planck 2015 results. XXI. The integrated Sachs-Wolfe effect”, Astron. Astrophys. **594**, A21 (2016).

[207] B. Stölzner, A. Cuoco, J. Lesgourgues, and M. Bilicki, “Updated tomographic analysis of the integrated Sachs-Wolfe effect and implications for dark energy”, Phys. Rev. **D97**, 063506 (2018).

[208] R. S. Somerville, K. Lee, H. C. Ferguson, J. P. Gardner, L. A. Moustakas, and M. Giavalisco, “Cosmic variance in the great observatories origins deep survey”, Astrophys. J. Lett. **600**, L171 (2004).

[209] R. G. Crittenden and N. Turok, “Looking for a cosmological constant with the rees-sciama effect”, Phys. Rev. Lett. **76**, 575–578 (1996).

[210] M. Kamionkowski, “Matter microwave correlations in an open universe”, Phys. Rev. D **54**, 4169–4170 (1996).

[211] Y.-S. Song, W. Hu, and I. Sawicki, “Large scale structure of f(R) gravity”, physical review d **75**, 044004, 044004 (2007).

[212] X.-H. Tan, J.-P. Dai, and J.-Q. Xia, “Searching for Integrated Sachs–Wolfe Effect from $Fermi$-LAT diffuse γ-ray map”, Phys. Dark Univ. **29**, 100585 (2020).

[213] I. Reiss and U. Keshet, “Detection of virial shocks in stacked Fermi-LAT galaxy clusters”, JCAP **2018**, 010, 010 (2018).

[214] P. Norberg, C. M. Baugh, E. Gaztañaga, and D. J. Croton, “Statistical analysis of galaxy surveys - I. Robust error estimation for two-point clustering statistics”, Mon. Not. Roy. Astron. Soc. **396**, 19–38 (2009).

[215] M. De Domenico and H. Lyberis, “Fast generation of mock maps from realistic catalogs of astrophysical objects”, ArXiv e-prints (2012).

[216] H. S. Xavier, F. B. Abdalla, and B. Joachimi, “Improving lognormal models for cosmological fields”, Mon. Not. Roy. Astron. Soc. **459**, 3693–3710 (2016).

[217] W. Hu and B. Jain, “Joint galaxy-lensing observables and the dark energy”, Phys. Rev. D **70**, 043009 (2004).